QED EFFECTS IN LASER-PLASMA INTERACTIONS

THOMAS G. BLACKBURN

A thesis submitted for the degree of *Doctor of Philosophy*

St. John's College

University of Oxford

Hilary 2015

ABSTRACT

It is possible to reach the radiation-reaction–dominated regime in today's high-intensity laser facilities, using the collision of a wakefield-accelerated GeV electron beam with a 30 fs laser pulse of intensity 10^{22} Wcm^{-2}. This would demonstrate that the yield of high energy gamma rays is increased by the stochastic nature of photon emission: a beam of 10^9 electrons will emit 6300 photons with energy > 700 MeV, $60\times$ the number predicted classically. Detecting those photons, or a prominent low energy peak in the electron beam's post-collision energy spectrum, will provide strong evidence of quantum radiation reaction; we place constraints on the accuracy of timing necessary to achieve this.

This experiment would provide benchmarking for the simulations that will be used to study the plasmas produced in the next generation of laser facilities. With focused intensities $> 10^{23}$ Wcm^{-2}, these will be powerful enough to generate high fluxes of gamma rays and electron-positron pairs from laser–laser and laser–solid interactions. It will become possible to test the physics of exotic astrophysical phenomena, such as pair cascades in pulsar magnetospheres, and explore fundamental aspects of quantum electrodynamics (QED). To that end we will discuss: classical theories of radiation reaction; QED processes in intense fields; and a Monte Carlo algorithm by which the latter may be included in particle-in-cell codes. The feedback between QED processes and classical plasma dynamics characterises a new regime we call QED-plasma physics.

ACKNOWLEDGMENTS

This work would not have been possible without the continuing advice, support and hospitality of Chris Ridgers, John Kirk and my supervisor Tony Bell. They have my sincere admiration and gratitude, both scientifically and personally. I am indebted to the residents of 316.3 past and present – Brian Reville, Klara Schure, Gwenael Giacinti and Anabella Araudo – and to Chris Murphy for many stimulating discussions over these past four years. Finally, to my friends at Trinity and St. John's, and especially my parents, my deepest thanks.

PUBLICATIONS

Ideas and figures from this thesis have appeared in the following publications:

- T. G. Blackburn, C. P. Ridgers, J. G. Kirk, and A. R. Bell. Quantum radiation reaction in laser–electron-beam collisions. *Phys. Rev. Lett.*, 112:015001, Jan 2014. doi: 10.1103/PhysRevLett.112.015001. URL http://link.aps.org/doi/10.1103/PhysRevLett.112.015001.

- C. P. Ridgers, J. G. Kirk, R. Duclous, T. G. Blackburn, C. S. Brady, K. Bennett, T. D. Arber, and A. R. Bell. Modelling gamma-ray photon emission and pair production in high-intensity laser-matter interactions. *J. Comp. Phys.*, 260:273–285, Mar 2014. doi: 10.1016/j.jcp.2013.12.007. URL http://www.sciencedirect.com/science/article/pii/S0021999113008061.

- T. G. Blackburn. Measuring quantum radiation reaction in laser–electron-beam collisions. *Plasma Phys. Control. Fusion*, 57(7): 075012, Jun 2015. doi: 10.1088/0741-3335/57/7/075012. URL http://iopscience.iop.org/0741-3335/57/7/075012.

CONTENTS

1

INTRODUCTION

1.1 MOTIVATION

The development of multi-PW laser systems, and the prospect of focusing laser pulses to intensities greater than 10^{22} Wcm^{-2} [1, 2, 3], has led to substantial interest in how radiation reaction and strong-field quantum electrodynamics (QED) processes will alter the plasma physics studied in high-power laser facilities over the next decade.

Radiation reaction, the energy-momentum loss of a particle radiating electromagnetic waves in classical electrodynamics, has been studied theoretically for a century [4, 5, 6] and strong-field QED [7, 8, 9] for at least half that time. Experimental study of these two with lasers is interesting of itself, addressing as it would fundamental questions about the transition from classical to quantum electrodynamics [10].

However, we are poised on the edge of a new regime of plasma physics where the feedback between classical plasma dynamics and these new effects becomes significant [11]. That boundary can be quantified in terms of the laser strength parameter a_0, the work done on an electron over a laser wavelength λ in units of the electron rest energy mc^2:

$$a_0 = \frac{eE}{mc\omega} = 0.60 \left(\frac{I}{10^{18}\ \text{Wcm}^{-2}}\right)^{1/2} \left(\frac{\lambda}{\mu\text{m}}\right) \tag{1.1.1}$$

where e is the electron charge, E the laser root-mean-square (r. m. s.) electric field, ω its angular frequency and I its average intensity. When $a_0 \geqslant 1$, for example, the electron gains mc^2 over a distance λ; at relativistic velocity, the magnitude of the magnetic component of the

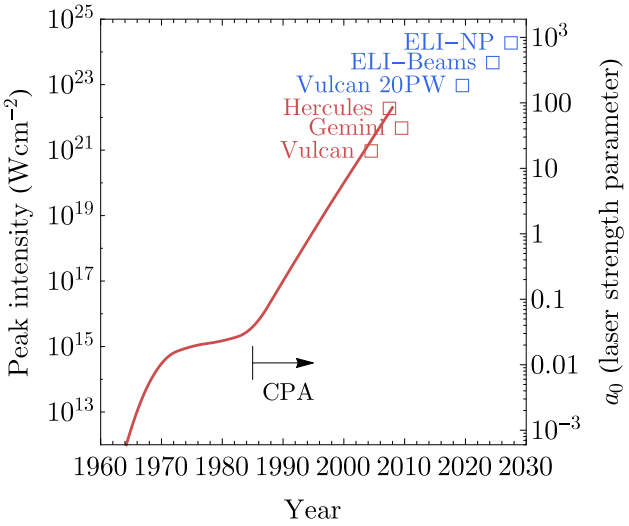

Figure 1: The increase in peak laser intensity with time, with examples of existing facilities in red and planned facilities in blue. Since the invention of chirped pulse amplification (CPA) in 1985 [12], that increase has been nearly exponential. a_0, the laser strength parameter, has been calculated for a wavelength of 1 μm.

Lorentz force becomes comparable to that of the electric component and electron motion becomes highly non-linear. This is the regime of *relativistic plasma physics*.

It is likely that the next generation of high-power laser facilities will reach peak intensities in excess of 10^{23} Wcm^{-2} (see fig. 1). When $a_0 >$ 100, electrons will be accelerated so strongly that their loss of energy to radiation must be taken into account in the equations of motion [13, 14, 15]. Furthermore, single photons of that radiation will be sufficiently energetic that they can produce electron-positron pairs by colliding with photons of the laser pulse [16, 17, 18]. Even if pair production is not dynamically significant, it is necessary to include quantum corrections to the radiation damping as classical electromagnetism predicts the emission of photons with energy greater than that of the electron and so overestimates the emissivity [19, 20].

The inclusion of these effects naturally alters plasma physics, as the electron motion is strongly damped by radiation and pair production introduces new sources of current to the plasma. However, the rates of

radiation emission and pair creation are determined by the large-scale electromagnetic fields, which are set by collective plasma dynamics. We term such plasmas *QED-plasmas* to emphasise the importance of this coupling [11, 21, 22].

The purpose of this thesis is threefold: to justify the necessity of including radiation reaction and QED when considering laser-plasmas with $a_0 > 100$; to explain how such plasmas may be modelled; and to show that it is possible to probe the QED-plasma regime in an experiment that could be accomplished in today's high-intensity laser facilities.

Let us begin by showing in section 1.2 that an electron in an intense electromagnetic wave is strongly accelerated and that the back-reaction of its radiation losses will be non-negligible for laser intensities $> 10^{21}$ Wcm^{-2}.

1.1.1 *Notation and units*

SI units are used throughout, except in chapter 2 where natural units ($\hbar = c = \epsilon_0 = 1$) are used instead. Per-particle energies will be expressed in MeV and intensities in Wcm^{-2}. The values of the physical constants used are given in SI and natural units in table 1.

Contravariant components of a four-vector are denoted with superscripted Greek indices

$$a^\mu \equiv \left(a^0, a^1, a^2, a^3\right) \tag{1.1.2}$$

and covariant components by subscripted Greek indices

$$a_\mu \equiv \eta_{\mu\nu} a^\nu. \tag{1.1.3}$$

Constant	Value in: SI units	natural units
α, fine-structure constant	7.30×10^{-3}	same
c, speed of light in vacuum	3.00×10^{8} ms^{-1}	1
e, electron charge	1.60×10^{-19} C	0.303
ϵ_0, vacuum permittivity	8.85×10^{-12} Fm^{-1}	1
E_{Sch}, Schwinger field	1.33×10^{18} Vm^{-1}	0.862 MeV^2
$\hbar$, reduced Planck constant	1.06×10^{-34} Js^{-1}	1
$\lambda\!\!\!^{-}_{\text{c}}$, Compton length ($\hbar/mc$)	3.86×10^{-12} m	1.96 MeV^{-1}
m, electron mass	9.11×10^{-31} kg	0.511 MeV
μ_0, vacuum permeability	$4\pi \times 10^{-7}$ Hm^{-1}	1
τ_{c}, Compton time ($\lambda\!\!\!^{-}_{\text{c}}/c$)	1.29×10^{-21} s	1.96 MeV^{-1}

Table 1: Physical constants, in SI and natural units.

Roman indices refer only to the spatial components $1, 2, 3$. Indices are repeated on the same side of an equation are implicitly summed over. The metric is given by

$$\eta^{\mu\nu} = \eta_{\mu\nu} = \text{diag}\,(1, -1, -1, -1) \tag{1.1.4}$$

and the scalar product of two four-vectors by

$$a \cdot b \equiv \eta_{\mu\nu} a^\mu b^\nu. \tag{1.1.5}$$

The four-gradient

$$\partial_\mu \equiv \frac{\partial}{\partial x^\mu} = \left(\frac{1}{c}\frac{\partial}{\partial t}, \frac{\partial}{\partial x}, \frac{\partial}{\partial y}, \frac{\partial}{\partial z}\right). \tag{1.1.6}$$

1.1.2 *Role of the author*

Chapter 1, the majority of chapter 2 and chapter 3 review the existing literature about radiation reaction, strong-field QED, and their incorporation in laser-plasma physics. My original work is found section 2.6.2 and chapter 4.

For the former, I developed a Monte-Carlo code to simulate gamma ray production from energetic electrons in laser pulses with $a_0 \leqslant 2$, implementing the non-linear Compton scattering rate described in section 2.4. Experimental data used as input were kindly provided by C. D. Murphy [23]; I performed the simulations and analysis given in section 2.6.2.

I also developed a Monte-Carlo code to simulate gamma ray and pair production in laser–electron-beam collisions for $a_0 > 20$, using the algorithm that is outlined in section 3.7.1.2 (from Duclous et al. [17]) to implement the strong-field QED processes described in chapter 3. This code is also capable of simulating electrons subject to the modified classical radiation reaction term given in section 3.3.3. I performed the simulations and analysis given in section 4.2 and section 4.3; a condensed version of the former has been published as Blackburn et al. [20].

1.2 RADIATION LOSSES OF AN ACCELERATING CHARGE

1.2.1 *The Larmor power*

The power radiated by an accelerating charge is given by the Larmor formula [24]. That can be derived by considering the electric and magnetic fields of a charge moving with arbitrary velocity and acceleration using the Liénard-Wiechert potentials [25]. However, we will reproduce a physically intuitive derivation from Longair [26] that is attributed to Thomson [27].

Let us consider a charge q, initially stationary at the origin of a particular inertial reference frame, that accelerates to a velocity $\Delta v \ll c$ over a short interval Δt. After a time t, information about that acceleration has only propagated outward to a radial distance of $r = ct$.

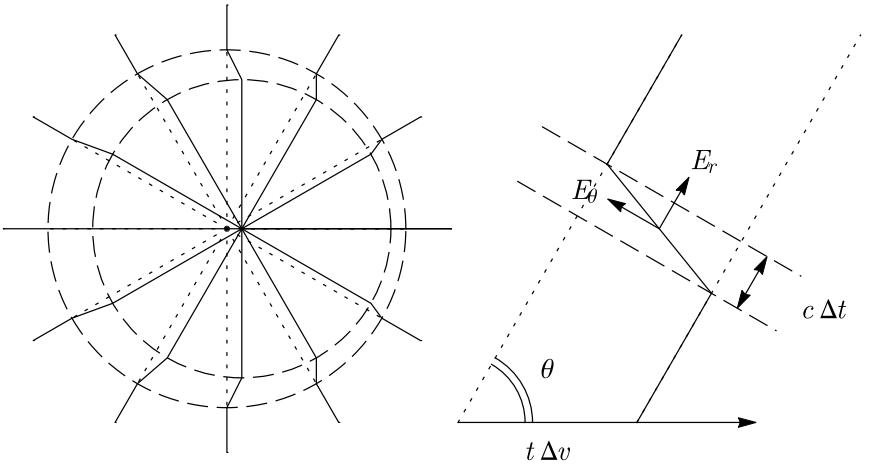

Figure 2: (left) The electric field lines of a charge that accelerates to velocity Δv in a time Δt. (right) The tangential and radial electric fields E_θ and E_r at a distance ct from the charge form a pulse of EM radiation of duration Δt. (Adapted from Longair [26].)

Outside that sphere the electric field must be unchanged, i.e. it still points radially outward from the origin. Within the sphere the field lines are directed radially outward from the origin of a reference frame that is moving with the charge at a speed Δv. That means within a spherical shell of thickness $c\Delta t$ there is a time-varying tangential component of electric field, or a pulse of electromagnetic radiation. This is shown in the left of fig. 2.

Away from the charge the electric field must be divergence-free, by Gauss's law. Therefore the electric field lines must be continuous across this spherical shell, as shown in the right of fig. 2. The ratio of the tangential and radial electric fields is given by

$$\frac{E_\theta}{E_r} = \frac{t\Delta v \sin\theta}{c\Delta t}. \tag{1.2.1}$$

By identifying $t = r/c$, $E_r = q/(4\pi\epsilon_0 r^2)$ and $\Delta v/\Delta t$ with the acceleration $|\mathbf{a}|$, we find that

$$E_\theta = \frac{q\,|\mathbf{a}|\sin\theta}{4\pi\epsilon_0 c^2 r}. \tag{1.2.2}$$

As E_θ changes from 0 to the above value and back to 0 over the course of the pulse time Δt, there must also be an azimuthal magnetic field $B_\phi = E_r/c$ by Ampere's law. The Poynting flux $S = E_\theta B_\phi/\mu_0$ is directed radially outwards with magnitude

$$S = \frac{q^2 |\mathbf{a}|^2 \sin^2\theta}{16\pi^2\epsilon_0 c^3 r^2}. \tag{1.2.3}$$

Integrating this over the surface of the spherical shell, we find the radiated power is given by

$$\mathcal{P} = \frac{q^2 |\mathbf{a}|^2}{6\pi\epsilon_0 c^3} \tag{1.2.4}$$

which was first obtained for non-relativistic charges by Larmor [28].

The total radiated power is a Lorentz invariant [25] (the radiation carries no net momentum in the charge's instantaneous rest frame), so (1.2.4) can be written in the manifestly covariant form

$$\mathcal{P} = -\frac{q^2}{6\pi\epsilon_0 m^2 c^3}\left(\frac{\mathrm{d}p}{\mathrm{d}\tau}\cdot\frac{\mathrm{d}p}{\mathrm{d}\tau}\right). \tag{1.2.5}$$

Expanding the scalar product, the radiated power in a reference frame where the charge moves with velocity $\mathbf{v}$ and acceleration $\mathbf{a}$ is [24]

$$\mathcal{P} = \frac{q^2\gamma^4}{6\pi\epsilon_0 c^3}\left[|\mathbf{a}|^2 + \left(\frac{\gamma\mathbf{a}\cdot\mathbf{v}}{c}\right)^2\right]. \tag{1.2.6}$$

The γ^4 factor means that radiative losses are negligible for non-relativistic particles but large for accelerating charges with $|\mathbf{v}| \to c$. Although in the particle's instantaneous rest frame the radiation is dipolar and so carries no net momentum, this is not true in a general reference frame due to relativistic beaming. The radiation will be concentrated into a cone of opening angle $\sim 1/\gamma$ around the charge's velocity vector; as that radiation carries momentum, there must be a back-reaction on the particle. This is called *radiation reaction* and will be the subject of section 1.3.

First let us consider when radiative energy losses become significant in laser-plasma interactions, using the simple analytical model of a charge in a plane electromagnetic wave.

1.2.2 *In a plane electromagnetic wave*

The dynamics of a point particle with charge q, mass m and four-momentum $p^\mu = \gamma m(c, \mathbf{v})$, where $\gamma = (1 - |\mathbf{v}|^2/c^2)^{-1/2}$ is the Lorentz factor and $\mathbf{v}$ the three-velocity, in an electromagnetic field $F^{\mu\nu}$ are determined by the Lorentz force

$$\frac{\mathrm{d}p^\mu}{\mathrm{d}\tau} = \mathcal{F}^\mu_{\mathrm{L}} \equiv \frac{q}{mc} F^{\mu\nu} p_\nu. \tag{1.2.7}$$

The motion is parametrised by the proper time τ. In three-components, identifying $\frac{\mathrm{d}}{\mathrm{d}\tau} = \gamma \frac{\mathrm{d}}{\mathrm{d}t}$, (1.2.7) takes the form

$$\frac{\mathrm{d}\mathcal{E}}{\mathrm{d}t} = q\mathbf{E} \cdot \mathbf{v} \tag{1.2.8}$$

$$\frac{\mathrm{d}\mathbf{p}}{\mathrm{d}t} = q\left(\mathbf{E} + \mathbf{v} \times \mathbf{B}\right). \tag{1.2.9}$$

The electromagnetic field $F^{\mu\nu}$ is defined as the antisymmetrised derivative of the four-potential

$$A^\mu = (\Phi, c\mathbf{A}), \tag{1.2.10}$$

$$F_{\mu\nu} = \partial_\mu A_\nu - \partial_\nu A_\mu \tag{1.2.11}$$

where $\partial_\mu \equiv \frac{\partial}{\partial x^\mu}$. In Cartesian coordinates, its components are

$$\begin{aligned} F_{0i} = -F_{i0} &= E_i \\ F_{ij} &= -c\varepsilon_{ijk} B_k \end{aligned} \tag{1.2.12}$$

where E_i, B_i are components of the electric and magnetic fields respectively and ε_{ijk} the antisymmetric Levi-Civita symbol. The dual tensor is given by

$$F^*_{\mu\nu} = \frac{1}{2}\varepsilon_{\mu\nu\alpha\beta}F^{\alpha\beta}. \tag{1.2.13}$$

1.2.2.1 *Equations of motion*

The field arising from a plane, transverse electromagnetic wave is characterised by a four-potential

$$A^\mu = A^\mu_1 \cos\phi + A^\mu_2 \sin\phi \tag{1.2.14}$$

that is a function of a single Lorentz-invariant parameter $\phi = k \cdot x$. Here k is the wave's (null) four-frequency $k^\mu = (\omega/c)(1, \hat{\mathbf{k}})$, ω its angular frequency and $\hat{\mathbf{k}}$ is directed along its axis of propagation. $A^\mu_{1,2}$ are constant four-vectors that satisfy $A_1 \cdot A_2 = 0$; in the *Lorenz gauge* the four-potential must be divergence-free, i.e. $\partial \cdot A = 0$, so

$$k \cdot A_1 = k \cdot A_2 = 0. \tag{1.2.15}$$

(1.2.15) and the lightlike nature of k mean that electromagnetic field arising from the potential (1.2.14)

$$F^{\mu\nu} = (k^\mu A^\nu_2 - k^\nu A^\mu_2)\cos\phi - (k^\mu A^\nu_1 - k^\nu A^\mu_1)\sin\phi \tag{1.2.16}$$

is perpendicular to k. Dotting (1.2.7) with k, we can show that $k \cdot p$ is a constant of motion:

$$\frac{\mathrm{d}}{\mathrm{d}\tau} k \cdot p = 0. \tag{1.2.17}$$

As the electromagnetic field is a function only of ϕ, it would make sense to parametrise the electron motion by ϕ as well, instead of the proper time τ.

$$\frac{\mathrm{d}\phi}{\mathrm{d}\tau} = \frac{k \cdot p}{m} = \text{constant} \neq 0 \tag{1.2.18}$$

allows us to rewrite (1.2.7) as

$$\frac{\mathrm{d}p^\mu}{\mathrm{d}\phi} = \frac{q}{c}\frac{F^{\mu\nu}p_\nu}{k\cdot p}. \tag{1.2.19}$$

Substituting (1.2.16), the equations of motion become

$$\frac{\mathrm{d}p^\mu}{\mathrm{d}\phi} = \frac{q}{c}\left[\left(A_1^\mu - \frac{A_1\cdot p}{k\cdot p}k^\mu\right)\sin\phi - \left(A_2^\mu - \frac{A_2\cdot p}{k\cdot p}k^\mu\right)\cos\phi\right] \tag{1.2.20}$$

and

$$\frac{\mathrm{d}x^\mu}{\mathrm{d}\phi} = \frac{p^\mu}{k\cdot p}. \tag{1.2.21}$$

Taking only the components of (1.2.20) perpendicular to k, we have that

$$p_\perp^\mu = p_{0\perp}^\mu - \frac{q}{c}A^\mu \tag{1.2.22}$$

where p_0 is the electron four-momentum in the absence of the wave; although the wave defined by eqs. (1.2.14) and (1.2.16) is perfectly monochromatic and so must be of infinite extent, this is acceptable if the wave switches-on sufficiently slowly that the amplitude can be taken as constant. (1.2.20) can then be integrated by recognising that $A_{1,2}\cdot p = A_{1,2}\cdot p_\perp$ as A is always transverse. The result is

$$p^\mu = p_0^\mu - \frac{q}{c}A^\mu + \frac{q}{c}\frac{A\cdot p_0}{k\cdot p_0}k^\mu - \frac{q^2}{2c^2}\frac{A^2}{k\cdot p_0}k^\mu. \tag{1.2.23}$$

1.2.2.2 *Initially at rest*

Suppose the charge is an electron, i.e. $q = -e$, initially at rest in the absence of the laser field. We have $k\cdot p_0 = m\omega$. Its momentum and trajectory can be written in terms of the Lorentz-invariant *dimensionless vector potential*

$$a_0 = \frac{e\sqrt{\langle -A^2\rangle}}{mc^2} = \frac{eE_{\mathrm{rms}}}{mc\omega} \tag{1.2.24}$$

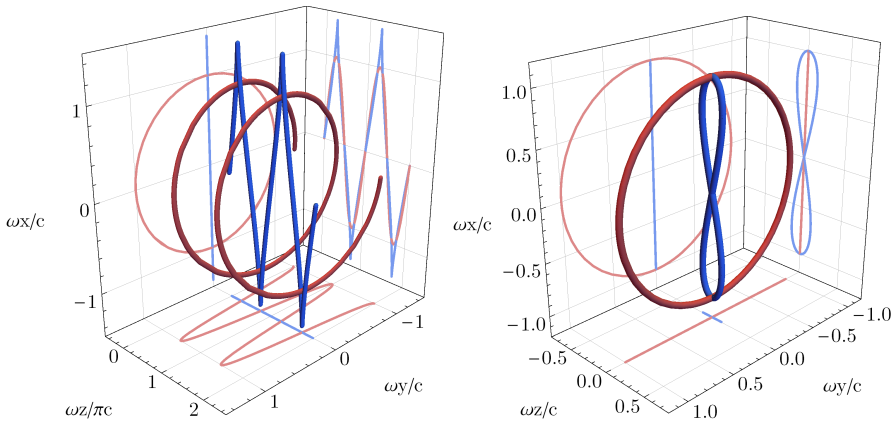

Figure 3: The trajectory of an electron in a plane EM wave propagating along z with normalised vector potential $a_0 = 1$ and angular frequency ω that is (red) circularly polarised, (blue) linearly polarised in the x-direction, as seen in (left) the lab frame and in (right) a frame moving along z with drift velocity $a_0^2 c/(2 + a_0^2)$.

or *strength parameter*. It is defined so that linearly and circularly polarised waves that have the same average intensity I have the same a_0:

$$a_0 = 0.60 \left(\frac{I}{10^{18}\ \mathrm{Wcm}^{-2}} \right)^{1/2} \left(\frac{\lambda}{\mu\mathrm{m}} \right). \tag{1.2.25}$$

The action of the EM wave is to accelerate the electron along $\hat{\mathbf{k}}$; it acquires a longitudinal momentum of

$$\frac{\langle p_\parallel \rangle}{mc} = \frac{a_0^2}{2} \tag{1.2.26}$$

and drift velocity

$$\frac{\langle v_\parallel \rangle}{c} = \frac{a_0^2}{2 + a_0^2} \tag{1.2.27}$$

(on average for linear polarisation, exactly for circular polarisation). We can determine the trajectory in the electron's average rest frame by boosting along $\hat{\mathbf{k}}$ by (1.2.27) and integrating (1.2.21) using $k' \cdot p'_0 = m\omega\sqrt{1 + a_0^2}$. For circular polarisation the electron describes a circle of radius ca_0/ω; for linear polarisation a figure-of-eight, with maximum displacement along the polarisation axis of $\frac{c}{\omega}\sqrt{\frac{2a_0^2}{1+a_0^2}}$ and along the propagation axis of $\frac{c}{\omega}\frac{a_0^2}{4(1+a_0^2)}$. These are illustrated in fig. 3.

We conclude that if the electron is at rest in the absence of the field, a strong laser pulse ($a_0 > 1$) will rapidly accelerate it up to near the speed of light, with typical transverse oscillatory momentum $p_\perp \simeq a_0 mc$. As this leads to electron energies larger than the rest energy mc^2, the condition $I\lambda^2 > 10^{18}$ Wcm$^{-2}\mu$m^2 defines when relativistic effects become important in plasma physics.

1.2.2.3 *Initially ultrarelativistic, counter-propagating*

If instead the electron were ultrarelativistic, with Lorentz factor $\gamma_0 \gg 1$, and propagating backwards into a circularly polarised laser pulse, its transverse momentum would be $p_\perp/mc = a_0$ and in the longitudinal direction, by $k \cdot p_0 = 2\gamma_0 m\omega$,

$$\frac{p_\parallel}{mc} \simeq \frac{a_0^2}{4\gamma_0} - \gamma_0. \tag{1.2.28}$$

If $\gamma_0 \gg a_0 \gg 1$, the longitudinal velocity remains nearly c and the electron trajectory, a helix of radius $(c/\omega)(a_0/2\gamma_0)$, is approximately linear.

1.2.3 *When do radiation losses become significant?*

Electrons in intense laser pulses are rapidly accelerated to relativistic energies; therefore we expect them to radiate by the results of section 1.2.1. The Larmor power (1.2.5) for an electron in a plane EM wave takes the form

$$\mathcal{P} = -\frac{e^4}{6\pi\epsilon_0 m^2 c^5}\left(\frac{k\cdot p}{m}\right)^2 \left(A_1^2\cos^2\phi + A_2^2\sin^2\phi\right). \tag{1.2.29}$$

For a circularly polarised wave $A_1^2 = A_2^2 = -A_0^2$.

The power radiated by a counter-propagating, ultrarelativistic electron with $\gamma \gg 1$ is

$$\mathcal{P} = \frac{e^2(2\gamma a_0 \omega)^2}{6\pi\epsilon_0 c} \tag{1.2.30}$$

which is a factor of $4\gamma^2$ larger that radiated by a charge initially at rest. This is because transforming to the average rest frame of an electron co-moving with the pulse red-shifts the laser field, reducing the four-acceleration and so the radiated power.

Although (1.2.30) is a classical result, it can be recast to make explicit its relation to the quantum-mechanical result that will be outlined in section 3.3.2:

$$\begin{aligned}\mathcal{P} &= \frac{2}{3}\frac{e^2}{4\pi\epsilon_0 \hbar c}\frac{(mc^2)^2}{\hbar}\left(\frac{2\gamma a_0 \hbar\omega}{mc^2}\right)^2 \\ &= \frac{2\alpha}{3}\frac{mc^2}{\tau_c}\eta^2\end{aligned} \tag{1.2.31}$$

where $\alpha \simeq 1/137$ is the fine-structure constant, $\tau_c = \hbar/(mc^2) = 1.288 \times 10^{-21}$ s is the Compton time and η is a dimensionless Lorentz-invariant parameter. We will postpone discussion of η until section 1.4; it will suffice for now to comment that the classical radiated power scales with a_0^2 (i.e. with laser intensity) and the square of the electron energy.

(1.2.31) means that an electron with energy $\mathcal{E}$ colliding with a laser pulse of intensity I and wavelength λ will radiate in a single laser period a fraction of its energy equal to

$$f = 0.42\left(\frac{\mathcal{E}}{100\ \text{MeV}}\right)\left(\frac{I}{10^{22}\ \text{Wcm}^{-2}}\right)\left(\frac{\lambda}{\mu\text{m}}\right). \tag{1.2.32}$$

This energy loss can be substantial in laser-plasmas where electrons propagate anti-parallel to the driving laser field. This can occur in underdense laser-solid interactions, where the radiation pressure of the laser accelerates the electrons, but not the ions, into the target, establishing a space charge field that can re-accelerate the electrons

backwards into the laser field [13]; Brady et al. [21] show that the fraction of laser energy absorbed to radiation in this process $f = 0.1(a_0/100)^2(n/10^{23}\ \mathrm{cm}^{-3})(\lambda/\mu\mathrm{m})$ where n is the electron number density.

Alternatively, we could consider the case in which an intense laser pulse is reflected from an overdense target to form a standing wave. At the nodes $B = 0$, the electric field rotates with constant amplitude at the laser frequency ω and the charge performs circular motion. (1.2.6) with $\mathbf{a} \cdot \mathbf{v} = 0$, $\gamma \simeq a_0$ and $|\mathbf{a}| = c\omega$ leads to a fractional loss of energy per laser period of

$$f = 0.51 \left(\frac{I}{10^{23}\ \mathrm{Wcm}^{-2}} \right)^{3/2} \left(\frac{\lambda}{\mu\mathrm{m}} \right)^2 , \tag{1.2.33}$$

which is consistent with Bell and Kirk [16] who show that copious gamma ray production occurs for laser intensities $> 10^{23}\ \mathrm{Wcm}^{-2}$.

The radiation field carries momentum and so the energy losses given in eqs. (1.2.32) and (1.2.33) should lead to back-reactions on the electron. However, that reaction is not accounted for by the Lorentz force. Indeed, the 0-component of (1.2.20)

$$\frac{1}{c}\frac{\mathrm{d}\mathcal{E}}{\mathrm{d}\phi} = \frac{a_0}{2\gamma_0}\left(p_x \sin\phi - p_y \cos\phi\right) = 0 \tag{1.2.34}$$

vanishes identically for circular polarisation, given the $p_{x,y}$ from section 1.2.2.3. While this is to be expected as the electron trajectory is a circular orbit, we must conclude that the Lorentz force by itself is insufficient to describe the dynamics of charged particles in intense fields.

1.3 CLASSICAL RADIATION REACTION

We have seen that classical electromagnetism predicts substantial energy losses to radiation for accelerating charged particles, but that the back-reaction of those losses is not accounted for by the Lorentz force. This is because in solving the Lorentz force law (1.2.7) for a charge in a plane wave we implicitly assumed that $F^{\mu\nu} = F^{\mu\nu}_{\text{ext}}$ and that the charge moved in response only to the electromagnetic fields generated by *other* sources. We must somehow account for the contribution from its own field $F^{\mu\nu}_{\text{self}}$ by solving a modified equation of motion

$$\frac{\mathrm{d}p^\mu}{\mathrm{d}\tau} = \frac{q}{mc}\left(F^{\mu\nu}_{\text{ext}} + F^{\mu\nu}_{\text{self}}\right)p_\nu. \tag{1.3.1}$$

We face the immediate problem that, for a point-like charge, $F^{\mu\nu}_{\text{self}}$ diverges and so the equation of motion (1.3.1) is apparently physically unacceptable. However, one can proceed by regularisation of the problem [29] or by considering an extended particle [5, sec. C]. In the latter case the physical origin of radiation reaction is an imbalance of the forces acting between constituent parts of the charge, which can only exist if the particle is accelerating; this is called *Lorentz-Abraham* theory [30]. However, as we wish to describe radiation reaction for fundamental particles, one may ask how valid this approach is when the electron has not been measured to have internal structure nor are the associated length scales within the purview of classical physics.

However, taking the point charge limit gives the same result as an alternative approach that considers only conservation laws and associated symmetries. A simple argument is given by Rohrlich [31] as follows: let the equation of motion for a charge in an external electromagnetic field $F^{\mu\nu}$ be

$$m_0\frac{\mathrm{d}u^\mu}{\mathrm{d}\tau} = \frac{q}{c}F^{\mu\nu}u_\nu + \mathcal{F}^\mu_{\text{rr}} \tag{1.3.2}$$

where u^μ is the four-velocity and $\mathcal{F}^\mu_{\rm rr}$ the radiation reaction term. We will not yet identify m_0 with the physical mass of the charge; for now it will be called the *bare mass*. The mass-shell condition $u^2 = c^2$ requires that the force be orthogonal to u; this is satisfied automatically for the Lorentz force by the antisymmetry of the field tensor $F^{\mu\nu}$. Therefore a suitable ansatz for $\mathcal{F}_{\rm rr}$ would be the tensor product of a general four-vector g^μ with

$$P^{\mu\nu} = \eta^{\mu\nu} - \frac{u^\mu u^\nu}{c^2} \tag{1.3.3}$$

which is an operator that projects onto the hyper-plane orthogonal to u. A minimal form for g^μ is

$$g^\mu = Au^\mu + B\frac{\mathrm{d}u^\mu}{\mathrm{d}\tau} + C\frac{\mathrm{d}^2u^\mu}{\mathrm{d}\tau^2} \tag{1.3.4}$$

keeping only linear terms. We can set $A = 0$ by the orthogonality condition; the term proportional to B can be absorbed into the bare mass, renormalising such that $m_0 - B = m$, the physically observed rest mass. C is set by requiring that the term proportional to u^μ reproduces the Larmor formula (1.2.5), with the result that $C = q^2/(6\pi\epsilon_0 c^3)$.

The equation of motion of a charge responding to an external electromagnetic field $F^{\mu\nu}$ and its own radiation field becomes

$$\frac{\mathrm{d}p^\mu}{\mathrm{d}\tau} = \frac{q}{mc}F^{\mu\nu}p_\nu + \frac{q^2}{6\pi\epsilon_0 mc^3}\left[\frac{\mathrm{d}^2p^\mu}{\mathrm{d}\tau^2} + \frac{p^\mu}{(mc)^2}\left(\frac{\mathrm{d}p}{\mathrm{d}\tau}\cdot\frac{\mathrm{d}p}{\mathrm{d}\tau}\right)\right]. \tag{1.3.5}$$

This is called the *Lorentz-Abraham-Dirac (LAD) equation* and was first obtained in covariant form by Dirac [4]. That derivation employs Gauss's theorem to equate the energy-momentum flux across a thin tube around the world-line of a charge with the net flow across the time-like ends of the tube [5]; and features a mass renormalisation necessary to eliminate divergences associated with the point-like nature of

the particle [6]. As the coefficient of the radiation reaction term has units of time, we shall call it τ_{rad}. For an electron it has magnitude $\tau_{\text{rad}} = q^2/(6\pi\epsilon_0 mc^3) = 6 \times 10^{-24}$ s.

This should be the end of the story. However, (1.3.5) possesses pathological solutions that call into question its validity [6]. These include the so-called *runaway* solutions, in which an electron at rest in the absence of an external field accelerates to relativistic velocity in a characteristic time $\sim 10^{-23}$ s. Let us consider motion confined to the x-axis, so that the 0-component of the LAD equation takes the form

$$\frac{\mathrm{d}\mathcal{E}}{\mathrm{d}\tau} = \tau_{\text{rad}} \left\{ \frac{\mathrm{d}^2\mathcal{E}}{\mathrm{d}\tau^2} + \frac{\mathcal{E}}{m^2c^4} \left[\left(\frac{\mathrm{d}\mathcal{E}}{\mathrm{d}\tau} \right)^2 - c^2 \left(\frac{\mathrm{d}p_x}{\mathrm{d}\tau} \right)^2 \right] \right\}. \tag{1.3.6}$$

The mass shell condition requires that $\mathcal{E}^2 - c^2 p_x^2 = (mc^2)^2$. We can guarantee this by setting

$$\frac{\mathcal{E}(\tau)}{mc^2} = \cosh(f(\tau)) \qquad \frac{p_x(\tau)}{mc} = \sinh(f(\tau)) \tag{1.3.7}$$

for some function f. Substituting, we find

$$\sinh(f) \left(\tau_{\text{rad}} \frac{\mathrm{d}^2 f}{\mathrm{d}\tau^2} - \frac{\mathrm{d}f}{\mathrm{d}\tau} \right) = 0. \tag{1.3.8}$$

This system has two solutions; in the first, $f(\tau) = 0$, the charge remains at rest for all time as we would expect. In the second,

$$\frac{\mathcal{E}}{mc^2} = \cosh \left[A \exp \left(\frac{\tau}{\tau_{\text{rad}}} \right) + B \right] \tag{1.3.9}$$

for arbitrary constants A, B. The charge is therefore capable of accelerating itself to relativistic energies in a few τ_{rad}, manifestly violating the conservation of energy.

While runaway behaviour can be eliminated by adding the constraint that in the far future the acceleration tends to zero (once all forces have finished acting), this introduces a new unphysical phenomenon called

pre-acceleration; it is found that the acceleration at time t depends on the acceleration at all future times [6]. Various authors have attempted to address these problems by proposing alternative formulations of the radiation reaction force: they include Ford and O'Connell [32], Mo and Papas [33], Bonnor [34] and Sokolov [35] (details can be found in the review by Burton and Noble [6]). They each have their particular advantages and disadvantages. However, we will see later that to first order in QED, they are not distinguishable from each other.

Pathologies arise in (1.3.5) because of the term that depends on the derivative of the particle's four-acceleration. This can be eliminated by reducing the order of the equation with an iterative procedure developed by Landau and Lifshitz [36]. This exploits the small size of τ_{rad} to treat the radiation reaction as a perturbation to the charge's motion, assuming that it is much smaller than the Lorentz force in the charge's instantaneous rest frame.

By substituting $\frac{\mathrm{d}p^\mu}{\mathrm{d}\tau} \to \frac{q}{mc} F^{\mu\nu} p_\nu$ into the right hand side of (1.3.5) we obtain an equation of motion that is correct up to $\mathcal{O}(\tau_{\text{rad}})$

$$\frac{\mathrm{d}p^\mu}{\mathrm{d}\tau} = \frac{q}{mc} F^{\mu\nu} p_\nu + \mathcal{F}^\mu_{\text{LL}} + \mathcal{O}\left(\tau^2_{\text{rad}}\right). \tag{1.3.10}$$

This is called the Lorentz-Abraham-Dirac equation in the Landau-Lifshitz prescription. The second term $\mathcal{F}^\mu_{\text{LL}}$ is the *Landau-Lifshitz force*

$$\mathcal{F}^\mu_{\text{LL}} \equiv \frac{q^3}{6\pi\epsilon_0 m^3 c^4} \Big[\left(\partial_\sigma F^{\mu\nu}\right) p_\nu p^\sigma + \frac{q}{c} F^{\mu\nu} F_{\nu\sigma} p^\sigma + \frac{q}{m^2 c^3} \left(F^{\nu\sigma} p_\sigma\right)^2 p^\mu \Big]. \tag{1.3.11}$$

The equation of motion (1.3.10) is valid for an electron when the external EM field's characteristic frequency and magnitude (as measured in the electron rest frame) are much smaller than the inverse Compton time and $m^2c^4/e^3 = 1.6 \times 10^{30}$ Vm^{-1} respectively [36]. It is first-order in the momentum and so free from unphysical solutions. Indeed, it can

be solved exactly for plane-wave external EM fields that have arbitrary shape and polarisation [37]. The third term of (1.3.11) is dominant for ultrarelativistic particles [13] and is directed antiparallel to the velocity whether the charge is positive or negative.

Ilderton and Torgrimsson [38] have derived radiation reaction in the classical limit of strong-field QED; their results, correct to first order in the fine-structure constant α, are consistent with both the LAD and Landau-Lifshitz equations.

There are subtleties within the framework presented which have yet to be resolved: for a charge undergoing constant acceleration, i.e. $\left(\frac{\mathrm{d}u}{\mathrm{d}\tau}\right)^2 = -g^2$ for constant g, the Larmor power (1.2.5) is non-zero but the radiation reaction force in (1.3.5) vanishes. If that is the case, how is energy conserved and, if g arises from a gravitational field, is there a violation of the equivalence principle?

This apparent contradiction has led such distinguished physicists as Feynman and von Laue to conclude that a uniformly accelerating charge does *not* radiate. This remains controversial: Fulton and Rohrlich [39], Eriksen and Øyvind [40] conclude that the charge does radiate and that the energy lost is supplied from the *Schott energy* [41] of the particle (energy associated with the charge's bound fields, which do not respond rigidly to applied acceleration [42]) rather than its kinetic energy, hence the absence of radiation reaction; Singal [43] argues that there is no radiation; and Heras and O'Connell [44] argue that radiation is only emitted during the transition to and from hyperbolic motion. In the first of these cases, the equivalence principle is not violated as radiation is emitted into a region of spacetime inaccessible to co-moving and accelerated observers [45]. A calculation from QED has shown that the motion of a charge in bounded hyperbolic motion is indeed given by the LAD equation (1.3.5) to lowest order in α [46].

There is a similar debate about whether the Unruh effect [47], the prediction that in a reference frame with proper acceleration a the quantum vacuum is observed to be a black-body radiation field with temperature $T = \hbar a/(2\pi c k_{\mathrm{B}})$, leads to Unruh radiation: does a particle scattered by the thermal background emit radiation in the lab frame? Narozhny et al. [48] demur, though disagreement can be seen in Unruh's comment on the same [49] and the authors' reply thereto [50]; the difficulty here arises from the choice of boundary conditions attached to the problem [51].

In reality unbounded hyperbolic motion does not exist, and the Larmor power and Landau-Lifshitz equation of motion are widely accepted [6]. Nevertheless the debate outlined previously does raise questions about the interpretation of radiation reaction in a classical framework. We saw that this was characterised by a time $\tau_{\mathrm{rad}} = q^2/(6\pi\epsilon_0 mc^3)$, which for an electron is approximately the time taken for light to cross a classical electron radius. This is smaller than the Compton length by a factor of $\alpha \simeq 1/137$ and so well within the realm of quantum electrodynamics. One may therefore ask whether the difficulties presented could not be resolved within that framework. We will continue by showing as classical radiation reaction becomes important so too do QED effects.

1.4 STRONG-FIELD QED

We found in section 1.2.3 that the magnitude of radiation loss for an electron in a plane wave with strength parameter a_0 and frequency ω was controlled by a dimensionless, Lorentz-invariant parameter η. For the charge initially at rest it was given by

$$\eta = \frac{a_0 \hbar\omega}{mc^2} = \frac{E}{E_{\mathrm{Sch}}} \tag{1.4.1}$$

and for the counter-propagating ultrarelativistic charge by

$$\eta = \frac{2\gamma a_0 \hbar\omega}{mc^2} = \frac{2\gamma E}{E_{\text{Sch}}}. \tag{1.4.2}$$

These have been written in terms of the laser's electric field strength E and a quantum-mechanical characteristic field strength

$$E_{\text{Sch}} = \frac{m^2c^3}{e\hbar} = 1.326 \times 10^{18}\ \text{Vm}^{-1} \tag{1.4.3}$$

which we call the *Schwinger field* [52]; it is also referred to as the *Sauter field* [53] and the *critical field*. It does work equal to the electron rest energy mc^2 over the Compton length $\lambda\!\!\!^{-}_{\text{c}} = \hbar/mc$. The equivalent magnetic field strength is $B_{\text{Sch}} = E_{\text{Sch}}/c = 4.41 \times 10^9$ T and the equivalent intensity $I_{\text{Sch}} = 2.3 \times 10^{29}\ \text{Wcm}^{-2}$, which is seven orders of magnitude beyond the current intensity frontier [1, 54].

Fields of comparable magnitude do exist in nature. They can be found in pulsar magnetospheres [55], with typical magnitude $B \sim 0.1B_{\text{Sch}}$ [56]. A pulsar is a rapidly rotating neutron star, formed after the supernova of a massive star and the collapse of its core. Retaining most of the parent star's angular momentum, but with a much smaller radius (typically tens of km), means their rotation velocity is very large [57]; the rotation of the dipole magnetic field drives electromagnetic waves along the magnetic axis as well as a relativistic wind of charged particles. Even larger magnetic fields, of order 10-100B_{Sch}, are believed to exist near magnetars [58, 59]: neutron stars whose magnetic fields were amplified by a dynamo process just after their creation by stellar core collapse. The plasma present in the magnetospheres of these objects interacts with a near- or super-critical field, which fact has prompted substantial interest in QED processes in intense fields [60, 61, 62].

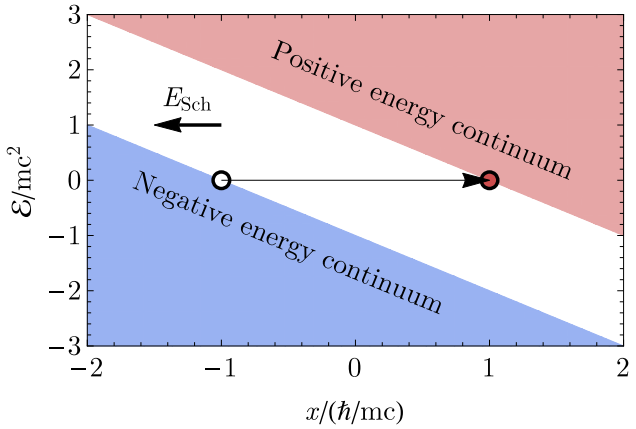

Figure 4: Vacuum pair production via the Schwinger mechanism, as seen in the concept of the Dirac sea. The electric field $-E_{\mathrm{Sch}}\hat{\mathbf{x}}$ biases the $2mc^2$ mass gap to allow the tunnelling of an electron from a negative to a positive energy state, creating a real electron-positron pair.

The magnitude of E_{Sch} is significant as it suggests the possibility of electron-positron pairs directly from the vacuum. The QED vacuum is empty of real particles but contains quantum fluctuations: virtual particles whose lifetime t is governed by the uncertainty principle $\Delta E \Delta t \geqslant \hbar/2$ [63]. A strong electric field with $E = E_{\mathrm{Sch}}$ can supply $2mc^2$ over the typical separation of the virtual pair $\lambda\!\!\!^{-}_{\mathrm{c}}$, pulling these particles onto the mass shell. This can be understood in the Dirac sea picture as a tunnelling process, which is shown in fig. 4. This non-perturbative result of QED was first obtained by Sauter [53], Schwinger [52]. Other strong-field–induced non-linearities in QED, such as vacuum polarisation, were predicted by Heisenberg and Euler [64].

We can understand the meaning of η by writing it in a manifestly covariant way. Substituting (1.2.7) into (1.2.5) and recasting as in (1.2.31), we find that

$$\eta = \frac{\sqrt{-\left(F^{\mu\nu}p_\nu\right)^2}}{mcE_{\mathrm{Sch}}} \tag{1.4.4}$$

compares the electric field strength in the rest frame of the electron to that of the Schwinger field [16]. While we cannot create fields of critical strength in laboratory, we can observe them indirectly if the electrons are accelerated to energies such that $\eta \sim 1$. (1.2.31) suggests that as

radiative energy losses and radiation reaction becomes important, so too will QED effects such as pair production.

In an intense laser-plasma interaction, we would expect the electrons to be accelerated up to $\gamma \simeq a_0$. The typical η would then be

$$\eta = 0.18 \left(\frac{I}{10^{23}\ \mathrm{Wcm}^{-2}} \right) \left(\frac{\lambda}{\mu\mathrm{m}} \right). \tag{1.4.5}$$

We have already seen in (1.2.33) that such laser intensities will lead to substantial radiative energy losses. It is reasonable, therefore, to expect that the laser-plasma physics studied in the next generation of high-intensity laser facilities [2, 3] will be substantially altered by gamma ray production, radiation reaction and electron-positron pair production.

1.5 OUTLINE

In chapter 2 I will discuss the strong-field QED process of *non-linear Compton scattering*, which is the inelastic scattering of an electron from multiple photons. This is the first QED process to become significant as $a_0 > 1$; we will explore various aspects of the dynamics and how it has been observed in experiment.

In chapter 3 I will extend that analysis to describe how QED-plasmas may be modelled when $a_0 \gg 1$. The two fundamental process are *synchrotron photon emission* and *Breit-Wheeler pair creation*. We will see how the recoil from the former can be related to classical radiation reaction and what quantum corrections must be made. Then we will show how QED processes may be included in simulations of laser-plasmas, focusing on particle-in-cell (PIC) codes.

Finally, in chapter 4, I will show that QED effects may be observed in an experiment that could be performed in today's PW laser facilities.

The verification of the QED-plasma model will be vital in benchmarking simulations and theoretical predictions of the laser-plasmas that will be studied in high-intensity laser experiments in the coming decade.

2

NON-LINEAR COMPTON SCATTERING

2.1 INTRODUCTION

While in a classical calculation radiation reaction is fraught with subtleties, it arises much more naturally in quantum electrodynamics (QED). This is because classically there is a distinction drawn between particles and fields; in QED, no such distinction exists and both the electromagnetic and electron fields are sources of quantised excitations i.e. the particles we observe experimentally.

One of the most elementary processes of QED is Compton scattering: the inelastic scattering of a single electron and a single photon. The cross-section was first calculated by Klein and Nishina [65] in 1928, including both tree-level Feynman diagrams of $\mathcal{O}(\alpha^2)$, where $\alpha \simeq 1/137$ is the fine-structure constant; the shift in photon energy was first observed by Compton [66] in 1923. The conservation of energy and momentum applied to the electron-photon system gives the recoil of the electron, and so radiation reaction in a straightforward way.

However, in high-intensity electromagnetic fields, the nature of Compton scattering changes as the background photon density becomes very large. The number of photons in a cubic laser wavelength

$$N = 5 \times 10^{18} \left(\frac{a_0}{100}\right)^2 \left(\frac{\lambda}{\mu\mathrm{m}}\right)^2 \gg 1 \tag{2.1.1}$$

with the consequence that the electron is likely to interact with more than one during the emission process. QED reaction rates in this regime must be studied within the Furry [7] picture of QED [10]. In this frame-

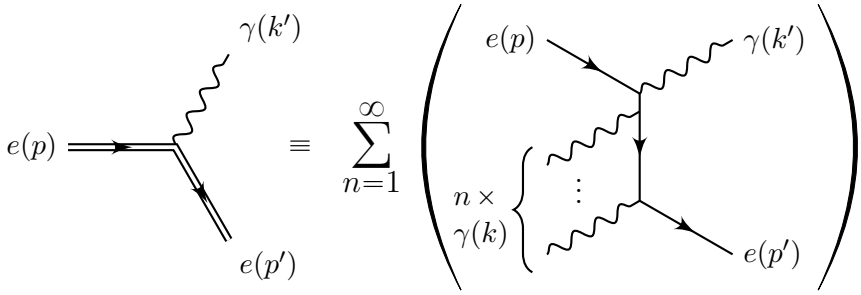

Figure 5: An electron (four-momentum p^μ), embedded in an intense electromagnetic wave (wavevector k^μ, four-potential A^μ), emits a photon with four-momentum k'^μ, as considered in strong-field QED. The electron's interaction with the background field, i.e. the absorption and re-emission of an arbitrary number of laser photons, is accounted for exactly by using Volkov basis states and propagators, as represented by the double lines. (Adapted from Mackenroth and Di Piazza [67].)

work, the photon field is divided into a large, classical part and a smaller, fluctuating part [68]

$$A^\mu \to A^\mu_{\text{classical}} + A^\mu_{\text{SFQED}}. \tag{2.1.2}$$

The equations of motion that arise from the QED Lagrangian [63]

$$\mathcal{L} = \overline{\psi}(i\not{\partial} - e\not{A} - m)\psi - \frac{1}{4}F_{\mu\nu}F^{\mu\nu} \tag{2.1.3}$$

where ψ is the Dirac (electron) field, $\overline{\psi}$ its adjoint, and 'slashed' quantities are shorthand for $\not{Q} \equiv \gamma \cdot Q$ where γ^μ are the four Dirac matrices, describe the electron's exact interaction with the classical background and its interactions with the quantised radiation field A^μ_{SFQED}. The former is handled by solving the Dirac equation for the electron basis states; the latter with perturbation theory. This is illustrated in fig. 5.

However, deriving those basis states can only be done analytically for a limited set of electromagnetic fields with high symmetry. If a plane wave is chosen, the states are called Volkov [69] states, which are characterised by an intensity-dependent momentum q. As a true plane

wave must be infinitely large, the probability for an interaction will be unity; therefore differential probability *rates* are calculated instead.

While a full derivation of the strong-field QED rate for non-linear Compton scattering (NLCS) is beyond the scope of this thesis, we will consider various details of the calculation that illustrate the practical effects of increasing non-linearity, and then discuss an experiment by which they could be measured.

We use natural units throughout this chapter, i.e. we take $\hbar = c = \epsilon_0 = 1$. The unit of electric charge e is defined through the fine-structure constant $\alpha = e^2/4\pi \simeq 1/137$.

2.2 QUASI-MOMENTUM AND THE MASS SHIFT

In deriving the cross-section for standard Compton scattering, the initial and final states of the electron are given by plane waves

$$\psi_p = u(p) \exp(-ip \cdot x) \tag{2.2.1}$$

where p is the electron four-momentum and $u(p)$ is a Dirac spinor satisfying $(\not{p} - m)u(p) = 0$ [63, p. 45]. The photon wavefunctions carry a similar dependence $\exp(-ik \cdot x)$, where k is the four-frequency [63, p. 123].

Each particle in the initial and final state contributes such a phase factor (complex conjugated for the particles in the final state) to the matrix element. Integrating the resulting product over all space leads to a δ-function that enforces the conservation of four-momentum for the matrix element $\mathcal{M}$

$$\mathcal{M} \sim \delta^{(4)}(p + k - p' - k'). \tag{2.2.2}$$

Setting the argument of the δ-function to zero describes the kinematics of the scattering event.

However, in an intense electromagnetic wave, the initial and final states in a scattering problem no longer comprise vacuum waves of the type shown in (2.2.1). The photon density is sufficiently high that we must account for continuous absorption and re-emission along the electron trajectory by including an external field in the Dirac equation:

$$\left(i\not{\partial} - e\not{A} - m\right)\psi_p = 0 \tag{2.2.3}$$

Here A^μ is the four-potential of an unquantised, classical EM field.

It is not possible to solve (2.2.3) for arbitrary fields. However, Volkov [69] obtained an exact solution for the case of a plane electromagnetic wave, where A^μ is a function of one invariant only: $\phi \equiv k \cdot x$. The positive energy solutions are given by

$$\psi_p = \left(1 + \frac{e\not{k}\not{A}}{2k\cdot p}\right) u(p) \exp\left[-ip\cdot x - i\int_0^\phi \left(\frac{eA\cdot p}{k\cdot p} - \frac{e^2A^2}{2k\cdot p}\right)\mathrm{d}\phi\right]. \tag{2.2.4}$$

The spinor $u(p)$ is unchanged from that in (2.2.1) and we identify the four-vector p with the momentum of the electron distant from (or in the absence of) the field [9].

In a linearly polarised EM wave, $A^\mu = a^\mu \cos\phi$; its magnitude is related to the normalised vector potential by $a_0^2 = e^2(-a^2)/2m^2$. The factor of 2 arises because a_0 is generally defined by the r.m.s electric

field (i.e. average intensity), which is smaller than the peak field by $\sqrt{2}$. Then (2.2.4) takes the form

$$\psi_p = \left(1 + \frac{e\not{k}\not{A}}{2k\cdot p}\right) u(p) \exp\left[-i\left(p - \frac{e^2a^2}{4k\cdot p}k\right)\cdot x + i\frac{a\cdot p}{k\cdot p}\sin\phi + i\frac{e^2a^2}{8k\cdot p}\sin 2\phi\right]. \quad (2.2.5)$$

The second and third terms in the exponent of (2.2.5) vanish on averaging over the wave phase, leaving behind a phase factor that is the product of the electron four-position x and a four-vector with the dimensions of momentum. That four-vector is the electron's average kinetic momentum

$$q = \langle \overline{\psi}_p \left(i\not{\partial} - eA\right) \psi_p \rangle \quad (2.2.6)$$

where the angled brackets denote the mean over phase ϕ and the adjoint spinor $\overline{\psi}_p \equiv \psi_p^\dagger \gamma^0$. It is referred to as the *quasi-momentum* [70, 71]

$$q = p + \frac{a_0^2 m^2}{2k\cdot p}k. \quad (2.2.7)$$

and its magnitude gives the electron's effective, or shifted, mass

$$m_*^2 \equiv q^2 = m^2\left(1 + a_0^2\right). \quad (2.2.8)$$

When the states in (2.2.5) are used to calculate matrix elements for quantised interactions in a plane EM wave, the resulting conservation law (analogous to (2.2.2)) is defined in terms of q, rather than the electron external momentum p [9].

Although it has arisen here quantum-mechanically, we can understand the quasi-momentum classically by referring to section 1.2.2. We

found that the four-momentum p (initially p_0) of an electron in a plane wave with four-potential A is

$$p = p_0 + eA - \frac{eA \cdot p_0}{k \cdot p_0} k - \frac{e^2 A^2}{2k \cdot p_0} k \tag{2.2.9}$$

using (1.2.23) with $q = -e$ and setting $c = 1$. Averaging over the phase ϕ gives the same result as (2.2.7); the apparent intensity dependence of the mass in (2.2.8) arises from the electron's quiver motion in the oscillating laser fields.

Finally, we note that since the quasi-momentum is the momentum averaged over a wave period, by employing it in the conservation of momentum we implicitly assume that the scattering event occurs throughout a region of at least that length. Indeed this is the case, at least for $a_0 \lesssim 1$. However, we will defer discussion of this region, which we call the 'formation length' (Ritus [9] refers to it as the 'coherence interval'), until section 2.7. For now, we continue by describing the kinematics of a NLCS event.

2.3 KINEMATICS

In the case of non-linear Compton scattering (NLCS), where the electron is embedded in a plane wave with four-frequency k, the conservation of momentum analogous to (2.2.2) is

$$q + nk = q' + k'. \tag{2.3.1}$$

q, q' are the initial and final quasi-momenta of the electron and k' the four-frequency of the scattered photon. The integer quantity n, which arises as a Fourier index in the evaluation of the matrix element [9], can be identified as the number of field photons that are absorbed by the electron when it emits a single, higher-energy photon.

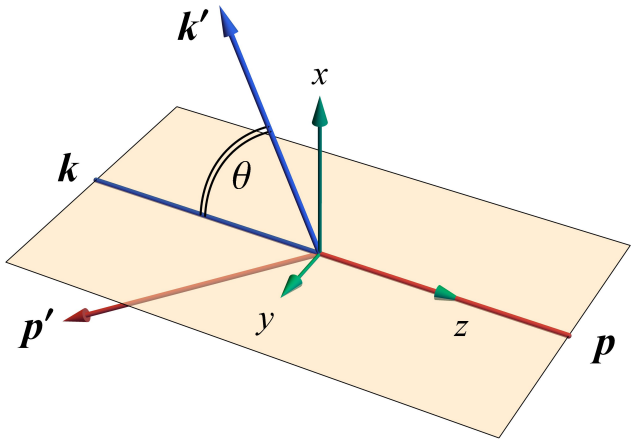

Figure 6: Diagram of a non-linear Compton scattering event in the lab frame: (red, solid) an electron with initial and final momentum $\mathbf{p}$ and $\mathbf{p}'$ and (blue) the scattered photon with momentum $\mathbf{k}'$. θ is the angle between $\mathbf{p}$ and $\mathbf{k}'$, which two vectors define the x-z plane.

Consider an electron propagating antiparallel to a plane EM wave with frequency ω, wavevector k and strength parameter a_0, as shown in fig. 6. This process differs from standard Compton scattering in two ways: the order of interaction can be arbitrarily large, i.e. $n \geqslant 1$; and the electron experiences a 'mass shift' caused by the continuous absorption and re-emission of laser photons, which is accounted for by the quasi-momentum q.

Dotting (2.3.1) with k and using $k \cdot q' = k' \cdot q$, we have

$$nk \cdot q = k' \cdot q + nk \cdot k'. \tag{2.3.2}$$

By the definition of quasi-momentum (2.2.7), $k \cdot q = k \cdot p$ and $k \cdot q' = k \cdot p'$:

$$nk \cdot q = k' \cdot p + \left(n + \frac{a_0^2 m^2}{2k \cdot q}\right) k \cdot k'. \tag{2.3.3}$$

The situation of interest to us is *inverse* Compton scattering of an ultrarelativistic electron, for which its external energy $\mathcal{E} \gg m$. The

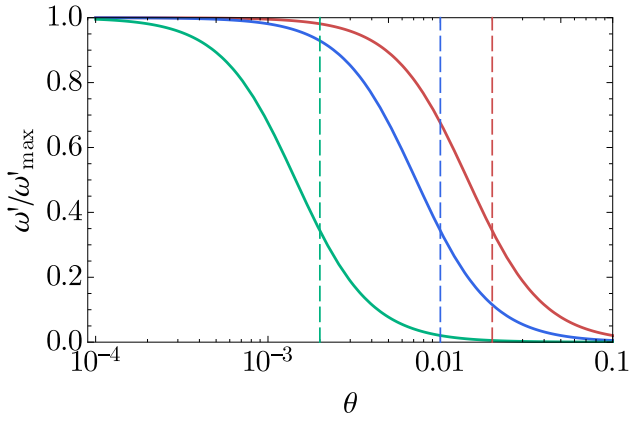

Figure 7: The energy of a photon emitted at an angle θ by an electron with energy (red) 50, (blue) 100 and (green) 500 MeV colliding with a plane wave with frequency 1 eV and $a_0 = 1$, as given by (2.3.4) and (dashed) the angle $1/\gamma$ for each electron.

energy of the scattered photon in terms of its scattering angle θ, the electron Lorentz factor γ and the invariant u is therefore

$$\frac{\omega'}{\mathcal{E}} = \frac{nu}{1 + nu - \left(1 + nu - \frac{4\gamma^2}{1+a_0^2}\right)\sin^2\frac{\theta}{2}} \tag{2.3.4}$$

where

$$u \equiv \frac{2k \cdot q}{q^2} \simeq \frac{4\mathcal{E}\omega}{m^2(1+a_0^2)}. \tag{2.3.5}$$

(2.3.4) is plotted in fig. 7; we can see that the most energetic photons are strongly beamed along $\theta = 0$, parallel to the electron momentum, into a cone with opening half-angle $\sim 1/\gamma$; we will see in section 2.5 that this applies to the total radiated power as well. The maximum photon energy is

$$\frac{\omega'_{\max}}{\mathcal{E}} = \frac{nu}{1+nu}. \tag{2.3.6}$$

If n is large, the fraction of the electron energy carried off by a photon spans the entire range $[0, 1]$; therefore the recoil due to emission cannot be neglected.

It can also be shown that the position of the first Compton edge becomes intensity-dependent as a_0 increases. Taking $n = 1$ and $u \ll 1$, we have

$$\omega'_{\max} = \mathcal{E}u = \frac{4\gamma^2\omega}{1 + a_0^2}. \tag{2.3.7}$$

where $\gamma = \mathcal{E}/m$ is the Lorentz factor of the electron. In the low-intensity limit, this reproduces the well-known inverse Compton upshift of $4\gamma^2$. However, at higher intensities, the electron behaves as though it were heavier by a factor $\sqrt{1 + a_0^2}$, reducing the energy of the emitted photon. We will discuss in section 2.5 how the combination of the mass shift and the advent of higher-order interactions affects the scaling of the radiated power.

2.4 THE SCATTERING RATES

The full calculation of the NLCS rate is given in Ritus [9]. In general it depends on the wave polarisation, unlike standard Compton scattering; here we quote the results for circularly and linearly polarised waves [71].

In natural units, the differential probability rate for an electron with energy $\mathcal{E}$ to scatter off n photons with frequency ω in a plane wave with normalised vector potential a_0, producing a scattered photon with energy $\omega' = x\mathcal{E}$ is

$$\frac{\mathrm{d}W_n}{\mathrm{d}x} = \frac{\alpha m^2}{4\mathcal{E}}\left[-4J_n^2 + a_0^2\left(1 - x + \frac{1}{1-x}\right)\right.$$
$$\left.\left(J_{n-1}^2 + J_{n+1}^2 - 2J_n^2\right)\right] \tag{2.4.1}$$

for circular polarisation and

$$\frac{\mathrm{d}W_n}{\mathrm{d}x} = \frac{2\alpha m^2}{\pi\mathcal{E}}\int_0^{\pi/2}\left[-A_0^2 + a_0^2\left(1 - x + \frac{1}{1-x}\right)\right.$$
$$\left.\left(A_1^2 - A_0A_2\right)\right]\mathrm{d}\varphi \tag{2.4.2}$$

for linear polarisation. These are both unpolarised rates, i.e. an average has been taken over the spin states of the electron and high energy photon.

Here we use the shorthand $J_n \equiv J_n(z)$ and $A_i \equiv A_i(n, a, b)$. The argument of the Bessel function z is given by

$$z = \frac{2a_0}{\sqrt{1+a_0^2}} \frac{\sqrt{x\left(nu - (1+nu)x\right)}}{u(1-x)}. \tag{2.4.3}$$

The A_i functions are defined

$$A_i(n, a, b) \equiv \frac{1}{\pi} \int_0^\pi \cos^i \phi \, \cos\left[(a + 2b\,\cos\phi)\sin\phi - n\phi\right] \, \mathrm{d}\phi \tag{2.4.4}$$

and their arguments a, b are given by

$$a = \frac{\sqrt{8}Qna_0}{1+a_0^2+Q^2}\cos\varphi \qquad b = -\frac{(n/2)a_0^2}{1+a_0^2+Q^2} \tag{2.4.5}$$

where

$$Q^2 = (1+a_0^2)\left[nu\left(\frac{1}{x}-1\right)-1\right]. \tag{2.4.6}$$

In both cases u is as defined in (2.3.5). a_0, the normalised vector potential of the background wave, is defined by the root-mean-square electric field

$$a_0 = \frac{eE_{\mathrm{rms}}}{m\omega} \tag{2.4.7}$$

i.e. by the average intensity $I = E_{\mathrm{rms}}^2$. The fraction of energy transferred from the electron to the scattered photon $x \in [0, x_{\mathrm{max}}]$, where

$$x_{\mathrm{max}} = \frac{nu}{1+nu}. \tag{2.4.8}$$

Outside this range the rates (2.4.1) and (2.4.2) are zero.

The total NLCS rate is obtained by summing over all the harmonics given by (2.4.1) and (2.4.2). This sum is convergent as the contribution

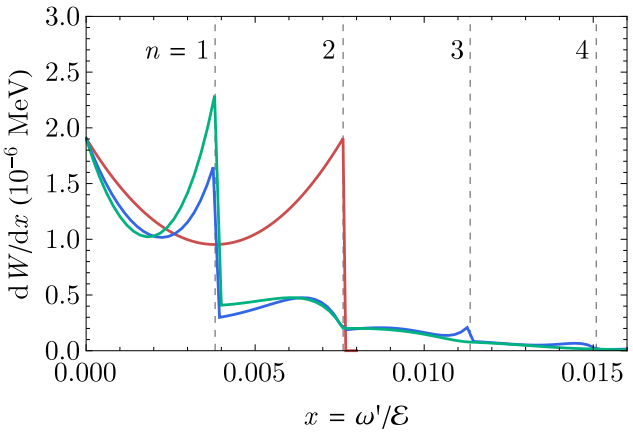

Figure 8: The differential rates eqs. (2.4.1) and (2.4.2) at which an electron with energy $\mathcal{E} = 500$ MeV, colliding with a (blue) linearly polarised and (green) circularly polarised plane EM wave with frequency $\omega = 1$ eV and strength parameter $a_0 = 1$, produces photons with energy $\omega' = x\mathcal{E}$. (Wave parameters equivalent to a wavelength of 1.2 μm and an intensity of 1.8×10^{18} Wcm^{-2}.) (red) The differential rate of *linear*, i.e. Klein-Nishina, Compton scattering (2.4.10) for the same parameters. (grey, dashed) The maximum energies for each harmonic; the maximum for linear Compton scattering is aligned with the $n = 2$ edge at $a_0 = 1$.

from high orders is strongly suppressed: for large n the Bessel functions J_n satisfy [72]

$$J_n(z) \simeq \frac{1}{\sqrt{2\pi n}} \left(\frac{ez}{2n}\right)^n . \tag{2.4.9}$$

Figure 8 illustrates the typical structure of the photon spectrum from NLCS. We can see two non-linear effects: the reduction in energy of the Compton edges caused by the mass shift and the presence of harmonics with $n > 1$.

At low intensities $a_0 \ll 1$ we would expect the differential rates (2.4.1) and (2.4.2) for $n = 1$ to reproduce the Klein-Nishina result [65] which is independent of the polarisation of the initial photons.

For $a_0 \ll 1$, the differential NLCS rate for $n = 1$ is

$$\frac{\mathrm{d}W}{\mathrm{d}x} = \frac{\alpha m^2}{4\mathcal{E}} a_0^2 \left[\frac{(2+u)^2}{u^2} + \frac{4}{u^2(1-x)^2} - \frac{8+4u+u^2}{u^2(1-x)} - x \right] + \mathcal{O}(a_0^4) \tag{2.4.10}$$

and the total rate, integrating over $0 \leqslant x \leqslant u/(1+u)$,

$$W = \frac{\alpha m^2}{4\mathcal{E}} a_0^2 \left[\frac{1}{2} + \frac{8}{u} - \frac{1}{2(1+u)^2} + \left(1 - \frac{4}{u} - \frac{8}{u^2}\right) \ln(1+u) \right] + \mathcal{O}\left(a_0^4\right) \quad (2.4.11)$$

where u becomes

$$u = \frac{4\mathcal{E}\omega}{m^2}. \quad (2.4.12)$$

2.5 THE RADIATED POWER

Let $\mathcal{P}_n = \int \omega' \, \mathrm{d}W_n$ be the instantaneous power radiated by an electron in non-linear interactions of order n. Then the total power

$$\mathcal{P} = \sum_{n=1}^{\infty} \mathcal{P}_n = \mathcal{E} \sum_{n=1}^{\infty} \int_0^{x_{\max}} x \frac{\mathrm{d}W_n}{\mathrm{d}x} \, \mathrm{d}x \quad (2.5.1)$$

where we have used the definition $\omega' = x\mathcal{E}$.

For $a_0 \ll 1$, the power can be derived from the Klein-Nishina rate. Multiplying (2.4.10) by $x\mathcal{E}$ and integrating, we obtain for the Klein-Nishina power

$$\mathcal{P}_{\mathrm{kn}} = \frac{\alpha m^2}{4} a_0^2 \left[-\frac{5}{6} + \frac{12}{u} - \frac{1}{1+u} - \frac{1}{2(1+u)^2} + \frac{1}{3(1+u)^3} + \left(1 - \frac{4}{u} - \frac{12}{u^2}\right) \ln(1+u) \right] \quad (2.5.2)$$

where u is as given in (2.4.12). $\mathcal{P}_{\mathrm{kn}}$ increases quadratically with a_0. We can understand this scaling by recalling that the energy loss is dominated by photons at the Compton edge, which have energy $4\gamma^2\omega$. This is constant with respect to a_0, so the total radiated power depends only on the product of the total Compton cross-section and the photon number density in the wave. While the former is independent of a_0, the latter is proportional to intensity and so to a_0^2.

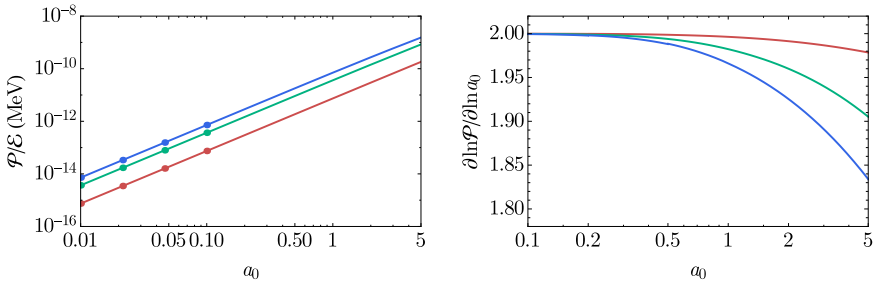

Figure 9: (left) The total power (2.5.1) radiated in NLCS by an electron with energy (red) 100, (green) 500 and (blue) 1000 MeV colliding with a circularly polarised EM wave with frequency $\omega = 1$ eV and given strength parameter a_0. Points give the Klein-Nishina power (2.5.2). (right) The exponent of a_0 in $\mathcal{P}$ for the same parameters.

For $a_0 \gtrsim 1$, we expect the scaling of the NLCS power (2.5.1) to be more complicated due to the onset of non-linear effects. While the mass shift acts to lower the overall power as a_0 increases, the growing number of high harmonics that can be accessed will act to compensate this loss.

Figure 9 gives the instantaneous power $\mathcal{P}$ (2.5.1) and m, its scaling with a_0, for ultrarelativistic electrons colliding with a circularly polarised plane EM wave, comparing it to the Klein-Nishina power (2.5.2). Using $\mathcal{P} \sim a_0^m$, we can define m by

$$m = \frac{\partial \ln \mathcal{P}}{\partial \ln a_0}. \tag{2.5.3}$$

If $a_0 \ll 1$, we can see that across the range of energies the exponent $m = 2$ and the power matches that given by the Klein-Nishina rate. In fact even at $a_0 = 1$ the Klein-Nishina power is within 2% of the correct value, despite the fact that the predicted photon spectra are fundamentally different (as can be seen in fig. 8). As the field strength increases further, m falls below 2, and the growth in $\mathcal{P}$ is suppressed. This suppression will be discussed fully in section 3.3.2 once we have introduced the quantum synchrotron function.

In section 2.3 we derived a one-to-one relation between the energy of the radiated photon and its scattering angle and found that the energy

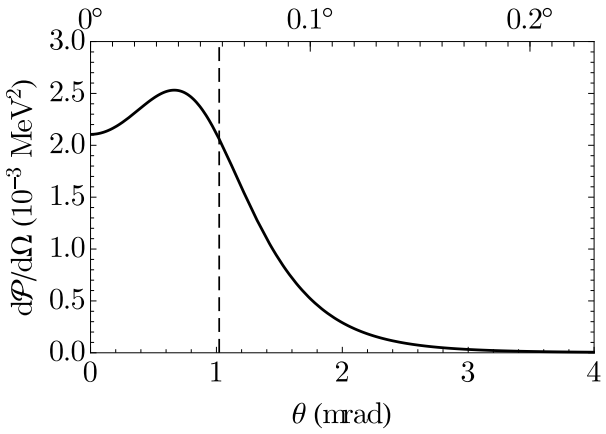

Figure 10: (black) The angular power spectrum (2.5.4) for an electron with energy 500 MeV colliding with a circularly polarised EM wave with frequency $\omega = 1$ eV and strength parameter $a_0 = 1$ and (black, dashed) the angle $1/\gamma$, where γ is the Lorentz factor of the electron.

was maximised for scattering in the forward direction. We find that the radiated power is strongly beamed in the forward direction as well; the power radiated per unit solid angle is

$$\frac{\mathrm{d}\mathcal{P}}{\mathrm{d}\Omega} = \frac{\mathcal{E}}{2\pi \sin\theta} \sum_{n=1}^{\infty} x \left|\frac{\mathrm{d}x}{\mathrm{d}\theta}\right| \frac{\mathrm{d}W_n}{\mathrm{d}x} \tag{2.5.4}$$

where, for each n in the sum, x and θ are related by (2.3.4). This is plotted in fig. 10, which shows that most of the radiation is confined to a cone with opening angle $\sim 2/\gamma$ pointed along the electron's direction of propagation. For ultrarelativistic electrons undergoing nonlinear Compton scattering, it is therefore a good approximation to treat the photon as being emitted parallel to the electron momentum.

In evaluating the NLCS power, we should in general take the sum in (2.5.1) to arbitrarily large n. However, as each extra harmonic contributes a decreasing amount to the total power, we impose a cutoff $n_{\max}$ which is set so that the power converges. We choose $n_{\max}$ to be the smallest m that satisfies

$$\mathcal{P}_m < 10^{-6} \sum_{n=1}^{m} \mathcal{P}_n. \tag{2.5.5}$$

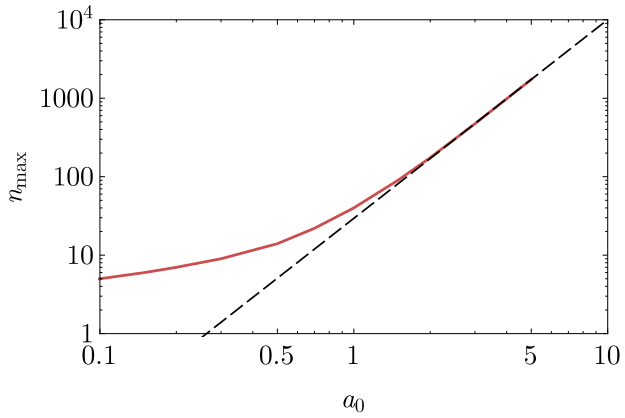

Figure 11: (red) The number of non-linear orders that must be included for the instantaneous power (2.5.1) to converge and (black, dashed) an exponential fit for $a_0 \gg 1$, given by (2.5.6).

This is plotted in fig. 11. A good approximation of $n_{\max}$ for $a_0 \gg 1$ is given by

$$n_{\max} \simeq 30\, a_0^{2.53}. \tag{2.5.6}$$

While comparable, this is larger than the limit $n_{\max} \sim \mathcal{O}(a_0^3)$ given by Seipt [73, p. 134]. However, that calculation sought convergence of the scattering rate rather than the power; while each extra harmonic contributes a smaller number of photons, the wider range of possible energies means that the partial power decreases more slowly and so our sum must necessarily be taken to higher n.

We can see that an emission event taking place in a background field with $a_0 \simeq 10$ and $\omega = 1$ eV could draw up to 10 keV of energy from that field. As an electron with $\mathcal{E} \simeq 100$ MeV will produce photons with $\omega' \simeq 10$ MeV, it is an acceptable approximation to take the recoil of the electron to be exactly the photon momentum. It is more concerning to note that for very large a_0, calculating the NLCS photon spectrum requires including a prohibitively large number of non-linear orders. The resolution to this difficulty will be discussed in section 2.7.

2.6 IN EXPERIMENT

We could examine NLCS experimentally in the collision of an intense laser pulse ($a_0 \simeq 1$) with an energetic electron beam. This was most famously achieved in SLAC Experiment E144 [74, 75, 76], where 46.6 GeV electrons colliding with a TW laser pulse (intensity $\sim 10^{18}$ Wcm^{-2}, $a_0 \simeq 0.5$) produced energetic gamma rays by NLCS, some of which decayed to electron-positron pairs in the intense field of the laser. The results, that non-linear orders up to 5 were observed in the scattering [74] and pair production [75], were consistent with theoretical predictions.

We would like to perform an experiment of this type in an all-optical setup, using two laser pulses: one to accelerate an electron beam and the other to act as the intense target. The difficulty here lies in aligning the beams sufficiently well that the electron beam collides with the target pulse. Led by C. D. Murphy, an experiment was performed at the Astra-Gemini facility, STFC Rutherford Appleton Laboratory. The geometry was inspired by Ta Phuoc et al. [77], in which a single laser pulse was used as accelerator and target, thus avoiding the alignment difficulties of a two-beam setup. The experimental design is illustrated in fig. 12.

2.6.1 *Experimental procedure*

The laser pulse was estimated to have a duration $\tau = 40$ fs, wavelength $\lambda = 0.8$ μm and waist size $w_0 = 25$ μm, corresponding to a photon energy of $\omega = 1.55$ eV. Colliding this with the wakefield-accelerated electron beam was achieved by reflecting the laser from a foil; as the electrons follow the laser pulse at a distance of 10s of μm along its axis of propagation, overlap of the beams is much more easily achieved. This

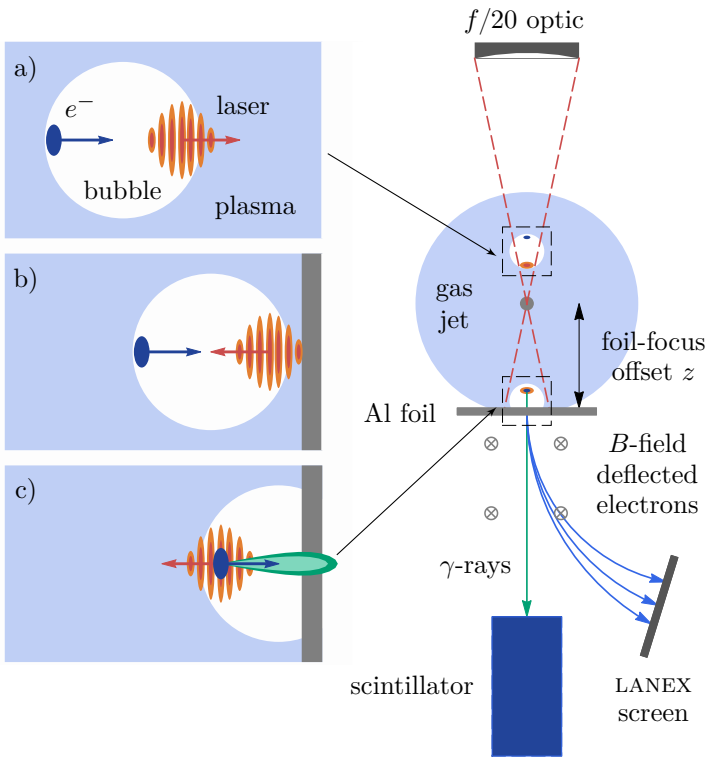

Figure 12: a) A 40 fs laser pulse is focused with an $f/20$ optic onto a He supersonic gas jet, reaching $a_0 \sim 1$ and driving a wakefield that accelerates an electron bunch to 100s of MeV. b) The laser pulse, moving at the head of the bubble structure, reflects off a plasma mirror formed at the surface of the Al foil target. c) The electron beam collides with the laser pulse and emits γ-rays in the forward direction, which are detected in a CsI scintillator block. In the absence of the foil, the electron beam is deflected magnetic field onto a LANEX screen to determine its energy spectrum. (Adapted from Ta Phuoc et al. [77].)

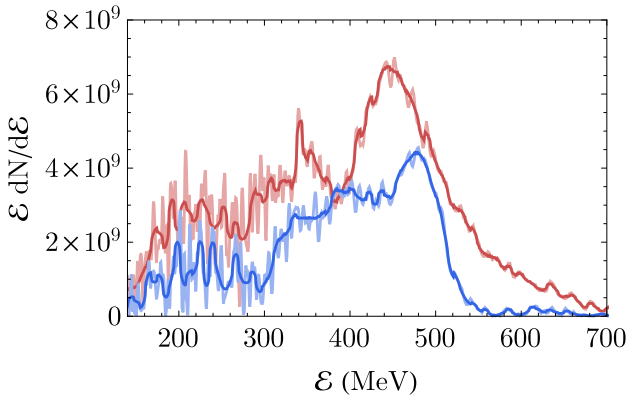

Figure 13: Energy spectra of the wakefield-accelerated electron beams generated by experimental shots (light red) 14 and (light blue) 27. Darker lines are the smoothed spectra used as simulation input. (Provided by Murphy [23].)

comes at the expense of laser intensity: wakefield acceleration requires a laser pulse in long focus [78] and the spot size of a Gaussian beam is inversely proportional to its divergence. The a_0 of the laser pulse at the collision point was varied from shot to shot by adjusting the foil-focus offset z, exploiting the divergence of the laser beam to perform an intensity scan in the range $0.5 \lesssim a_0 \lesssim 2$. The non-linear nature of the scattering process then manifests itself in the dependence of the gamma ray yield on z, a proxy for a_0.

The diagnostics available were a Thomson spectrometer and scintillator stack, measuring the electron beam and gamma ray energies respectively. While the former gives an energy spectrum for the electron beam (in the range $[127, 800]$ MeV, the limits arising from the size of the detector), the latter does not do so directly for the gamma rays. This is because the energy loss per unit length in a scintillator stack, being stochastic, is proportional to the energy in the beam. Thus two 50 MeV photons cannot necessarily be distinguished from a single 100 MeV photon.

NLCS must be identified indirectly. The electron beam's energy spectrum can be measured from shot to shot, as shown in fig. 13; smoothed spectra are used as input to obtain a simulated yield of Compton scat-

tered gamma rays. That yield can be used as input in a GEANT4 [79, 80] simulation of the experimental apparatus, calculating the expected scintillator signal. GEANT4 was also used to calculate the gamma ray background arising from bremsstrahlung of the electron beam in the foil and the wall of the gas cell. Analysis of the experimental results is ongoing, but here we can discuss the NLCS simulations I have performed.

2.6.2 *Simulated gamma ray yields*

I have developed a Monte-Carlo code to simulate gamma ray production from energetic electrons colliding with an intense laser pulse in the NLCS regime. It accepts as input experimentally measured electron spectra, using pseudorandom sampling to initialise the computational electron beam. The algorithm neglects the ponderomotive deflection of the electron beam by the laser and the defocusing effect of its own space-charge field, assuming that each electron may be treated independently and that they propagate ballistically through the laser pulse close to the speed of light.

For the experimental parameters in question, where the electrons have Lorentz factors $\gamma > 100$ and the laser pulse has strength parameter $a_0 \sim 1$, we have $\gamma \gg a_0$; the rigid-beam approximation is then valid as the transverse momentum gained from the laser $\sim a_0 m$ is small compared to the longitudinal momentum. This does not mean the fast quiver motion of the electrons has been neglected: recall from section 2.2 that this oscillation is implicitly included by using the quasi-momentum in the scattering rate.

We can neglect the effect of the space-charge field as well. If the electron bunch has a radially symmetric charge density and its length is much larger than its radius, then its electric and magnetic fields are,

respectively, purely radial and purely azimuthal. From Gauss's and Ampere's laws in cylindrical coordinates

$$\frac{1}{r}\frac{\partial(rE_r)}{\partial r} = \rho(r) \qquad \frac{1}{r}\frac{\partial(rB_\phi)}{\partial r} = \beta\rho(r) \tag{2.6.1}$$

we have

$$E_r = \frac{B_\phi}{\beta} = \frac{1}{r}\int_0^r r'\rho(r')\,\mathrm{d}r' \tag{2.6.2}$$

where β is the velocity of the beam. These space-charge fields exert a defocusing force

$$F_{\mathrm{sc}} = q(E_r - \beta B_\phi) = \frac{e|E_r|}{\gamma^2}. \tag{2.6.3}$$

Wakefield-accelerated electron beams typically have charge 100 pC and transverse (longitudinal) dimension 5 (20) μm [78], so $F_{\mathrm{sc}} \simeq 10^{-8}\gamma^{-2}$ MeV^2 which is much smaller than the power radiated in NLCS. We may therefore take the electron trajectory, initially antiparallel to the laser propagation axis, to be one-dimensional and its momentum as constant between emission events.

The algorithm is implemented as follows, following Duclous et al. [17]: each electron is pseudorandomly assigned a 'final' optical depth τ_{f} against emission. As it propagates through the laser pulse, its differential optical depth $\mathrm{d}\tau/\mathrm{d}t$ is integrated according to

$$\frac{\mathrm{d}\tau}{\mathrm{d}t} = \sum_{n=1}^{n_{\max}}\int_0^1 \frac{\mathrm{d}W_n}{\mathrm{d}x}\,\mathrm{d}x \tag{2.6.4}$$

where $\mathrm{d}W_n/\mathrm{d}x$ is given by (2.4.2). The largest non-linear order included $n_{\max}$ is determined by the a_0 at each timestep. Emission occurs when $\tau = \tau_{\mathrm{f}}$: the energy of the scattered photon (as a fraction of the electron energy) is determined by solving

$$\sum_{n=1}^{n_{\max}}\int_0^x \frac{\mathrm{d}W_n}{\mathrm{d}x}\,\mathrm{d}x = R\sum_{n=1}^{n_{\max}}\int_0^1 \frac{\mathrm{d}W_n}{\mathrm{d}x}\,\mathrm{d}x \tag{2.6.5}$$

for

$$x \in \left[0, \frac{n_{\max} u}{1 + n_{\max} u}\right] \tag{2.6.6}$$

where R is a pseudorandom number. The electron's final optical depth is reassigned, and its momentum reduced by that of the emitted photon. This neglects the energy absorbed from the background field; however, as can be seen from fig. 11, this is always $\lesssim 200$ eV and so the error in doing so is negligible. The approximation that the photon is emitted exactly parallel to the electron momentum is valid if the electron has $\gamma \gg 1$.

(2.6.4) employs a NLCS rate that was derived considering a plane EM wave of infinite extent: describing a real laser pulse as such is clearly something of an idealisation, as to reach high intensities, laser energy needs to be focused spatially and temporally. However, provided that the electron beam is radially smaller than the laser focus, we can neglect the transverse variation in laser intensity. The effect of the temporal profile of the laser pulse is of more importance.

As discussed by Heinzl et al. [81], this gives rise to subharmonic structure in the photon spectrum. For each harmonic n, there are nonlinear Compton edges for each $a_0 \in [0, a_{0,\text{peak}}]$; as the effective length over which the scattering takes place is of order the laser wavelength (see section 2.7), there is interference between radiation that is emitted at different times, creating sub-peaks that range in energy from the Compton edge for $a_0 = a_{0,\text{peak}}$ to that for $a_0 = 0$. This structure is illustrated in fig. 5 of [81]; they find that the number of sub-peaks for the first harmonic $N \simeq 0.24 a_0^2 (T/\text{fs})$ where T is the duration of the laser pulse.

We neglect this interference, effectively averaging over the subharmonic structure. This is an acceptable approximation as the laser pulse in this experiment is a long pulse ($T \sim 40$ fs) and weakly focused. There will be a large number of sub-peaks, but these will be smeared out as

the electron beam is not mono-energetic (see fig. 13) and scattering can take place to $n > 1$. Were the target laser pulse very short, with duration of a few cycles only, it would be necessary to follow the method of [82, 67], which takes into account the temporal profile when deriving the NLCS matrix element.

We assume that all electrons experience the same $a_0(t)$ along their trajectories, given by

$$a_0(t) = a_0 \exp\left(-\frac{t^2}{\tau^2}\right) \tag{2.6.7}$$

where $0.5 < a_0 < 2$ and $\tau = 40$ fs. The electron's initial energies are sampled from a smoothed distribution based on the experimental spectra shown in fig. 13. Figure 14 gives the simulated gamma ray spectra arising from both non-linear and linear Compton scattering of beams 14 and 27 for various laser a_0.

As a_0 increases the difference between non-linear and linear Compton scattering becomes more pronounced. While the shape of the linear spectrum does not change with a_0, its height does increase, scaling as $N \sim a_0^2$ according to (2.4.10). The structure that can be seen arises from structure in the electron beam's initial energy spectrum; for shot 14, the peaks at 200, 340 and 450 MeV give rise to peaks in the photon spectrum at 0.95, 2.7 and 4.6 MeV, estimating the upshift to be $4\gamma^2$ and taking the laser photon energy to be $\omega = 1.55$ eV. The largest photon energy is approximately 10 MeV for shot 14 and 7 MeV for shot 27 across the range of a_0.

The shape of the non-linear spectrum does however change with increasing a_0. At $a_0 = 0.5$ it is similar to that from linear Compton scattering, with most of the scattering taking place at first order ($n = 1$), but the peak energies have been reduced by 10% because of the mass shift. The contribution from higher harmonics washes out the struc-

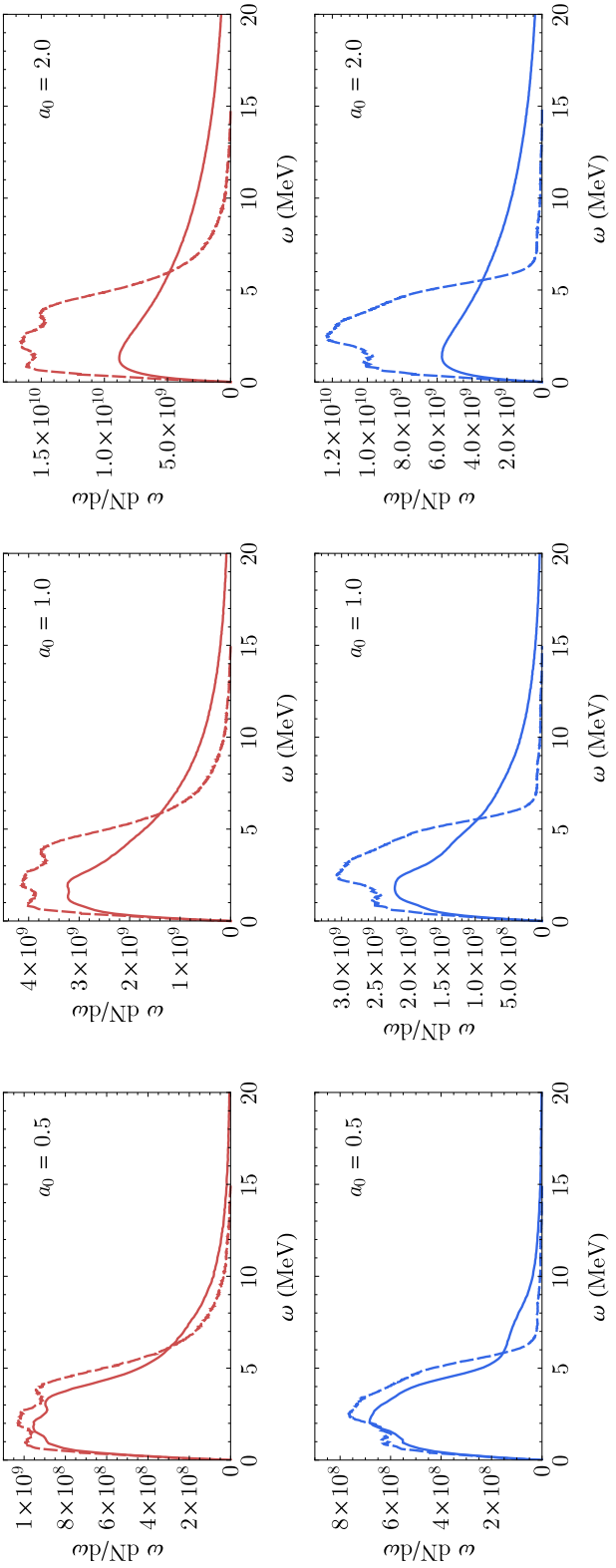

Figure 14: Simulated gamma ray spectra from (solid) non-linear Compton scattering and (dashed) linear Compton scattering of electron beams (red) 14 and (blue) 27 and laser $a_0 = 0.5, 1, 2$.

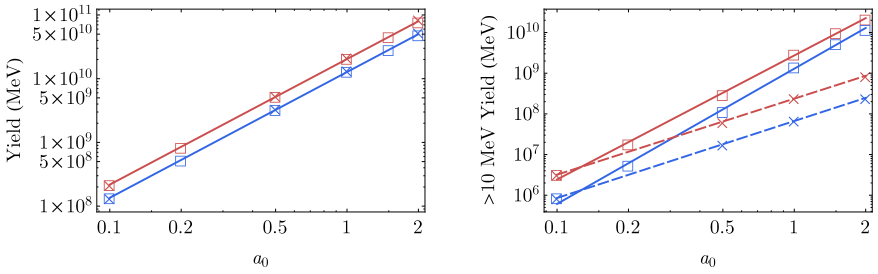

Figure 15: (left) The simulated yields of gamma rays of all energies and (right) those with $\omega > 10$ MeV from shots (red) 14 and (blue) 27. (solid) Power law fit to (squares) NLCS spectra; (dashed) power law fit to (crosses) linear Compton spectra.

ture evident in the linear spectrum for shot 14 as a_0 increases, and a high-energy tail develops up to a maximum of 20 MeV.

Let us consider whether the total yield provides evidence of non-linearity. Figure 15 shows how the integrals of the spectra in fig. 14 scale with increasing a_0. The total yield does not allow us to distinguish between linear and non-linear Compton scattering; both yields scale quadratically with a_0, as discussed in section 2.5. However, as NLCS manifests itself in the hardening of the photon spectrum, if we consider the non-linear yield of photons with $\omega > 10$ MeV, we find that it increases as a_0^3 rather than a_0^2.

Measuring the photon spectrum directly would provide strong evidence of non-linear Compton scattering; this has been accomplished by Sarri et al. [83], who demonstrated production of gamma rays with energies up to 18 MeV from non-linear scattering of 400 MeV electrons in a laser pulse with $a_0 \simeq 2$. Those experimental parameters are similar to those studied here and the gamma ray spectra they show are qualitatively similar to fig. 14.

2.7 FORMATION LENGTH AND THE HIGH-INTENSITY LIMIT

In section 2.2 we discussed how employing the conservation of quasi-momentum to determine the scattering kinematics implicitly assumed

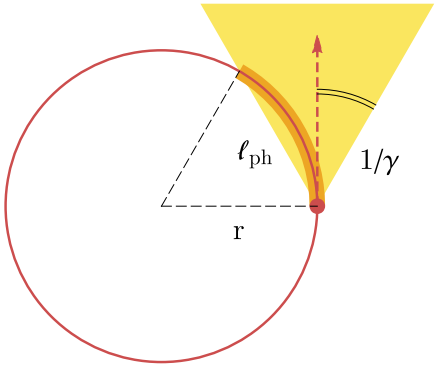

Figure 16: The photon formation length $\ell_{\rm ph}$, as seen in the average rest frame of an electron in a circularly polarised EM wave.

that the emission process occurred throughout a region with size comparable to the laser wavelength. That can be made more precise following Ritus [9]; for simplicity we consider only circular polarisation [9, sec. 18] (the result for linear polarisation is the same [9, sec. 8]).

The differential probability rate (2.4.1) depends upon Bessel functions, which arise from the Fourier expansion of the Volkov states (2.2.4). In the integral representation

$$J_n(z) = \frac{1}{2\pi}\int_{-\pi}^{\pi} \exp\left[i\left(z\sin\theta - n\theta\right)\right] \mathrm{d}\theta \tag{2.7.1}$$

where z is as given in (2.4.3) and θ is related to the wave phase ϕ and the azimuthal angle ϕ_0 at which emission occurs by $\theta = \phi - \phi_0$.

If $a_0 \ll 1$, $z < 1$ and $n \sim 1$; the integrand in (2.7.1) is slowly oscillating and the entire phase interval $[-\pi, \pi]$ contributes to the emission. If $a_0 \gg 1$, by contrast, $z \sim n \sim a_0^3 \gg 1$. (2.7.1) can be expanded in this limit using the saddle-point method. It is found that the dominant contribution to the integral arises from a phase region around $\phi = \phi_0$ that has width $\Delta\phi \simeq 1/a_0$. The length over which the photon is formed is then

$$\ell_{\rm ph} \simeq \frac{\lambda}{a_0}. \tag{2.7.2}$$

We can use the results of section 1.2.2 to justify this classically. An electron in a circularly polarised plane wave performs circular orbits at the laser frequency ω in the plane perpendicular to the laser wavevector k; in its average rest frame, these orbits have radius

$$r = \frac{a_0}{\omega\sqrt{1+a_0^2}} \tag{2.7.3}$$

and the electron Lorentz factor

$$\gamma = \sqrt{1+a_0^2}. \tag{2.7.4}$$

Radiation is strongly beamed in the direction of the electron momentum into a cone of opening angle $\sim 1/\gamma$. We can think of the photon formation length as the distance over which the electron is swept out of this cone, after which interval it has decoupled from the radiation [84]. Figure 16 shows the geometry of this situation; the length pictured satisfies

$$\ell_{\text{ph}} = \frac{\lambda a_0}{\pi(1+a_0^2)} \simeq \frac{\lambda}{a_0} \tag{2.7.5}$$

which is consistent with (2.7.2), the result from strong-field QED.

In section 2.5 we saw that as a_0 becomes large, the number of nonlinear orders that must be included (such that the radiated power converges) itself becomes large, making calculation of the NLCS rate difficult. However, we have now seen that for $a_0 \gg 1$, the region over which the emission process occurs becomes vanishingly small. The emitted photon cannot therefore carry information about the field structure: it only 'sees' the electron trajectory over a region in which the external fields are effectively constant. In the limit that $\lambda/a_0 \to 0$, the rate (2.4.1) can be replaced by the scattering rate calculated in a *constant crossed field*, i.e. $|\mathbf{E}| = c\,|\mathbf{B}|$ and $\mathbf{E} \perp \mathbf{B}$ [9, 85]. This is called the *quasistatic approximation* and greatly simplifies the calculation of the transition rate, allowing our analysis of NLCS to be extended easily to

$a_0 > 10$. Furthermore, it becomes possible to model QED processes in strong fields that have arbitrary shape, by treating them as 'stacked slices' of constant field. We will explore these consideration in the next chapter.

2.8 CONCLUDING REMARKS

It appears that QED naturally incorporates radiation reaction in a way that classical electromagnetism cannot, as the electromagnetic field is formed of quanta that carry both energy and momentum. At each NLCS event, the conservation of momentum determines the recoil experienced by the radiating electron. However, as this recoil is proportional to $\hbar$, it is a quantum-mechanical phenomenon; in the classical limit $\hbar \to 0$ we recover Thomson scattering, which is elastic, rather than the radiation reaction force identified in section 1.3 [10, sec. 6b].

The remedy is to identify quantum radiation reaction with the overall recoil caused by multiple, incoherent emissions [86]: an electron embedded in an intense laser field ($a_0 \gg 1$) emits $N \sim \alpha a_0$ photons per laser period, each carrying energy $\omega' \simeq u\mathcal{E}$; while both N and ω' are quantum-mechanical in origin ($\alpha \sim 1/\hbar$ and $u \sim \hbar$), their product, the total energy loss, does not contain $\hbar$ and so has a classical analogue. The detail of that consistency will be discussed in section 3.3.3.

While strong-field QED can be successfully used to describe the radiation produced by an energetic electron in an intense laser pulse, it is clear this method has shortcomings. These include the necessity of including prohibitively many NLCS orders as the intensity increases and, more seriously, the difficulty of extending the analysis to EM fields with arbitrary spatial and temporal shape.

However, the results of section 2.7 indicate that a dramatic simplification occurs if the fields are very strong indeed. We have seen that

the length over which QED processes occur becomes small compared to the length over which the field varies for $a_0 \gg 1$. This large separation of scales suggests a semi-classical treatment, where between pointlike, instantaneous QED events, the electron may be treated as propagating classically [20]. This method of incorporating QED processes in the simulation of laser-plasmas will be the subject of the next chapter.

3

QED PROCESSES FOR $a_0 \gg 1$

3.1 INTRODUCTION

Having considered both classical radiation reaction and non-linear Compton scattering, it is evident that there is new physics that must be incorporated into conventional models of laser-plasmas as the driving intensity exceeds $10^{22}\ \mathrm{W\,cm^{-2}}$. The question is: how? We have seen that classical radiation reaction poses awkward questions about the structure of the electron, and that calculating analytical matrix elements for non-linear QED processes is impossible outside configurations of high symmetry.

The way forward was indicated in section 2.7: as the laser intensity increases, the formation length for QED processes becomes much smaller than the typical length of the external field structure. There arises a large separation of scales between the electron's interaction with this external field and the radiation field. We will find that it is possible to treat the former classically, as in standard plasma physics, and the latter perturbatively, through the methods of strong-field QED. In situations where the electron couples strongly to both, a new regime of plasma physics is reached which we term a *QED-plasma*. How one studies these plasmas will be the subject of this chapter.

We now return to SI units, though per-particle energies will be measured in MeV and intensities in $\mathrm{W\,cm^{-2}}$ rather than their SI equivalents.

3.2 THE WEAK-FIELD AND QUASISTATIC APPROXIMATIONS

Let us consider the probability rates for photon emission by an electron and pair production by a photon in a uniform, static electromagnetic field characterised by field tensor $F^{\mu\nu}$. The electron and photon have four-momenta p^μ and $\hbar k^\mu$ respectively. For the probabilities to be Lorentz invariant, the transition rates can be functions of only these four invariants [84, 9]

$$\begin{aligned} \eta &= \frac{\sqrt{-(F_{\mu\nu}p^\nu)^2}}{mcE_{\text{Sch}}} & \chi &= \frac{\hbar\sqrt{-(F_{\mu\nu}k^\nu)^2}}{2mcE_{\text{Sch}}} \\ f &= -\frac{F_{\mu\nu}F^{\mu\nu}}{2E_{\text{Sch}}^2} & g &= -\frac{F^*_{\mu\nu}F^{\mu\nu}}{4E_{\text{Sch}}^2} \end{aligned} \tag{3.2.1}$$

where $E_{\text{Sch}} = m^2c^3/e\hbar$ is the critical field of QED. In terms of the electron Lorentz factor γ and velocity $\mathbf{v}$, the photon frequency ω and wavevector $\mathbf{k}$, and the electric and magnetic field strengths $\mathbf{E}$ and $\mathbf{B}$, where $\mathbf{E}$ has component $\mathbf{E}_\perp$ perpendicular to $\mathbf{v}$ (or $\mathbf{k}$)

$$\eta = \frac{\gamma\sqrt{\left(\mathbf{E}+\mathbf{v}\times\mathbf{B}\right)^2 - \left(\mathbf{E}\cdot\mathbf{v}/c\right)^2}}{E_{\text{Sch}}} \simeq \frac{\gamma\left|\mathbf{E}_\perp + \mathbf{v}\times\mathbf{B}\right|}{E_{\text{Sch}}} \tag{3.2.2}$$

$$\chi = \frac{\hbar\left|\omega\mathbf{E}_\perp + c^2\mathbf{k}\times\mathbf{B}\right|}{2mc^2E_{\text{Sch}}} \tag{3.2.3}$$

$$f = \frac{\mathbf{E}^2 - c^2\mathbf{B}^2}{E_{\text{Sch}}^2} \tag{3.2.4}$$

$$g = \frac{c\mathbf{B}\cdot\mathbf{E}}{E_{\text{Sch}}^2} \tag{3.2.5}$$

where the asymptotic equality in (3.2.2) holds for ultrarelativistic electrons ($\gamma \gg 1$).

By setting $\gamma = 1$ and $\mathbf{v} = 0$ in (3.2.2), we can see that if $\eta = 1$, the electron observes in its rest frame an electric field of critical strength. We expect strong-field QED effects to become important for $\eta = 1$; the implication here is that although we cannot yet create a field comparable to E_{Sch} in the lab frame, it is possible to probe one

by using ultrarelativistic particles to 'boost' the lab field to critical strength. The other three invariants can be understood in these terms. While a photon has no rest frame, we can define for it a quantum parameter χ by analogy with η, using the photon four-momentum $\hbar k^\mu$ rather than p^μ. f, g are the two invariant measures of field strength: a static electric field that could spontaneously produce electron-positron pairs from the vacuum [52] would have $f \geqslant 1, g = 0$.

If we have both $f, g \ll 1$ and $\eta^2 \gg \max(f, g)$, then we can make the *weak-field approximation*, which is that we may neglect the dependence of the transition rates on f and g; setting $f = g = 0$, a general rate $W(\eta, \chi, f, g) = W(\eta, \chi, 0, 0)$ becomes a function of η and χ only [84, 17]. The *quasistatic approximation* is that for an electron or photon moving in an arbitrary EM field, the probability rate for a QED process may be calculated in an equivalent system which has the same η or χ, but in which the EM field is both uniform and static [84, 17].

The two most commonly used equivalent systems are the *constant crossed field* (e.g. [87, 88, 9]) and the *static magnetic field* (e.g. [89, 90, 60, 91]). The former is defined by $|\mathbf{E}| = c\,|\mathbf{B}|$ and $\mathbf{E} \perp \mathbf{B}$, i.e. a monochromatic plane wave in the low-frequency limit. In the static magnetic field approach $\mathbf{E} = 0$, so to satisfy the weak-field and quasistatic approximations we must have $|\mathbf{B}| \ll E_{\text{Sch}}/c$ and $\gamma \gg 1$.

The weak-field approximation is likely to be valid in all laser-plasma experiments for the foreseeable future as $E_{\text{Sch}} = 1.3 \times 10^{18}$ Vm^{-1} (or 4.4×10^9 T) is equivalent to an intensity of 2×10^{29} Wcm^{-2}, seven orders of magnitude greater than the current intensity frontier [1, 54]. For the quasistatic approximation to be valid, we require that the formation length of the given process be much shorter than the length scale over which the field varies. As discussed in section 2.7, in an in-

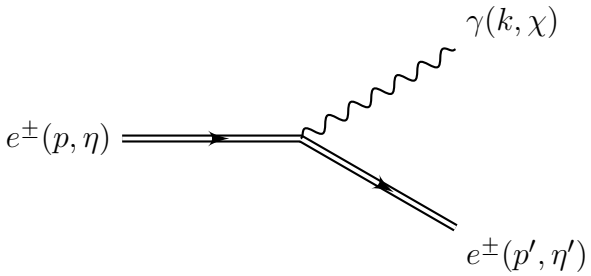

Figure 17: Feynman diagram for synchrotron photon emission. Double lines are 'dressed' electron states that account exactly (to all orders in a_0) for the effect of the classical external field.

tense laser field, the photon formation length is smaller than the laser wavelength by a factor of a_0, so the quasistatic approximation becomes

$$a_0 = \left[\frac{I(\lambda/\mu\mathrm{m})^2}{1.37\times10^{18}\ \mathrm{Wcm}^{-2}}\right]^{1/2} \gg 1. \tag{3.2.6}$$

For a 1 μm laser, we can take the intensity requirement to be $I > 10^{21}$ Wcm^{-2}.

With both these approximations satisfied, we can continue by discussing the QED processes we will be studying in laser-plasma interactions: at $\mathcal{O}(\alpha)$, synchrotron photon emission and Breit-Wheeler pair production; and at $\mathcal{O}(\alpha^2)$, trident pair production.

3.3 SYNCHROTRON PHOTON EMISSION

This is the emission of a photon by an electron (or positron) moving in a strong electromagnetic field, as shown in fig. 17. It is frequently referred to as *non-linear Compton scattering* even if the equivalent system is a constant crossed field, which term we reserve for the process that occurs at $a_0 \gtrsim 1$ in a plane EM wave; in the static magnetic field approach, it can be called *magnetic bremsstrahlung* [91], *curvature radiation* [16] or *quantum synchrotron emission* [11]. We adopt the last of these. However, provided η is the same, the choice of system will not affect the final result.

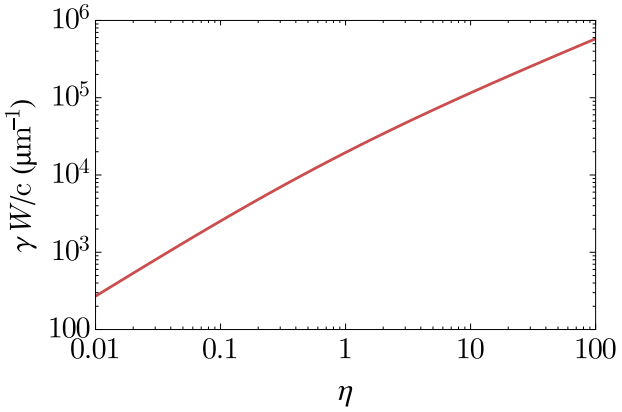

Figure 18: The instantaneous rate of synchrotron photon emission W, as given by (3.3.2), for an ultrarelativistic electron with Lorentz factor γ and quantum parameter η.

Following Erber [60] and Baier et al. [91], the differential probability rate for an electron with Lorentz factor γ and quantum parameter η to emit a photon with parameter χ is

$$\frac{\mathrm{d}W_\gamma}{\mathrm{d}\chi} = \frac{\sqrt{3}\alpha}{2\pi\tau_\mathrm{c}}\frac{\eta}{\gamma}\frac{F(\eta,\chi)}{\chi} \tag{3.3.1}$$

where $\tau_\mathrm{c} = \hbar/mc^2 = 1.288\times10^{-6}$ fs is the Compton time and $F(\eta,\chi)$ is the quantum synchrotron function, given in section 3.3.1. This rate describes *unpolarised* emission, i.e. the matrix element has been averaged over the initial spin state of the electron and summed over the final spin states of the electron and photon.

Integrating (3.3.1) over all photon energies $0 \leqslant \chi \leqslant \eta/2$ gives the total rate of emission

$$W_\gamma = \frac{\sqrt{3}\alpha}{2\pi\tau_\mathrm{c}}\frac{\eta}{\gamma}h(\eta) \tag{3.3.2}$$

where [91]

$$h(\eta) = \begin{cases} \frac{5\pi}{3}\left(1-\frac{8\eta}{5\sqrt{3}}+\frac{7\eta^2}{2}\right) & \eta \ll 1, \\ 5.298\eta^{-1/3} & \eta \gg 1. \end{cases} \tag{3.3.3}$$

This is plotted in fig. 18. As a rule of thumb, the number of photons emitted per laser period by an electron propagating at an angle θ to the laser optical axis is $\sim 15(1-\cos\theta)\alpha a_0$.

3.3.1 *The quantum synchrotron function*

The quantum synchrotron function determines the emissivity of the electron as well as the shape of the radiated photon spectrum. It is given by

$$F(\eta,\chi) = \frac{4\chi}{3\eta^2}\left[\left(1-\frac{2\chi}{\eta}+\frac{1}{1-2\chi/\eta}\right)K_{2/3}(\delta) - \int_\delta^\infty K_{1/3}(t)\,\mathrm{d}t\right] \quad (3.3.4)$$

where

$$\delta = \frac{4\chi}{3\eta^2}\left(1-\frac{2\chi}{\eta}\right)^{-1}. \quad (3.3.5)$$

$F(\eta,\chi)$ is non-zero only for $0<\chi<\eta/2$; from the definitions of η (3.2.2) and χ (3.2.3) it can be seen that the upper bound on the energy of the scattered photon is that of the electron.

For small χ, the quantum synchrotron function (3.3.4) has limiting behaviour

$$F(\eta,\chi) \simeq \left(\frac{16}{3}\right)^{1/3}\Gamma\left(\frac{2}{3}\right)\eta^{-2/3}\chi^{1/3} \quad (3.3.6)$$

where the coefficient $(16/3)^{1/3}\Gamma(2/3)\simeq 2.366$. This means that $F(\eta,\chi)/\chi$, and so the differential rate of photon emission (3.3.1), diverge as $\chi^{-2/3}$ for $\chi\to 0$. The total number of photons, however, does not diverge. Neither does the normalised energy emitted to photons with frequency between χ and $\chi+\mathrm{d}\chi$ during interval $\mathrm{d}t$, $\chi\frac{\mathrm{d}W}{\mathrm{d}\chi}\mathrm{d}t\mathrm{d}\chi$, which is zero for $\chi=0$.

In a classical framework, one should strictly consider the differential intensity of emission rather than the differential rate, as the concept of a 'number of photons' is purely quantum-mechanical. Nevertheless we can define a classical version of (3.3.1) provided that the concomitant

radiated power is consistent with the classical prediction [92]. The result is that $F(\eta, \chi)$ is replaced by its classical counterpart [93, sec. V-B]

$$F_{\mathrm{cl}}(\eta, \chi) = \delta_{\mathrm{cl}} \left[2K_{2/3}(\delta_{\mathrm{cl}}) - \int_{\delta_{\mathrm{cl}}}^{\infty} K_{1/3}(t)\, \mathrm{d}t \right] \tag{3.3.7}$$

where $\delta_{\mathrm{cl}} = 4\chi/3\eta^2$. This is equivalent to the formulation $F_{\mathrm{cl}}(\eta, \chi) = \delta_{\mathrm{cl}} \int_{\delta_{\mathrm{cl}}}^{\infty} K_{5/3}(t)\, \mathrm{d}t$ given in Kirk et al. [84] and is maximised for $\chi = 0.214\eta^2$, or $\hbar\omega = 0.429\eta\gamma mc^2$ [16].

This differs from the quantum synchrotron function (3.3.4) in that it neglects both the effect of recoil and the spin contribution. The first of these is encoded in δ: according to Schwinger [90] and Lindhard [94], the effect of recoil can be included in the classical rate by substituting for the radiated frequency $\omega \to \omega\mathcal{E}/(\mathcal{E} - \hbar\omega)$, which modifies δ_{cl} to give δ (3.3.5). The spin contribution is given by the bracketed factor multiplying $K_{2/3}(\delta)$ in (3.3.1) [93, sec. V-E]; by identifying $2\chi/\eta = \hbar\omega/\mathcal{E}$ we can see that in classical limit this factor $\to 2$. This approximation is acceptable if $\chi \ll \eta/2$, i.e. the photon energy is much smaller than that of the electron. However, as the spin factor becomes very large for $\chi \simeq \eta/2$, it dramatically enhances the probability of photons with energy comparable to that of the electron.

The quantum synchrotron function and its classical limit are plotted in fig. 19. We can see that the classical approximation always overestimates the emissivity of the electron; indeed, for $\eta = 2$, it predicts the emission of photons with energies greater than that of the electron. The spin contribution to the rate, which is concentrated at the high energy tail of the spectrum, only becomes significant for $\eta \gtrsim 1$.

An intuitive physical explanation for this is given by Kirsebom et al. [95]. Consider the equivalent system of an ultrarelativistic electron in a static magnetic field. In the electron rest frame, there is an energy difference between the spin-up and spin-down states of the electron of $\Delta\mathcal{E} = 2\mu B_{\mathrm{rf}}$, where the electron magnetic moment $\mu = e\hbar/2m$. The rest

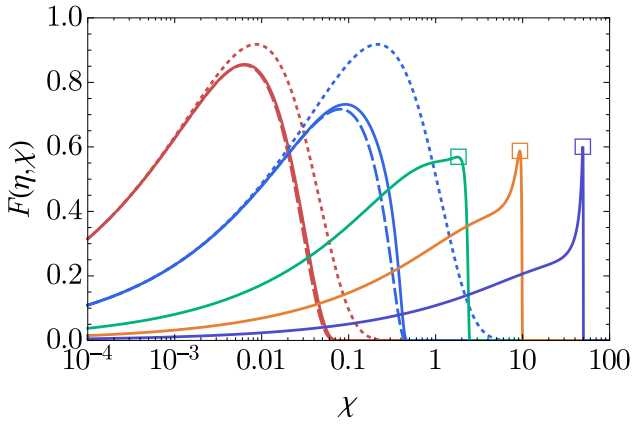

Figure 19: (solid) The quantum synchrotron function (3.3.4), (dotted) the classical synchrotron function (3.3.7) and (dashed) a semi-quantum synchrotron function that includes recoil but not the spin contribution, for electrons with η = (red) 0.2, (blue) 1, (green) 5, (orange) 20 and (purple) 100. (boxes) The maxima of $F(\eta,\chi)$ for $\chi \gg 1$ are approximately $\eta/2 - 2/3$.

frame magnetic field $B_{\rm rf} = \gamma B$, where γ and B are the electron Lorentz factor and magnetic field in the equivalent system. A photon emitted in a spin-flip transition has energy $\hbar\omega \simeq \gamma\Delta\mathcal{E}$, transforming back from the rest frame; identifying $\eta = \gamma(cB/E_{\rm Sch})$ and $\chi = (\hbar\omega/2mc^2)(cB/E_{\rm Sch})$, its quantum parameter $\chi \simeq \eta^2/2$. The quasistatic approximation means that this relation is valid for all electrons that have the same η, so we conclude that for spin-flip transitions to produce photons with energies comparable to that of the electron, we must have $\eta \gtrsim 1$.

Figure 19 also shows that as η grows larger than 1, the photon spectrum increasingly 'piles up' against the edge $\chi = \eta/2$. Let us estimate the location of the maximum of $F(\eta,\chi)$ in the limit that $\eta \to \infty$. Near the edge of the spectrum, $\epsilon = 1 - 2\chi/\eta$ is small and $\delta \simeq 2/(3\epsilon\eta)$. Estimating $F(\eta,\chi) \simeq 4K_{2/3}(\delta)/(6\epsilon\eta)$ and $K_{2/3}(\delta) \simeq \sqrt{\pi/(2\delta)}\exp(-\delta)$, we find that the quantum synchrotron function peaks at $\chi \simeq \eta/2 - 2/3$, which is a reasonable estimate of the true maximum for $\eta > 5$. We conclude that in that regime, an energetic electron is overwhelmingly likely to radiate almost all its energy in a single gamma ray.

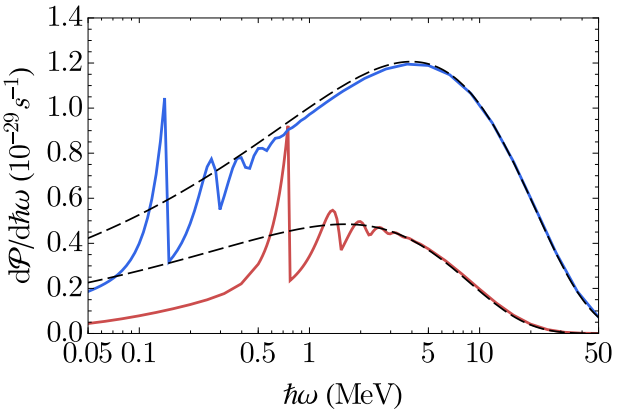

Figure 20: The differential power spectra for an electron with energy 500 MeV colliding with a plane wave with frequency 1 eV ($\lambda = 1.2\ \mu$m) and strength parameter a_0 = (red) 2 and (blue) 5, as calculated using the NLCS rate (2.4.1). (black, dashed) The synchrotron power (3.3.8) for the corresponding η.

3.3.2 *Radiated power and quantum suppression*

The differential power $\mathrm{d}\mathcal{P} = \omega\,\mathrm{d}W$ emitted in photons with parameter χ is

$$\frac{\mathrm{d}\mathcal{P}}{\mathrm{d}\chi} = \frac{2\mathcal{E}\chi}{\eta}\frac{\mathrm{d}W_\gamma}{\mathrm{d}\chi} = \frac{\sqrt{3}\alpha}{\pi}\frac{mc^2}{\tau_c}F(\eta,\chi). \tag{3.3.8}$$

This should be a good approximation to the power spectrum from non-linear Compton scattering when $a_0 \gg 1$, as the photon formation length becomes very short and so the plane EM wave can be treated quasistatically. Comparisons of the differential power for an electron with $\mathcal{E} = 500$ MeV colliding with a plane wave that has $a_0 = 2, 5$ are plotted in fig. 20. It is clear that while the synchrotron power is a good fit to the high energy tail of the spectrum, it smears out the low-energy harmonic structure. However, as the energy of first non-linear Compton edge falls with increasing a_0 (by (2.3.7)), the importance of this structure diminishes rapidly as the intensity increases. A thorough analysis of the discrepancy in the photon spectra that arises by treating their emission quasistatically is given by Harvey et al. [85]; they reach similar conclusions.

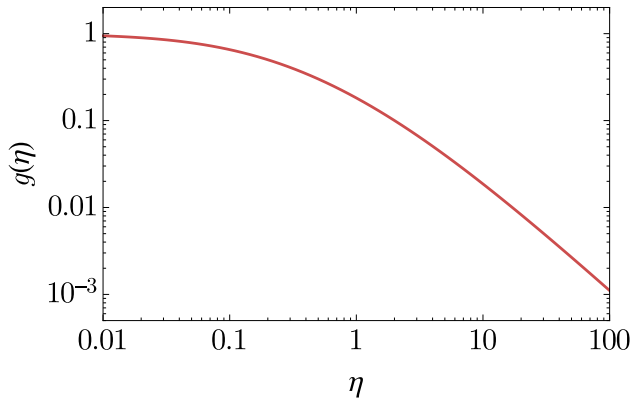

Figure 21: The quantum correction to the radiated power $g(\eta)$ as given by (3.3.10).

The total radiated power is obtained by integrating (3.3.8) over the range $0 \leqslant \chi \leqslant \eta/2$. We find

$$\mathcal{P} = \frac{2\alpha}{3}\frac{mc^2}{\tau_c}\eta^2 g(\eta) \tag{3.3.9}$$

where $g(\eta)$, the quantum-mechanical correction to the radiated intensity, is a monotonically decreasing function of η, defined [84]

$$g(\eta) = \frac{3\sqrt{3}}{2\pi\eta^2}\int_0^\infty F(\eta,\chi)\,\mathrm{d}\chi. \tag{3.3.10}$$

and plotted in fig. 21. For $\eta \ll 1$, $g(\eta) \simeq 1 - (55\sqrt{3}/16)\eta + 48\eta^2$ [90, 96], where the first term is the classical value obtained by replacing $F(\eta,\chi)$ with (3.3.7) [97], the second is a correction arising from the inclusion of recoil, and the third is the spin contribution [91]; for $\eta \gg 1$, $g(\eta) \simeq 0.5564\eta^{-4/3}$ [60]. An approximation which differs from the exact value by at most 2% is [91]

$$g(\eta) = \left[1 + 4.8(1+\eta)\ln(1+1.7\eta) + 2.44\eta^2\right]^{-2/3}. \tag{3.3.11}$$

For small η the radiated power (3.3.9) matches that predicted by the Larmor formula (1.2.5). However, as the electron energy (or field intensity) increase, the growth is strongly suppressed: at $\eta = 1$, for example,

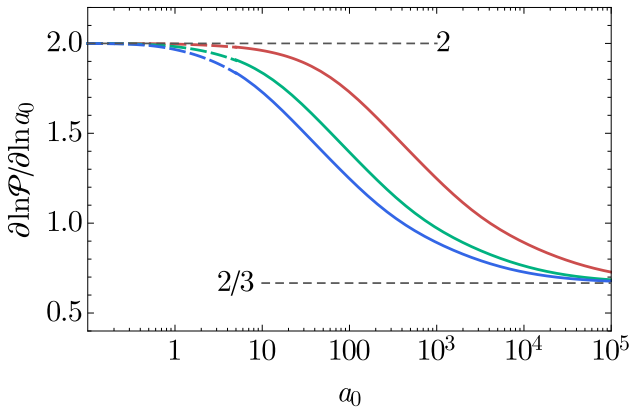

Figure 22: An extension of fig. 9, comparing the a_0 scalings of (solid) the quantum synchrotron power (3.3.9) and (dashed) the NLCS power (2.5.1) for an electron with energy (red) 100, (green) 500 and (blue) 1000 MeV colliding with a plane EM wave with frequency 1 eV ($\lambda = 1.2$ μm) and given strength parameter a_0; (grey, dashed) the limiting values of the scaling.

$g(\eta) \simeq 0.2$ and the classical prediction overestimates the power by a factor of 5. The physical origin of this reduction can be explained in terms of energy conservation. In classical electromagnetism, there is no restriction on the frequency of radiation that may be emitted and so the classical synchrotron function has an exponentially decaying tail to arbitrarily high frequency (as shown in fig. 19). This corresponds in a quantum-mechanical picture to the possibility of emitting a photon with energy greater than the electron. While negligible at low intensities, for $a_0 > 1$ it is necessary to introduce quantum corrections to cut off this high frequency tail, thereby reducing the exponent of the radiated power.

Finally, we are now in a position to extend the scaling law found in section 2.5: fig. 22 shows that as the intensity increases, the exponent of a_0 in the radiated power continues to fall, matching the NLCS prediction at $a_0 = 10$. We can confirm 2/3 to be the large a_0 value of the scaling by observing that $\mathcal{P} \propto \eta^{2/3}$ for $\eta \gg 1$ and that $\eta = 2\hbar\mathcal{E}\omega a_0/(mc^2)^2 \propto a_0$.

3.3.3 *Modifying the Landau-Lifshitz force*

In much the same way that the classical radiation reaction force was inferred from the Larmor formula in section 1.3, we can use (3.3.9) to derive a semi-classical equivalent [60]. As the radiation is strongly beamed forward along the electron's direction of propagation, the recoil must be antiparallel to its momentum. Thus we have

$$\mathbf{F} = -\frac{2\alpha}{3}\frac{mc}{\tau_c}\eta^2 g(\eta)\hat{\mathbf{p}} \tag{3.3.12}$$

which can be rewritten in covariant form using the definition of η (3.2.2)

$$\frac{\mathrm{d}p^\mu}{\mathrm{d}\tau} = g(\eta)\frac{e^4}{6\pi\epsilon_0 m^5 c^7}\left(F_{\mu\nu}p^\nu\right)^2 p^\mu. \tag{3.3.13}$$

This is precisely the ultrarelativistic limit of the Landau-Lifshitz force (1.3.11), modified by a factor $g(\eta)$ that accounts for quantum corrections to the electron emissivity.

Adding the term (3.3.12) to the Lorentz force in the electron equation of motion results in a semi-classical model of radiation reaction. However, as the synchrotron emission rate (3.3.1) is a *probability* rate, the radiated power we derived in (3.3.9) is the *average* rate of energy loss; therefore this semi-classical model's validity is restricted to the regime where, in a given time interval, the electron emits a very large number of low-energy photons [14, 98]. Where the photon energies become a substantial fraction of the electron energy, the probabilistic nature of emission will manifest itself in deviations from this semi-classical trajectory [99]. This phenomenon is called *straggling* and its effect on gamma ray production will be discussed in detail in section 4.2.

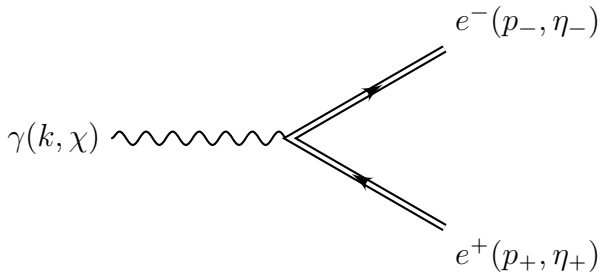

Figure 23: Feynman diagram for Breit-Wheeler pair production. An energetic photon with wavevector k and quantum parameter χ pair-produces by scattering off a large number of background photons; these are accounted for by the dressed electron and positron states.

3.4 BREIT-WHEELER PAIR PRODUCTION

The *Breit-Wheeler process* is the decay of a photon to an electron-positron pair in a strong electromagnetic field, as shown in fig. 23. It is so named by analogy with the linear QED process of two-photon pair creation $\gamma\gamma \to e^+e^-$, for which the cross-section was derived by Breit and Wheeler [100] in 1934, but which has yet to be detected experimentally[1]. This process is also referred to as *magnetic pair production* [60, 91] or simply as *pair production* [84, 17, 93, 102], where if other pair-creation mechanisms are considered, the unmodified name always refers to the process pictured in fig. 23.

The differential probability rate for a photon with energy $\hbar\omega$ and quantum parameter χ to decay to an $e^\pm$ pair with associated parameters $\eta_\pm$ is

$$\frac{\mathrm{d}W_\pm}{\mathrm{d}\eta_+} = \frac{\alpha}{\tau_\mathrm{c}} \frac{mc^2}{\hbar\omega} \chi \frac{\mathrm{d}T(\chi)}{\mathrm{d}\eta_+}. \tag{3.4.1}$$

1 An experimental geometry in which this may be possible is discussed by Pike et al. [101]

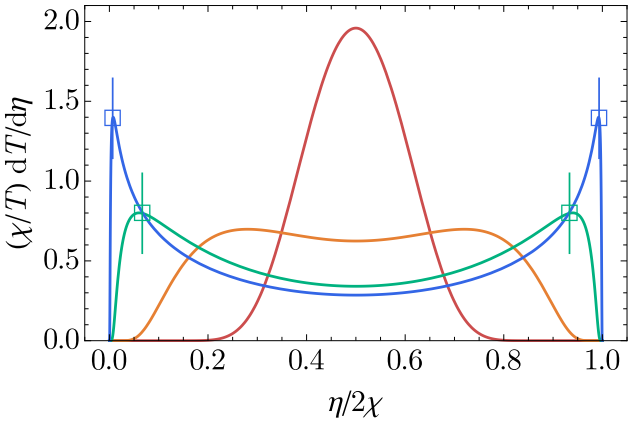

Figure 24: The partial energy distribution (3.4.2) for each particle of an electron-positron pair (normalised and then scaled by χ) produced by a photon with $\chi =$ (red) 0.1, (orange) 1, (green) 10 and (blue) 100. (boxes, vertical lines) Predicted maxima for $\chi \gg 1$, given by $\eta \simeq \chi \pm (\chi - 4/3)$.

The auxiliary function T, which controls how the photon energy is divided between electron and positron, is given by [91]

$$\frac{\mathrm{d}T(\chi)}{\mathrm{d}\eta_+} = \frac{1}{2\sqrt{3}\pi\chi^2}\left[\left(\frac{2\chi}{\eta_+} - 1 + \frac{1}{2\chi/\eta_+ - 1}\right) K_{2/3}(\delta) - \int_\delta^\infty K_{1/3}(t)\,\mathrm{d}t\right] \tag{3.4.2}$$

where

$$\delta = \frac{4\chi}{3\eta_+^2}\left(\frac{2\chi}{\eta_+} - 1\right)^{-1}. \tag{3.4.3}$$

The conservation law associated with this process is $2\chi = \eta_+ + \eta_-$. By making the substitution $\eta_- = 2\chi - \eta_+$ in (3.4.2) and (3.4.3), we find that $\mathrm{d}T(\chi)/\mathrm{d}\eta_+$, and the differential rate, are unchanged under the transformation $\eta_+ \to \eta_-$. This means that for a given energy fraction f, it is equally probable for the photon to transfer $f\hbar\omega$ to the electron as it is to the positron.

Figure 24 shows that (3.4.2) is indeed symmetric about the point $\eta = \chi$, where the photon energy is equally split between electron and positron. For $\chi \ll 1$ this is the most probable division of energy; the width of the distribution narrows as χ decreases. For $\chi \gg 1$, by contrast,

$\eta = \chi$ becomes a minimum and the transfer of almost all the photon energy to one of the electron and positron is favoured. We can estimate the size of this transfer in the limit of $\chi \to \infty$, for which $\delta \simeq 2/(3\eta)$ and $K_{2/3}(\delta) \simeq \sqrt{\pi/(2\delta)}\exp(-\delta)$ in (3.4.2). Keeping only the term $\sim 1/\chi$, we find that $\mathrm{d}T(\chi)/\mathrm{d}\eta$ has maxima at $\eta \simeq 4/3$ and $2\chi - 4/3$, where the latter arises due to the symmetry of (3.4.2) around $\eta = \chi$. Figure 24 shows that this is a good approximation for $\chi > 10$.

As the quantum synchrotron function also develops a strong maximum at the edge $\chi = \eta/2$ as η grows, we can infer that in very intense fields, a cascade of pairs and gamma rays can grow from a single high-energy particle. With each subsequent generation, most of the energy is transferred to a single particle, which creates many others of lower energy [93]. This does not mean the total energy of the cascade is confined to the initial energy of the seed particle: if the fields are sufficiently strong, any daughter electrons and positrons will be accelerated, absorbing energy that can then be converted to further gamma rays and pairs [102].

Integrating (3.4.1) over the range $0 \leqslant \eta_+ \leqslant 2\chi$, we obtain the total rate of Breit-Wheeler pair production

$$W_{\pm} = \frac{\alpha}{\tau_{\mathrm{c}}}\frac{mc^2}{\hbar\omega}\chi T(\chi) \tag{3.4.4}$$

where [60, 91, 93]

$$T(\chi) = \begin{cases} \frac{3\sqrt{3}}{8\sqrt{2}}\exp\left(-\frac{4}{3\chi}\right) & \chi \ll 1, \\ 0.60\chi^{-1/3} & \chi \gg 1. \end{cases} \tag{3.4.5}$$

Erber [60] gives the following as an analytic approximation for $T(\chi)$ valid across the full range of χ:

$$T(\chi) \simeq \frac{0.16}{\chi} K_{1/3}^2\left(\frac{2}{3\chi}\right). \tag{3.4.6}$$

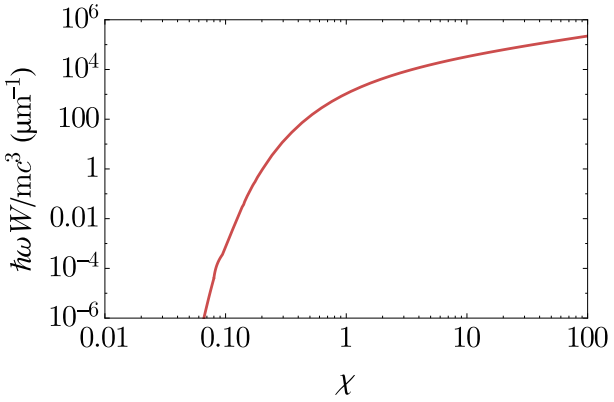

Figure 25: The probability rate (3.4.4) for a photon with energy $\hbar\omega$ and quantum parameter χ to decay to an $e^{\pm}$ pair via the Breit-Wheeler process.

The rate (3.4.4) is plotted in fig. 25. We can see that pair production is almost negligible for photons with $\chi < 0.1$ due to the exponential suppression in $T(\chi)$. For a 100 MeV gamma ray, this corresponds to a laser intensity of approximately 6×10^{22} Wcm^{-2}; if considering a laser-plasma interaction below this intensity, it would reasonable to assume that any high energy photons generated by synchrotron emission escape the region of large field at the laser focal spot without decaying.

As χ approaches 1, the pair production probability undergoes a dramatic increase. This behaviour is suggestive of a threshold being crossed, which Bassompierre et al. [103] explain using the uncertainty principle: a photon with energy $\hbar\omega$ can create a pair with longitudinal momentum $2pc$ provided that the consequent violation of energy conservation $\Delta\mathcal{E} = 2\sqrt{p^2c^2 + m^2c^4} - 2pc \simeq (mc^2)^2/\hbar\omega$ is smaller than the quantum energy fluctuation that can occur in an interval $\Delta t = \lambda_\mathrm{p}/c$, where λ_p is the pair formation length. By $\lambda_\mathrm{p} \simeq (\hbar/mc)(E_\mathrm{Sch}/E)$, the requirement that $\Delta\mathcal{E} < \hbar/(2\Delta t)$ is equivalent to $\chi > 1$, under which condition we expect pair production to become significant.

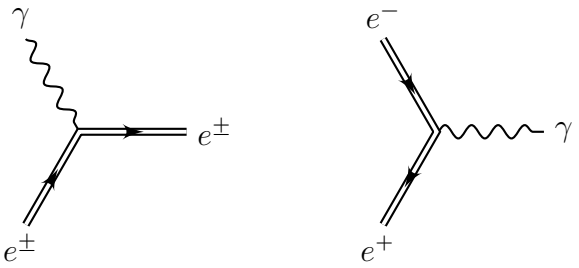

Figure 26: The remaining first-order processes are (left) photon absorption by an electron or positron and (right) electron-positron pair annihilation to a single photon.

3.5 FURTHER CONSIDERATIONS

3.5.1 *Photon absorption and pair annihilation*

There are two other processes at first order in the fine-structure constant: photon absorption by an electron; and electron-positron pair annihilation to a single photon. These processes are shown in fig. 26; we can see that they correspond to synchrotron emission and Breit-Wheeler pair creation under time reversal. However, the probabilities for both these processes are vanishingly small because there is but one particle in the final state, the four-momentum of which is restricted to a single possible value. Thus the final-state phase space collapses to a point and the cross-sections are strongly suppressed; Voroshilo et al. [104] demonstrate that for single-photon annihilation to occur, the electron and positron are required to be ultrarelativistic and collinear within an angle of 0.01 mrad. As a similar argument applies to photon absorption, it is acceptable to neglect these two processes entirely.

3.5.2 *Spin and polarisation*

The rates of the QED processes we propose including in a study of high-intensity-laser-generated plasmas in principle depend upon the spins of

the particles taking part. However, the rates (3.3.1) and (3.4.1) have been calculated for *unpolarised* emission, i.e. they have been averaged over the initial spin states and summed over the final spin states. Between these events, we should take into account the precession of the electron or positron spin in the background field. In a plane wave background this can be done semi-classically, as the expectation of spin S^μ of a Volkov state evolves according to the Bargmann-Michel-Telegdi equation [9, 105]

$$\frac{\mathrm{d}S^\mu}{\mathrm{d}t} = \frac{e}{m} F^{\mu\nu} S_\nu \tag{3.5.1}$$

which describes the Thomas precession of a classical electron with magnetic moment $e\hbar/2m$.

King et al. [106] considered pair cascades seeded by energetic electrons in a constant crossed field, including as a dynamical variable the polarisation of the photon in their calculation of the rates of emission and pair creation. While the individual rates varied with photon polarisation (up to 70% for emission and 35% for pair creation), the total pair yields calculated a) including polarisation and b) averaging over it differ only by 5%.

Their conclusion is that using average (unpolarised) rates is acceptable if the number of emission events per particle is large, as the distribution of polarisation angles becomes increasingly smoothed out with each successive generation. In a laser-plasma interaction this will always be true, as the number of photons emitted per electron per laser period is approximately $30\alpha a_0$. Were a laser to be collided with a spin-polarised electron beam, however, then the effect of polarisation would have to be included to model the pair cascade's early development correctly. A natural extension of the QED-PIC model that will be outlined in section 3.7.1.2 would be to include spin precession and polarisation dependence.

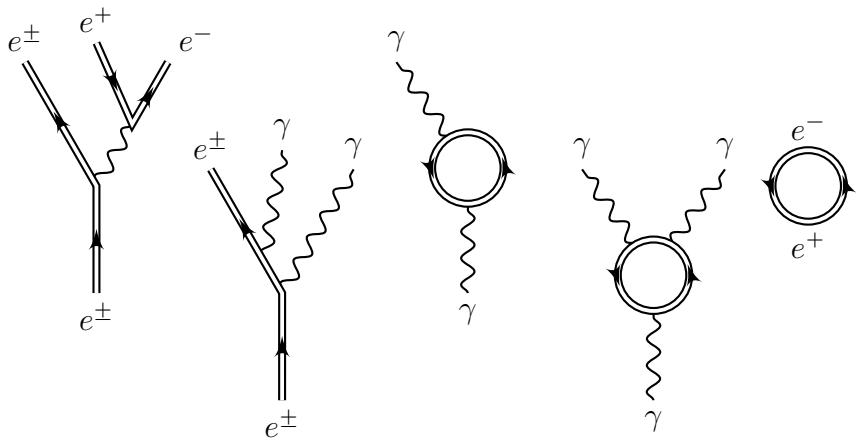

Figure 27: Some examples of higher-order QED processes. From left to right: trident pair production; double Compton scattering; Delbrück scattering; photon splitting; and vacuum pair creation.

3.5.3 *Higher order processes*

It is possible to link multiple vertices of the type shown in fig. 26 to create more complex QED interactions. However, as each additional vertex lowers the probability by a factor of the fine-structure constant $\alpha \simeq 1/137$, these are generally much less important than synchrotron emission and Breit-Wheeler pair creation. Nevertheless, it is possible that higher-order processes, some of which are pictured in fig. 27, could make non-negligible contributions in regions of phase space where the two leading processes are kinematically restricted.

Examples of higher-order processes include: trident pair production, where the mediating photon is virtual [107, 108, 88]; double Compton scattering, where two gamma rays are emitted during a single formation time [109, 110]; Delbrück scattering, where the photon is scattered by a charged vacuum fluctuation in the Coulomb field of an atomic nucleus [111, 112]; photon splitting, where the photon breaks into two photons of lower energy via a virtual electron loop [113, 114, 115]; and vacuum pair creation via the Schwinger mechanism [52].

We will consider only trident pair production in detail (see section 3.5.4), as it is the next most significant pair creation mechanism, and neglect the other possible processes. The contribution from double Compton scattering becomes comparable to that from single photon scattering when the dimension of the external field $L \ll 100\lambda/a_0$ [116], i.e in laser pulses much shorter than those we shall consider. Di Piazza and Milstein [112] find that while the presence of a laser field enhances the Delbrück scattering cross section, the scattering angle for a photon with energy $\hbar\omega$ is $\theta \lesssim mc^2/\hbar\omega \ll 1$ and the change in its energy is $\mathcal{O}(\hbar\omega_0)$, where ω_0 is the laser angular frequency[2]. The cross section for photon splitting is approximately $0.3(\alpha/\pi)^2 \simeq 1.6 \times 10^{-6}$ smaller than that for Breit-Wheeler pair production [93, sec. VI-C], which is therefore the dominant photon decay channel. Finally, the rate of vacuum pair creation in an electric field E (per unit four-volume) [117]

$$w = \frac{1}{4\pi(c\tau_c)^4}\frac{E^2}{E_{\text{Sch}}^2}\exp\left(-\frac{\pi E_{\text{Sch}}}{E}\right) \tag{3.5.2}$$

is strongly suppressed for fields well below the critical field strength. For example, even at $I = 10^{25}$ Wcm^{-2}, $w \simeq 10^{-189}$ μm^{-3}fs^{-1} is vanishingly small.

The inclusion of these processes would provide a more complete model of QED interactions with laser-plasmas; however, considering only the two leading processes of synchrotron emission and Breit-Wheeler pair creation supplies sufficient interesting physics that we leave processes other than trident pair creation for future work.

3.5.4 *Trident pair production*

The *trident process* is the creation of an electron-positron pair by an electron (or positron), where the decaying photon originates from the

2 In the absence of a laser field, Delbrück scattering is elastic.

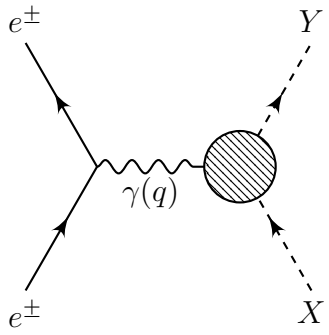

Figure 28: The Weizsäcker-Williams approximation (3.5.3) relates the cross-section for the process $e^{\pm}X \to e^{\pm}Y$ with that for $\gamma X \to Y$.

cloud of virtual particles that accompanies the parent particle. This means that the mediating photon is not necessarily on mass-shell, i.e. its four-momentum $\hbar k^2 \neq 0$.

Evaluating the cross-section for this process involves an integral over all possible values of the four-momentum transfer, including where it is null. This case, where the photon is real, corresponds to the combination of synchrotron emission and Breit-Wheeler pair creation, or 'two-step' pair creation, following Ilderton [108]. Treating the off-shell case separately then appears to draw an artificial distinction between the Breit-Wheeler and trident pair creation mechanisms. However, a full calculation of the trident rate by King and Ruhl [88] shows that the two-step part is exactly the product of the two tree-level rates; what we think of trident production here then consists of a 'pure' one-step term and cross terms that arise from interference between one-step and two-step.

We can also justify this distinction on more physical grounds: a real photon can propagate a macroscopic distance in the strong fields before pair-producing, whereas the range of a virtual photon is limited by the uncertainty principle; therefore if the typical dimension of the external field is much larger than the pair formation length, these processes are naturally differentiated.

A full calculation of the trident pair creation rate in a constant crossed field now exists [88], but has yet to be implemented in a laser-plasma simulation. Here we will discuss instead an estimate of the rate, calculated using the *Weizsäcker-Williams approximation* [118, 119] (also called the *equivalent photon approximation* [63] and the *method of virtual quanta* [25]), illustrated in fig. 28. This is that, given the cross-section for the process $\gamma X \to Y$, we can estimate the cross-section for the process $e^{\pm}X \to e^{\pm}Y$ as

$$\sigma(e^{\pm}X \to e^{\pm}Y) \simeq \int \sigma(\gamma X \to Y)\frac{\mathrm{d}N}{\mathrm{d}\omega}\,\mathrm{d}\omega \tag{3.5.3}$$

where $\mathrm{d}N/\mathrm{d}\omega$ is the spectrum of virtual photons associated with the electron. We require that the exchanged photon is nearly real for this approximation to be valid; if the electron is scattered from $\mathcal{E}$ to $\mathcal{E}'$ through an angle θ, the four-momentum transfer q has magnitude $q^2 \simeq -2\mathcal{E}\mathcal{E}'(1-\cos\theta)$. In the limit of forward scattering, this tends to zero and the photons appear real.

We can understand this from a classical perspective by considering the electric and magnetic fields of a charge q moving with constant velocity $\mathbf{v}$. When the charge is at position $\mathbf{r}$, these are [25]

$$\begin{aligned}\mathbf{E} &= \frac{\gamma q\mathbf{r}}{4\pi\epsilon_0 r^3}\left[1+\frac{\gamma^2(\mathbf{r}\cdot\mathbf{v})^2}{c^2r^2}\right]^{-3/2}\\ \mathbf{B} &= \frac{\mathbf{v}\times\mathbf{E}}{c^2}.\end{aligned} \tag{3.5.4}$$

The electric field is maximised when the charge is at its distance of closest approach to the observer b, when it is directed transverse to $\mathbf{v}$ and has magnitude $E_0 = \gamma q/(4\pi\epsilon_0 b^2)$. As that transverse field is a factor of γ larger than the maximum longitudinal field, and the time interval over which it is sustained is $\Delta t \simeq b/(\gamma c)$, an ultrarelativistic charge appears identical to a pulsed plane electromagnetic wave or, from a quantum-mechanical perspective, an assembly of photons.

We can estimate the frequency spectrum of these photons by observing that, as the pulse lasts for a time Δt, it contains frequencies up to $\omega_{\max} \simeq 1/\Delta t$. The total energy of the pulse $U = 4\pi\epsilon_0 E_0^2 b^3/\gamma$, which is distributed $\mathrm{d}U/\mathrm{d}\omega \simeq U/\omega_{\max} = e^2/(4\pi\epsilon_0 c)$. Therefore $\mathrm{d}N/\mathrm{d}\omega = (1/\hbar\omega)\mathrm{d}U/\mathrm{d}\omega \simeq \alpha/\omega$. This scaling is borne out by more thorough calculations: Jackson [25] gives the spectrum (3.5.6) used by Erber [60]; a calculation from QED in Peskin and Schroeder [63] gives

$$\frac{\mathrm{d}N}{\mathrm{d}x} = \frac{\alpha}{2\pi}\frac{1+(1-x)^2}{x}\log\left(\frac{s}{m^2}\right) \tag{3.5.5}$$

where $x = \hbar\omega/\mathcal{E}$ and the second term $(1-x)^2$ is the spin contribution neglected in a classical calculation.

Following Erber [60], Jackson [25]

$$\begin{aligned}\frac{\mathrm{d}N}{\mathrm{d}\chi} &= \frac{2\alpha}{\pi\chi}S\left(\frac{2\chi}{\eta}\right)\\ S(x) &= xK_0(x)K_1(x) - \tfrac{1}{2}x^2\left[K_1^2(x) - K_0^2(x)\right]\end{aligned} \tag{3.5.6}$$

which together with (3.4.4) and (3.4.6) yields a trident pair creation rate of

$$W_{\mathrm{tri}} \simeq \frac{\alpha^2}{\tau_{\mathrm{c}}}\frac{\eta}{\gamma}\Omega(\eta) \tag{3.5.7}$$

where the function $\Omega(\eta)$ is defined

$$\Omega(\eta) = \frac{0.16}{\pi}\int_0^\infty \frac{1}{\chi^2}K_{1/3}^2\left(\frac{2}{3\chi}\right)S\left(\frac{2\chi}{\eta}\right)\mathrm{d}\chi. \tag{3.5.8}$$

This rate is plotted in fig. 29.

King and Ruhl [88] showed that the Weizsäcker-Williams method leads to a pair creation rate that is a good approximation to the pure one-step term. However for $\chi \lesssim 20$, the cross term contribution, which is neglected entirely in this approximation, is negative, leading to an almost complete suppression of the pair creation probability. Therefore we now no longer use the rate (3.5.7). Nevertheless, discussion of the

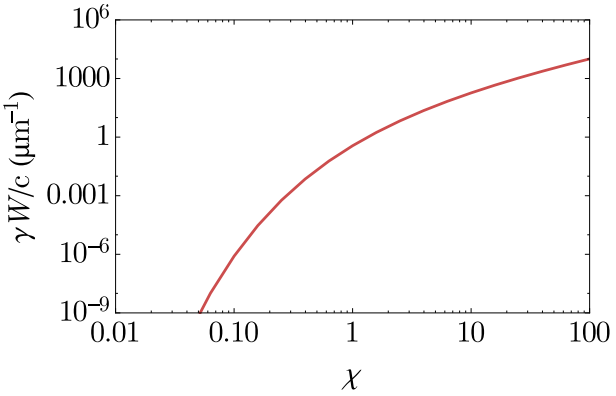

Figure 29: The probability rate (3.5.7) for an electron with Lorentz factor γ and quantum parameter η to emit an $e^{\pm}$ pair via the trident process.

same is necessary as it used in work that predates [88], such as [107, 84, 20].

3.5.5 *Limit of perturbation theory*

The contribution of radiative corrections to the electron and photon propagators means that the expansion parameter of strong-field QED is $\alpha\eta^{2/3}$ for $\eta \gg 1$ [9, 120]; thus for the results of perturbation theory, as applied to the radiation field, to be valid, we must have $\eta, \chi < 1000$.

3.6 EXPERIMENTAL VERIFICATION WITH CRYSTALS

Most of the theoretical results outlined in this chapter were obtained in the 1950-60s. However, experimental validation of non-linear effects in strong-field QED with lasers did not occur until 1997, when Burke et al. [75] demonstrated pair creation by multiphoton scattering. In that experiment a laser pulse of intensity 1.3×10^{18} Wcm^{-2} and wavelength 527 nm collided with an electron beam of energy 46.6 GeV, which parameters correspond to an a_0 of 0.36 and an η of 0.3. The latter indicates that strong-field QED is important; however, as $a_0 < 1$,

the synchrotron limit has not been reached and so the results of that experiment cannot be used to justify eqs. (3.3.2), (3.4.4) and (3.5.7).

This has, however, been done in experiments employing strong crystalline fields, as reviewed by Uggerhøj [93]. The fundamental concept is that a highly energetic particle travelling down a crystalline axis experiences a 'channelling' effect that guides it along the lattice [121]. The electric fields that arise from screened nuclei add coherently such that the particle experiences a near-constant electric field of magnitude $E \sim 10^{13}$ Vm^{-1}. For electrons with $\gamma > 10^5$, this corresponds to the regime $\eta = 1$. As the photon formation length, $\ell_\gamma = c\tau_c/\eta$ [93, sec. V], becomes small for energetic electrons, we can consider radiation from electron-beam–crystal collisions as arising from the multiple, incoherent emission of synchrotron photons in the quasistatic approximation.

These experiments have confirmed much of what has been discussed about the strong-field QED rates in this chapter: Kirsebom et al. [95] measured photon spectra for 35–243 GeV electrons incident on W crystals ($1 < \eta < 7.3$) and showed that the spin contribution to $F(\eta, \chi)$ enhances the production of the highest energy gamma rays; Andersen et al. [122] measured photon spectra for 10–150 GeV electrons incident on Ge and W ($0.048 < \eta < 0.723$) and demonstrated the onset of the quantum suppression $g(\eta)$; Belkacem et al. [123] (improving on their earlier work [124]) produced beams of 22–155 GeV photons by bremsstrahlung of 70–200 GeV electrons in a 0.5 mm lead foil and measured the pair creation yield when those photons were incident on a Ge crystal, showing that Breit-Wheeler pair production increased that yield over the Bethe-Heitler background by an amount consistent with the quasistatic approximation.

We may therefore have some confidence that the rates of synchrotron photon emission and Breit-Wheeler pair production we incorporate into

laser-plasma simulations are justified both theoretically and experimentally, provided that the quasistatic condition $a_0 \gg 1$ is fulfilled.

3.7 SIMULATING QED-PLASMAS

Now that we have discussed the QED processes of photon emission and pair creation, we can discuss how we should go about including their effects in plasma physics. It is not obvious how this can be accomplished. After all, plasmas are creatures of classical electromagnetism, where the self-consistent coupling of fields to currents, and currents to fields, are described by Maxwell's equations and the Lorentz force. In this formalism, fields and particles are distinct from one another. This is not the case in QED, where all particles, and the forces between them, arise from quantised excitations of particular fields and must be treated on the same footing.

Nevertheless, it is possible to proceed with a semi-classical approach, which was first justified by Baier and Katkov [125]. There are two changes that arise when moving from a classical to a quantum picture of electrodynamics in a strong field: firstly, that particle motion in that field must be quantised; and secondly, that the recoil caused by radiation becomes non-negligible. In the case of a static magnetic field, the former means that pairs of dynamic variables are noncommuting within a factor of order $cB/(E_{\mathrm{Sch}}\gamma^2)$; thus as the particles become more energetic, their motion becomes increasingly classical and we can neglect this first correction [91]. The effect of recoil, by contrast, is of order $\hbar\omega/\mathcal{E}$, where ω is the frequency of the emitted radiation. For $\eta \sim 1$, $\hbar\omega \sim \mathcal{E}$ and so this correction must be accounted for.

We have seen already that in very strong fields, the length over which QED processes occur is much smaller than the characteristic field length. This separation of scales between the interactions with

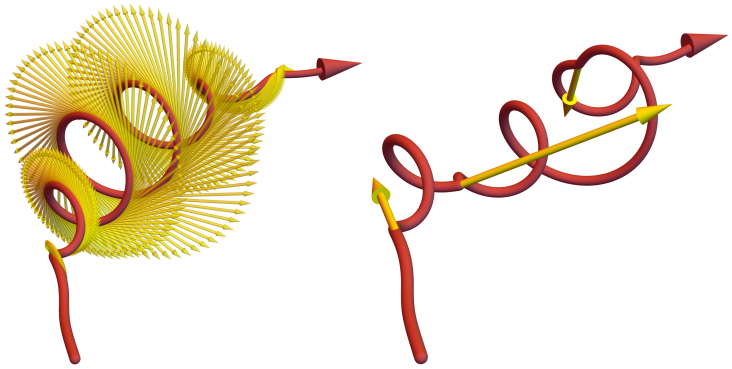

Figure 30: In the classical picture (left), electrons are subject to continuous loss of energy to radiation as determined to the Landau-Lifshitz force. In the quantum radiation reaction-dominated regime (right), this energy loss is large, discontinuous and probabilistic. However, the electron trajectory between pointlike emission events can still be determined classically.

the background and radiation fields means that we can treat the two entirely separately. Between pointlike emission events, the electron's energy loss to radiation is negligible and so its dynamics can be modelled classically using the Lorentz force. At those emission events, the interaction with the radiation field is treated perturbatively using the strong-field QED rates we have previously discussed. To quote Mackenroth and Di Piazza [110],

> One can picture [the] dynamics by considering a succession of two classical trajectories with initial four-momenta p_i^μ and p_t^μ, respectively, continuously joined at a point corresponding to the [wave] phase $\overline{\eta}_{x,1}$ where the photon with four-momentum k_1^μ is emitted.

This concept is illustrated in fig. 30.

One powerful tool for studying laser-plasma dynamics is the particle-in-cell (PIC) code. These simulate *ab initio* the self-consistent evolution of EM fields and charged particle motion according to Maxwell's equations and the Lorentz force law. The picture we have here naturally lends itself to extending the PIC algorithm to include QED processes,

which we will consider in section 3.7.1.2. First let us briefly review a standard PIC code.

3.7.1 *QED-PIC codes*

3.7.1.1 *The particle-in-cell method*

A classical plasma is an ensemble of charged particles interacting via their self-generated electromagnetic fields. In principle, therefore, we could determine the resulting dynamics by solving the set of equations

$$\frac{\mathrm{d}\mathbf{r}_i}{\mathrm{d}t} = \mathbf{v}_i \qquad \frac{\mathrm{d}\gamma_i\mathbf{v}_i}{\mathrm{d}t} = \frac{q_i}{m_i}(\mathbf{E} + \mathbf{v}_i \times \mathbf{B}) \tag{3.7.1}$$

$$\mathbf{J} = \sum_{i=1}^{N} q_i \mathbf{v}_i \delta(\mathbf{r} - \mathbf{r}_i) \tag{3.7.2}$$

$$\frac{\partial \mathbf{E}}{\partial t} = c^2 \nabla \times \mathbf{B} - \frac{\mathbf{J}}{\epsilon_0} \qquad \frac{\partial \mathbf{B}}{\partial t} = -\nabla \times \mathbf{E} \tag{3.7.3}$$

for each particle $i \in [1, N]$ with charge q_i, position $\mathbf{r}_i$, velocity $\mathbf{v}_i$ and Lorentz factor γ_i. self-consistent behaviour is achieved thus: (3.7.1) determines how the electric and magnetic fields affect particle motion; (3.7.2) how that motion gives rise to a local current density; and (3.7.3) how that current density alters the electric and magnetic fields.

Neither of Gauss's laws appear explicitly here. By taking the divergence of (3.7.3)

$$\frac{\partial}{\partial t}\nabla \cdot \mathbf{E} = -\frac{1}{\epsilon_0}\nabla \cdot \mathbf{J} = \frac{1}{\epsilon_0}\frac{\partial \rho}{\partial t} \qquad \frac{\partial}{\partial t}\nabla \cdot \mathbf{B} = 0 \tag{3.7.4}$$

we can see they provide boundary conditions for the system eqs. (3.7.1) to (3.7.3). If $\nabla \cdot \mathbf{E} = \rho/\epsilon_0 = \sum_{i=1}^{N} q_i \delta(\mathbf{r} - \mathbf{r}_i)/\epsilon_0$ and $\nabla \cdot \mathbf{B} = 0$ are initially satisfied, the continuity equation guarantees that they will remain so.

The problem with this naive approach is the sheer number of particles present in laboratory-produced plasmas. Studying a laser-solid interaction may require simulation of a plasma with density 10^{27} m^{-3} over a volume of $(10\ \mu\text{m})^3$. Tracking the position and momentum of each particle in 3D space alone would require $10^{12} \times 6 \times 8$ bytes = 44 TiB of memory. Furthermore, as each particle interacts with every other, the number of inter-particle forces that must be tracked is $N(N-1) \simeq 10^{24}$. The quadratic scaling of the latter makes direct solution of eqs. (3.7.1) to (3.7.3) impractical in almost all situations.

Reducing the scale of the problem is achieved in two ways [126, 127]. First, *collective*, rather than binary, interactions are considered. The plasma's electric and magnetic fields are defined at discrete locations in space rather than at the location of each particle. These points are generally structured into a Cartesian grid of *simulation cells*; by interpolating the plasma's local charge and current density onto these cells, we can solve Maxwell's equations to determine the time evolution of these fields. The advantage of using a grid to mediate the electromagnetic interaction between particles is two-fold: the number of interactions scales with N rather than N^2; and both Coulomb singularities and spurious large-angle scattering events are avoided by ensuring that as the inter-particle separation goes to zero, so does the force.

Second, the plasma itself is modelled using *macroparticles*: groups of plasma particles that have spatial extent but a single value of momentum (and no internal degrees of freedom). Rather than follow the trajectories of individual particles, we follow the trajectory of the macroparticle. This is determined by the force upon it, which is determined by interpolating from the fields at nearby grid points. The resultant acceleration (and so velocity and position) are independent of the number of particles in the macroparticle because they depend only on the constituent particles' charge-to-mass ratio.

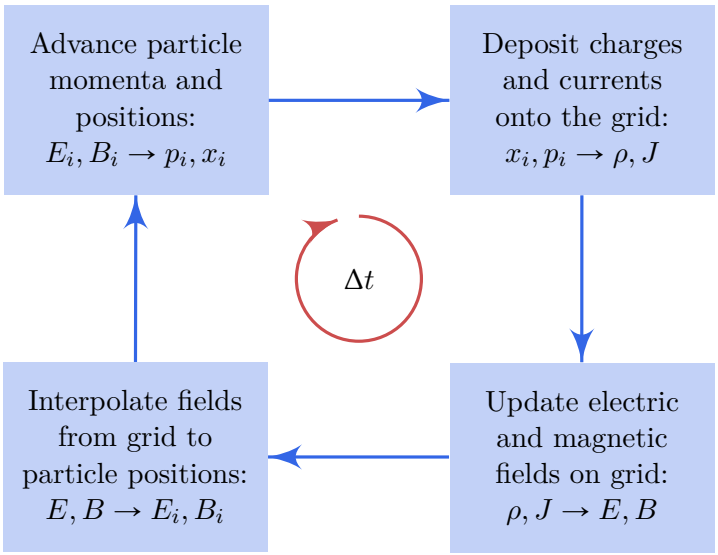

Figure 31: The structure and major operations of a collisionless PIC code.

The discretisation of the simulation domain and the algorithm followed each timestep in a PIC code are illustrated in fig. 31. Briefly:

- Given the electric and magnetic fields weighted over the macroparticle's extent, the Lorentz force is used to advance the particle's momentum and position. One of the commonly used algorithms is the *Boris push* [128]; an alternative is given by Vay [129].

- As long as the continuity equation is satisfied, then only the current arising from particle motion is needed to update $\mathbf{E}, \mathbf{B}$. Charge-conserving current deposition algorithms guarantee this by calculating the flux of macroparticle Φ_i that crosses each face of a simulation cell per timestep, with the result $J = \sum_i Q_i \Phi_i / A\Delta t$ where Q_i is the charge of each macroparticle, A the cell's cross-sectional area, and the sum runs over all macroparticles that have crossed that particular face [130].

- Given the current across each face of the cell, $\mathbf{E}, \mathbf{B}$ can be updated by solving (3.7.3). The method first described by Yee [131] involves a finite-difference time-domain discretisation over a stag-

gered mesh, with $\mathbf{E}, \mathbf{B}$ defined both half a timestep and half a cell apart.

- $\mathbf{E}, \mathbf{B}$ are then interpolated from the grid points to each macroparticle, where the weight associated with a grid point is given by the macroparticle's shape function. To conserve momentum this must be same shape function as used to calculate the flux in the current deposition step.

In practice there are more steps in the loop that handle, for example, boundary effects [132], collisions [133], and parallel decomposition of the simulation domain.

The result of this procedure is a simulation technique that is as close to a numerical experiment as can reasonably be achieved. There are, however, a number of convergence criteria that must be satisfied. The first is that the cell size must be small enough to resolve the Debye length $\Delta x < \lambda_\mathrm{D}$ or the simulated plasma will heat itself numerically, violating energy conservation, until the Debye length is resolved. The timestep must be small enough to resolve the fastest oscillation of the system (generally the plasma period $1/\omega_\mathrm{p}$) and must satisfy the Courant-Friedrichs-Lewy stability condition [134] $\Delta t < \Delta t_\mathrm{CFL} = \Delta x/c$, ensuring information cannot propagate across more than one cell in a single timestep. In a laser-solid simulation the former condition is stricter; the reverse is true for a laser-gas interaction [22]. Furthermore, the number of macroparticles per cell n determines how well the particle phase space is resolved and therefore how badly gridded quantities are affected by statistical noise. That effect can be reduced by increasing n (fluctuations scale as $1/\sqrt{n}$), but as it is difficult to determine n *a priori*, it is generally set by trial and improvement.

3.7.1.2 *A Monte Carlo approach to including QED*

Extending the PIC scheme to include the QED processes of synchrotron emission and Breit-Wheeler pair production has been accomplished in a number of codes [135, 136] by implementing a Monte Carlo algorithm of the kind described by Duclous et al. [17], Ridgers et al. [22] as an additional step in the PIC loop.

The probability of a QED process $P = 1 - e^{-\tau}$, where τ is the *optical depth* of the electromagnetic fields against that particular process. Each electron, position and gamma-ray photon is assigned a 'final' optical depth against photon emission and pair creation by solving $R = 1 - e^{-\tau_\mathrm{f}}$ with pseudorandom $R \in [0, 1]$. The particle's current optical depth τ is then integrated along its trajectory according to

$$\frac{\mathrm{d}\tau}{\mathrm{d}t} = W, \tag{3.7.5}$$

where W is the rate of the QED process in question, until $\tau = \tau_\mathrm{f}$. Emission, or pair creation, is deemed to occur at this point.

If $W = W_\gamma$ (synchrotron photon emission), then the χ of the emitted photon is determined by solving

$$R\, h(\eta) = \int_0^\chi \frac{F(\eta, \chi')}{\chi'}\, \mathrm{d}\chi' \tag{3.7.6}$$

where η is the quantum parameter of the emitting electron or positron, R is a new pseudorandom number in the interval $(0, 1]$, and $h(\eta)$ and $F(\eta, \chi)$ are as given in eqs. (3.3.3) and (3.3.4). As for ultrarelativistic particles radiation is strongly beamed in the forward direction, the four-momenta of the photon and the recoiling electron are given by

$$\hbar k^\mu = \frac{2\chi}{\eta}\left(|\mathbf{p}|, \mathbf{p}\right) \qquad p'^\mu = \left[\frac{\mathcal{E}'}{c}, \left(1 - \frac{2\chi}{\eta}\right)\mathbf{p}\right] \tag{3.7.7}$$

where $\mathcal{E}'$ is set such that $p'^2 = (mc)^2$. This conserves momentum but not energy[3], with error [17, 22]

$$\Delta\mathcal{E} \simeq \frac{\mathcal{E}}{2}\left(\frac{1}{\gamma} - \frac{1}{\gamma'}\right). \tag{3.7.8}$$

which we interpret as energy transfer from the classical background fields; for $\gamma, \gamma' \gg 1$ this quantity is negligible. Following emission, the electron's τ_f is reset and a new photon is added to the simulation at the emission location with the specified momentum. Thereafter it propagates ballistically with constant momentum.

A particle, rather than wave, description of the photon is necessary because discretising $\mathbf{E}, \mathbf{B}$ over a grid with spacing Δ introduces a momentum cutoff $\hbar/\Delta \ll (2\chi/\eta)\gamma mc$. This implies there is some double counting of photons, as the electron's classical motion is also a source of coherent radiation via Maxwell's equations; however, that double counting only occurs in the low-frequency part of the spectrum and is therefore negligible.

A similar scheme is followed if $W = W_\pm$ (Breit-Wheeler pair production). The η of the electron[4] is determined by solving

$$R \cdot T(\chi) = \int_0^\eta \frac{\mathrm{d}T(\chi)}{\mathrm{d}\eta'}\,\mathrm{d}\eta' \tag{3.7.9}$$

where χ is the quantum parameter of the decaying photon, R is a pseudorandom number in the interval $[0, 1]$, and the auxiliary functions $\mathrm{d}T(\chi)/\mathrm{d}\eta$ and $T(\chi)$ are as given in eqs. (3.4.2) and (3.4.5). The energies of the daughter electron and positron are then given by

$$p_-^\mu = \left(\frac{\mathcal{E}_-}{c}, \frac{\eta}{2\chi}\hbar\mathbf{k}\right) \qquad p_+^\mu = \left[\frac{\mathcal{E}_+}{c}, \left(1 - \frac{\eta}{2\chi}\right)\hbar\mathbf{k}\right] \tag{3.7.10}$$

3 In principle one could choose to conserve energy instead. We have chosen to conserve momentum as, unlike energy, it is conserved by standard PIC codes [126]

4 This scheme would be unchanged if η were instead assigned to the positron, by the results of section 3.4.

where $\mathcal{E}_\pm$ are set such that $p_\pm^2 = (mc)^2$. As before, this implies a (negligible) violation of energy-momentum conservation due to the transfer of energy from the background fields. The electron and positron are added to the simulation at the point of emission and the photon removed.

The addition of QED processes to a PIC code introduces a further constraint on the size of the timestep: it must be small enough that the probability of more than one QED event occurring during that interval is very small [22]. This is set by the maximum possible rate of photon emission, not pair production, as by eqs. (3.3.2) and (3.4.4)

$$\frac{\max W_\gamma}{\max W_\pm} = \frac{\sqrt{3}}{\pi}\frac{\max h}{\max T} \simeq 17. \tag{3.7.11}$$

Assuming that the largest electric field in the system is that of the laser, we require that $\Delta t < \Delta t_{\mathrm{QED}}$, where

$$\Delta t_{\mathrm{QED}} = \frac{1}{\max W_\gamma} = \left(\frac{5\alpha}{\sqrt{3}\tau_{\mathrm{c}}}\frac{E}{E_{\mathrm{Sch}}}\right)^{-1} \simeq \frac{8\lambda}{a_0 c}. \tag{3.7.12}$$

If in the absence of QED the timestep would have been set by the need to resolve the Debye length, as in a laser-solid interaction, then

$$\Delta t < \frac{\lambda_{\mathrm{D}}}{c} = \frac{a_0}{16\pi}\left(\frac{n_{\mathrm{cr}}}{n_e}\frac{kT}{mc^2}\right)^{1/2}\Delta t_{\mathrm{QED}}. \tag{3.7.13}$$

Typical electron densities $n_e \sim 10^3 n_{\mathrm{cr}}$ and temperatures $kT \sim 10^3 mc^2$, so $\Delta t < \Delta t_{\mathrm{QED}}$ only becomes a stronger constraint if $a_0 > 5 \times 10^4$. If instead the CFL condition were stricter, as in a laser-gas interaction, then

$$\Delta t < \frac{\lambda}{cn} = \frac{a_0}{8n}\Delta t_{\mathrm{QED}} \tag{3.7.14}$$

where n cells are used to resolve the laser wavelength. Assuming $n = 10$, $a_0 > 100$ is required for Δt_{QED} to set the timestep.

We noted earlier that the number of macroparticles per cell must be large enough such that the particle phase space is sufficiently well sampled. The steep increase in the pair production rate for $\chi \sim 0.1$ (see fig. 25) means that, at threshold, the number of pairs produced is strongly dependent on the yield of the highest energy gamma rays. If there are insufficiently many macroelectrons to resolve the high-energy tail of the photon spectrum, then any information gathered on the pair population will be subject to damaging statistical noise. Therefore a numerical study of pair creation will require many more macroparticles than a study of photon production only.

Furthermore, at very high laser intensities, a single particle can trigger a QED cascade, with the result that an exponentially growing number of photons, electrons and positrons must be tracked [102, 18]. This greatly increases the computational load of such a simulation, though a means of controlling this by merging macroparticles has recently been put forward by Vranic et al. [137]. Alternatively, if pair production is not dynamically significant, photons can be deleted upon generation and only the radiating electrons tracked [22].

QED-PIC Monte-Carlo codes have now been used to study laser-solid interactions at 10^{22} to 10^{25} Wcm^{-2} [11, 21, 138] and laser-laser interactions at $>10^{23}$ Wcm^{-2} [18, 139, 140]. The simulations that I have carried out, results from which will be described in chapter 4, used codes that implement simplified versions of the QED-PIC algorithm.

3.7.2 *Alternative approaches*

3.7.2.1 *Classical radiation reaction and PIC*

If one wished to simulate laser-plasma interactions where $\eta \ll 1$ and a semi-classical approach sufficed, one could modify the particle push stage in fig. 31 to incorporate radiation reaction in the Landau-Lifshitz

prescription, rather than implement the full Monte-Carlo algorithm outlined in section 3.7.1.2. Authors that have done this include Tamburini et al. [141], Thomas et al. [14], Vranic et al. [142].

However, as discussed in section 3.3.3, this approach neglects probabilistic effects that allow radiating electrons to deviate from the trajectories they would otherwise follow. Furthermore, quantum corrections manifest themselves in a factor $g(\eta)$ that reduces the radiated power by 5% at $\eta = 0.01$, 21% at $\eta = 0.05$ and 34% at $\eta = 0.1$. Only Thomas et al. of the authors given above account for this (but find it can be neglected for the configuration they study).

We will discuss both these effects in section 4.2, finding that while including $g(\eta)$ means that the electron spectra predicted by semi-classical and quantum radiation reaction are nearly consistent, the photon spectra differ substantially. One could not, therefore, expect a model that includes radiation classically to predict pair production with great accuracy.

3.7.2.2 *Solving kinetic equations*

An alternative method involves studying the particle distribution functions, rather than the particles themselves. Let the number of electrons (or positrons) with position $\mathbf{x}$ and momentum $\mathbf{p}$ at time t be given by $f_{\pm}(t, \mathbf{x}, \mathbf{p})\mathrm{d}^3\mathbf{x}\mathrm{d}^3\mathbf{p}$, and the number of photons with position $\mathbf{x}$ and momentum $\hbar\mathbf{k}$ be $f_{\gamma}(t, \mathbf{x}, \hbar\mathbf{k})\mathrm{d}^3\mathbf{x}\mathrm{d}^3\hbar\mathbf{k}$. The distribution functions $f_{\pm}, f_{\gamma}$ are Lorentz scalars and therefore in the absence of collisions, or processes that change particle number, they must obey the following continuity equation

$$\frac{\partial}{\partial x^{\mu}}\left(\frac{\partial x^{\mu}}{\partial \tau} f\right) + \frac{\partial}{\partial p^{\mu}}\left(\frac{\partial p^{\mu}}{\partial \tau} f\right) = 0 \tag{3.7.15}$$

where the proper time τ is measured along the world-line of the six-dimensional volume element.

By recognising that $\mathbf{x}, \mathbf{p}$ are independent variables, that the particle distributions f are not parametrised by the Lorentz factor $\gamma = \sqrt{1 + (\mathbf{p}/mc)^2}$, and that the Lorentz force $qF^{\mu\nu}p_\nu/(mc)$ is divergence-free in momentum space, we can expand (3.7.15) to obtain *Vlasov equations* for the electron, positron and photon populations

$$\frac{\partial f_\pm}{\partial t} + \frac{\mathbf{p}}{\gamma m} \cdot \frac{\partial f_\pm}{\partial \mathbf{x}} \pm e\left(\mathbf{E} + \frac{\mathbf{p} \times \mathbf{B}}{\gamma m}\right) \cdot \frac{\partial f_\pm}{\partial \mathbf{p}} = 0 \tag{3.7.16}$$

$$\frac{\partial f_\gamma}{\partial t} + c\hat{\mathbf{k}} \cdot \frac{\partial f_\gamma}{\partial \mathbf{x}} = 0. \tag{3.7.17}$$

$\mathbf{E}, \mathbf{B}$ are the self-consistent electric and magnetic fields, generated by the charge and current densities

$$\rho = \sum_i q_i \int f_i(t, \mathbf{x}, \mathbf{p})\, \mathrm{d}^3\mathbf{p} \qquad \mathbf{J} = \sum_i q_i \int \frac{\mathbf{p} f_i(t, \mathbf{x}, \mathbf{p})}{\gamma m}\, \mathrm{d}^3\mathbf{p} \tag{3.7.18}$$

where the sum runs over all species i.

Including QED processes in this system is accomplished by adding terms to the right hand side of eqs. (3.7.16) and (3.7.17). Following Elkina et al. [102], Sokolov et al. [143], we must add to the electron/-positron Vlasov equation

$$\begin{aligned}\left.\frac{\partial f_\pm}{\partial t}\right|_{\mathrm{QED}} = &\int f_\pm(t, \mathbf{x}, \mathbf{p}')\, \mathcal{W}_\gamma(\mathbf{p}', \mathbf{p}' - \mathbf{p})\, \mathrm{d}^3\mathbf{p}' \\ &- f_\pm(t, \mathbf{x}, \mathbf{p}) \int \mathcal{W}_\gamma(\mathbf{p}, \hbar\mathbf{k})\, \mathrm{d}^3\hbar\mathbf{k} \\ &+ \int f_\gamma(t, \mathbf{x}, \hbar\mathbf{k})\, \mathcal{W}_\pm(\hbar\mathbf{k}, \mathbf{p})\, \mathrm{d}^3\hbar\mathbf{k}\end{aligned} \tag{3.7.19}$$

and to the photon Vlasov equation

$$\begin{aligned}\left.\frac{\partial f_\gamma}{\partial t}\right|_{\mathrm{QED}} = &\int \left[f_-(t, \mathbf{x}, \mathbf{p}) + f_+(t, \mathbf{x}, \mathbf{p})\right] \mathcal{W}_\gamma(\mathbf{p}, \hbar\mathbf{k})\, \mathrm{d}^3\mathbf{p} \\ &- f_\gamma(t, \mathbf{x}, \hbar\mathbf{k}) \int \mathcal{W}_\pm(\hbar\mathbf{k}, \mathbf{p})\, \mathrm{d}^3\mathbf{p}.\end{aligned} \tag{3.7.20}$$

Here $\mathcal{W}_\gamma(\mathbf{p}, \hbar\mathbf{k})$ is the probability rate for an electron or positron with momentum $\mathbf{p}$ to emit a photon with momentum $\hbar\mathbf{k}$

$$\mathcal{W}_\gamma(\mathbf{p}, \hbar\mathbf{k}) = \int_0^{\eta/2} \frac{\mathrm{d}W_\gamma}{\mathrm{d}\chi}\, \delta\left(\hbar\mathbf{k} - \frac{2\chi}{\eta}\mathbf{p}\right) \mathrm{d}\chi \tag{3.7.21}$$

and $\mathcal{W}_\pm(\hbar\mathbf{k}, \mathbf{p})$ the probability rate for a photon with momentum $\hbar\mathbf{k}$ to decay to an electron-positron pair where the electron has momentum $\mathbf{p}$

$$\mathcal{W}_\pm(\hbar\mathbf{k}, \mathbf{p}) = \int_0^{2\chi} \frac{\mathrm{d}W_\pm}{\mathrm{d}\eta}\, \delta\left(\mathbf{p} - \frac{\eta}{2\chi}\hbar\mathbf{k}\right) \mathrm{d}\eta. \tag{3.7.22}$$

The δ-functions ensure that daughter particles are emitted parallel to the emitting particle's momentum. When integrated over all possible final momenta, these rates satisfy $\int \mathcal{W}_\gamma(\mathbf{p}, \hbar\mathbf{k})\, \mathrm{d}^3\hbar\mathbf{k} = W_\gamma$ and $\int \mathcal{W}_\pm(\hbar\mathbf{k}, \mathbf{p})\, \mathrm{d}^3\mathbf{p} = W_\pm$.

The three terms in (3.7.19) are, respectively: population increase due to electrons that have fallen from higher momentum states by radiating; population decrease due to electrons radiating and falling to lower momentum states; and population increase by pair production from photons in the same spatial element. The two terms in (3.7.20) are: population increase due to radiation from electrons and positrons in the same spatial element; and population decrease by the decay of photons in the local phase space element.

Equations (3.7.16) to (3.7.20) comprise a system of six-dimensional, nonlinear integro-differential equations that determine the coupled evolution of the electron, positron and photon distribution functions and the self-consistent electric and magnetic fields. This system can be discretised in as many dimensions as necessary to model a particular problem and then solved numerically; examples include studies of pair cascades by Sokolov et al. [143], Bulanov et al. [144] and laser–electron-beam collisions by Neitz and Di Piazza [19]. We would expect their results to be consistent with those from Monte-Carlo PIC simula-

tions (provided that convergence and stability criteria have been met for both) as the probabilistic nature of emission is accounted for by the integral over all kinematically possible η, χ in eqs. (3.7.21) and (3.7.22).

The advantage of this method is that, by spreading the computational effort over the particle phase space rather than the particles themselves, situations in which a small fraction of the distribution has a disproportionately large effect on the physics (such as pair production near threshold) can be modelled more efficiently than they would be by a PIC code. However, as the full phase space must be resolved, this can mean significant computational effort is expended on regions with very few particles that are not actually of interest. A PIC code, by contrast, places resolution in regions where there are most particles and therefore naturally adapts the resolution with time.

Furthermore, the equations that must be solved are much more complicated than the set used by a PIC code: eqs. (3.7.1) to (3.7.3) are linear and the Monte-Carlo algorithm in section 3.7.1.2 requires only local information about each macroparticle. The requirement to resolve the whole phase space sufficiently finely to prevent artificial diffusion and dispersion of the particle distribution function means that Vlasov codes tend to run much more slowly than PIC codes. This was borne out by a comparison between the kinetic code used by Neitz and Di Piazza [19] and the Monte-Carlo code of Blackburn et al. [20] [145].

3.7.2.3 *Solving fluid equations*

The Vlasov equations eqs. (3.7.16) and (3.7.17) can be reduced in scale by averaging over the momenta of the individual particles [146, ch. 1.3]. By taking *moments* of the distribution we dispense with detailed information about the particle distribution in momentum space, but gain a

series of simpler equations. For example, the first moment, obtained by integrating (3.7.15) over all momenta, is (neglecting pair production)

$$\frac{\partial n}{\partial t} + \frac{\partial}{\partial \mathbf{x}} \cdot (n\bar{\mathbf{u}}) = 0 \tag{3.7.23}$$

where n is the fluid number density and $\bar{\mathbf{u}} = \int \mathbf{p} f/(\gamma m)\, \mathrm{d}^3\mathbf{p}$ its four-velocity. This expresses continuity of the particle density; the next moment expresses the conservation of momentum. While the moment equations comprise an infinite series, this can be truncated by adding an equation of state for the fluid.

These *fluid equations* are much more amenable to analytical solution than kinetic equations: a notable example would be Kirk et al. [147], who found that the cold two-fluid equations with classical radiation reaction permit a static solution for an electron-positron pair plasma behind the hole-boring front driven by an incident laser pulse. In this solution, the radiation pressure of the reflected laser pulse is balanced against the energy density of a standing wave in the vacuum gap between pair plasma and hole-boring front; energy is conserved as the pairs radiate gamma rays perpendicular to the laser propagation axis.

However, when accounting for the fluid's loss of energy to gamma rays, we must recognise that as the synchrotron power $\mathcal{P}_\gamma$ depends non-linearly on the momentum, we cannot in general assert that $\overline{\mathcal{P}_\gamma(\eta)} = \mathcal{P}_\gamma(\overline{\eta})$, where $\overline{\eta}$ is the η associated with the fluid velocity $\bar{\mathbf{u}}$. Doing so is an approximation must be tested against kinetic models.

3.8 EXPERIMENTAL VERIFICATION WITH LASERS?

The plasmas that are being studied with models that incorporate QED require lasers with intensities that exceed 10^{23} Wcm^{-2}, which is an order of magnitude greater than the current intensity frontier of 10^{22} Wcm^{-2} [1,

54]. While facilities that can reach these intensities are planned [3], it is reasonable to ask if radiation reaction and strong-field QED could be measured in an experiment using existing high-power lasers. Such an experiment is the subject of the next chapter.

4

COLLIDING BEAMS: AN EXPERIMENTAL ROUTE TO STRONG-FIELD QED

4.1 INTRODUCTION

We have seen that the importance of strong-field QED effects may be quantified with the parameter

$$\eta = \frac{\sqrt{-(F_{\mu\nu}p^{\nu})^2}}{mcE_{\text{Sch}}} \tag{4.1.1}$$

where $F_{\mu\nu}$ is the electromagnetic field tensor and $p^{\mu} = \gamma m(c, \mathbf{v})$ the electron four-momentum. η compares the magnitude of the electric field in the electron's rest frame to that of the critical field of QED $E_{\text{Sch}} = 1.3 \times 10^{18}$ Vm^{-1}, which can produce electron-positron pairs directly from the vacuum.

For highly relativistic electrons, (4.1.1) becomes

$$\eta \simeq \frac{\gamma\,|\mathbf{E}_{\perp} + \mathbf{v} \times \mathbf{B}|}{E_{\text{Sch}}} \tag{4.1.2}$$

where γ is the electron Lorentz factor, $\mathbf{B}$ the magnetic field and $\mathbf{E}_{\perp}$ the electric field component perpendicular to $\mathbf{v}$. In a laser-plasma interaction we would expect the electrons to have $\gamma \simeq a_0$, where $a_0 = [I(\lambda/\mu\text{m})^2/1.37 \times 10^{18}\ \text{Wcm}^{-2}]^{1/2}$ is the laser's strength parameter, I its intensity and λ its wavelength. Then the typical $\eta \simeq I\lambda/(5.65 \times 10^{23}\ \text{Wcm}^{-2}\mu\text{m})$ and intensities $> 10^{23}$ Wcm^{-2} would be necessary to observe strong-field QED effects.

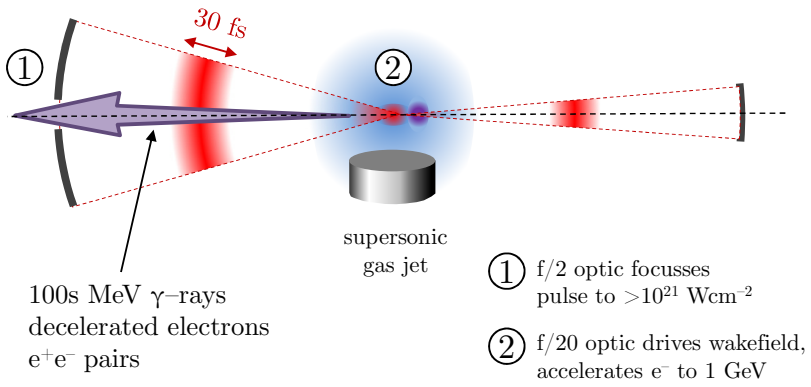

Figure 32: The collision of an intense laser pulse and energetic electron beam could demonstrate both the quantum nature of radiation reaction and pair production. GeV electrons, accelerated by a laser wakefield in a supersonic gas jet, radiate much of their energy to gamma rays in the large fields of the target laser pulse. These gamma rays then pass through an aperture in the $f/2$ focusing optic. (From Blackburn et al. [20].)

However, if the electrons are pre-accelerated to high energies before encountering the high field region, the QED-dominated regime can be reached using much lower field strengths. This was exploited in experiments at the SLAC facility [75] and at the CERN Super Proton Synchrotron [122]: in SLAC experiment E144 the collision of a 46.6 GeV electron beam and laser pulse of intensity 10^{18} Wcm^{-2} was observed to produce electron-positron pairs by photon–photon scattering; in the latter experiment at SPS, a 100 GeV electron beam incident on, and channelled down a crystal axis of, germanium experienced an effective electric field of 10^{13} Vm^{-1}, emitting gamma rays and pairs in accordance with strong-field QED theory.

The advent of high energy wakefield-accelerated electron beams [78, 148] and intense short pulses now raises the possibility that these experiments could be repeated with an all-optical setup in today's laser facilities. An electron with energy $\mathcal{E}$ colliding with a laser pulse with

intensity I and wavelength λ will radiate in a single laser period a fraction of its energy equal to

$$f = \frac{\mathcal{P}_\gamma \lambda}{\mathcal{E} c} = 0.42 \left(\frac{\mathcal{E}}{\text{GeV}}\right) \left(\frac{I}{10^{21}\ \text{Wcm}^{-2}}\right) \left(\frac{\lambda}{\mu\text{m}}\right) \tag{4.1.3}$$

which is greater than 50% for parameters that could be achieved today; it is necessary, therefore, to include radiation reaction in the electron's equation of motion.

Furthermore, as the quantum parameter for such an electron

$$\eta = 0.26 \left(\frac{\mathcal{E}}{\text{GeV}}\right) \left(\frac{I}{10^{21}\ \text{Wcm}^{-2}}\right)^{1/2} \tag{4.1.4}$$

is $\mathcal{O}(1)$ at the current intensity frontier, both the damping factor $g(\eta)$ and the stochastic nature of emission must be accounted for. The latter arises because the typical energy of a radiated photon for $\eta < 1$ is $\hbar\omega \simeq 0.43\eta\gamma mc^2$ (see section 3.3.1); when $\eta \simeq 1$, an electron can lose a substantial fraction of its energy in a single emission. This leads to deviations from the trajectory it would follow classically, or *straggling*.

We will first discuss how straggling allows quantum and classical radiation reaction to be distinguished in a laser-electron-beam collision, summarising the findings of Blackburn et al. [20]. Thereafter we will extend that analysis and consider how the angle of collision and spatial and temporal offsets affect the viability of diagnosing quantum radiation reaction with the resultant gamma ray and electron beam energy spectra.

4.2 THE IMPORTANCE OF STRAGGLING

A quantum-mechanical description of radiation differs from a classical description in two ways. First, corrections to the emission spectrum cut off the tail of photons with energies greater than that of the electron

but include the contribution from spin-flip transitions. The result is that the radiated power is reduced by the factor $g(\eta) \in (0, 1]$ described in section 3.3.2.

The second will prove more significant for $\eta \simeq 0.1$, which parameter regime we consider here. In a classical description, the electron would accelerate along its worldline radiating continuously. However, we saw in section 3.3.1 that the typical fraction of electron energy carried off by a single photon is 0.44η for $\eta \ll 1$ and $1 - 4/(3\eta)$ for $\eta \gg 1$; therefore as η approaches 1, radiative losses must be treated discontinuously. As photon emission is stochastic in nature, it must be described in terms of the probability to emit a gamma ray of given energy. This gives rise to a phenomenon called *straggling* [17, 99].

Straggling refers to those electrons that propagate significant distances without radiating, thereby accessing regions of phase space that would be otherwise inaccessible. For example, Duclous et al. [17] show that in the standing wave of two colliding, circularly-polarised laser beams, a classical electron in periodic motion absorbs and emits the same amount of energy from orbit to orbit. A stochastically radiating electron can absorb more energy from the laser fields if its emission is delayed; these straggling electrons reach higher energies, emit harder gamma rays and enhance the absorption of laser energy.

The case under consideration here is the collision of an ultrarelativistic electron beam and a laser pulse. As that laser pulse will have a non-uniform spatial intensity profile, straggling means that some electrons will reach the region of highest intensity at the pulse centre having radiated away little to no energy. The η of those electrons is then boosted well above that which classical electrons could reach. The non-linearity of $F(\eta, \chi)$ means that a small increase in η causes a large increase in the tail of the spectrum, and so the yield of the most energetic gamma rays.

We saw in section 3.4 that the rate of Breit-Wheeler pair production (3.4.4) undergoes a dramatic increase for photons with $\chi \simeq 0.1$. If the high-energy tail of the photon spectrum is enhanced by straggling, so too will be the yield of electron-positron pairs. It may then be possible to observe light-by-light pair creation in the highly non-linear regime (i.e. $a_0 \gg 1$) and extend the findings of Burke et al. [75].

To quantify the difference between classical and quantum radiation reaction, we will compare a fully stochastic model that implements the Monte Carlo algorithm given in section 3.7.1.2, with a semi-classical model, as outlined in sections 3.3.3 and 3.7.2.1. In the latter the electron loses energy continuously according to the Landau-Lifshitz force modified by the damping factor $g(\eta)$:

$$\frac{\mathrm{d}\gamma}{\mathrm{d}t} = -\frac{2\alpha}{3}\frac{\eta^2}{\tau_\mathrm{c}}g(\eta). \tag{4.2.1}$$

To satisfy energy conservation, photon spectra must be generated by sampling the same quantum synchrotron distribution (3.3.1) that the stochastic model does. We shall refer to this as *continuous radiation reaction*.

We will use these models to simulate the collision of a GeV electron beam and laser pulse of intensity in the range 10^{21} to 3×10^{22} Wcm^{-2}. To simplify our analysis of this interaction, we make the rigid-beam approximation and neglect the effects on the electron motion of the laser fields and the space-charge field of the electron beam. From section 2.6.2, this is acceptable if the electron Lorentz factor $\gamma \gg a_0$, the strength parameter of the laser, and $\gamma \gg 1$. If so, the electron propagates ballistically at the speed of light through the laser pulse.

The three strong-field QED processes included are: synchrotron photon emission, trident pair production and Breit-Wheeler pair production. The timestep must be small enough that multiple QED events do not occur, i.e. $\Delta t < \Delta t_\mathrm{QED}$ where Δt_QED is given by (3.7.12). The high-

est intensity we will consider is 3×10^{22} Wcm^{-2} ($a_0 \simeq 150$), for which $\Delta t_{\mathrm{QED}} = 0.18$ fs. Therefore for all simulations we set $\Delta t = 0.01$ fs.

The parameters of the interaction are: the laser pulse is linearly polarised, has wavelength $\lambda = 1$ μm and Gaussian temporal and radial intensity profiles, with full width at half-maximum (FWHM) $f = 30$ fs and waist $w_0 = 2.2$ μm respectively; the electrons have initial Lorentz factor $\gamma_0 = 2000$ and counter-propagate along the laser optical axis. Therefore the $\mathbf{E}_\perp$ and $\mathbf{v} \times \mathbf{B}$ terms in η add and $\eta = 2\gamma E/E_{\mathrm{Sch}}$. In terms of the wave phase $\phi = kx - \omega t$,

$$E = E_0 \exp\left(-\frac{r^2}{w_0^2} - \frac{2\ln 2\,\phi^2}{\omega^2 f^2}\right)\cos\phi \tag{4.2.2}$$

where the peak electric field E_0 is related to the intensity I and strength parameter a_0 by $I = \frac{1}{2}c\epsilon_0 E_0^2$ and $a_0 = eE/(mc\omega)$. The largest a_0 that will be encountered is $150 \ll \gamma_0$, so the electron is indeed ultrarelativistic and undeflected, with $\phi = -2\omega t$ and r constant. At each timestep, we calculate $\eta = 2\gamma(\phi)E(\phi)/E_{\mathrm{Sch}}$ to generate QED events according to section 3.7.1.2.

Figure 33 shows the $\mathcal{E}(t), \eta(t)$ of a particular stochastically radiating GeV electron colliding with a laser pulse of intensity 5×10^{21} Wcm^{-2}, comparing it to a continuously radiating electron. In this case the electron has lost more energy than the classical prediction; however, as that final energy will vary from electron to electron, the energy distribution of an initially mono-energetic electron beam will broaden over the course of the collision. Furthermore, the electron has propagated deep into the laser pulse without losing much energy, reaching a maximum $\eta = 0.51$. This exceeds that which would be reached by an electron subject to continuous loss of energy ($\eta = 0.33$), with the consequence that the emission of a single high-energy photon becomes more likely. In this case a photon is created with $\hbar\omega = 776$ MeV and $\chi = 0.198$, well into the regime where Breit-Wheeler pair creation becomes possible.

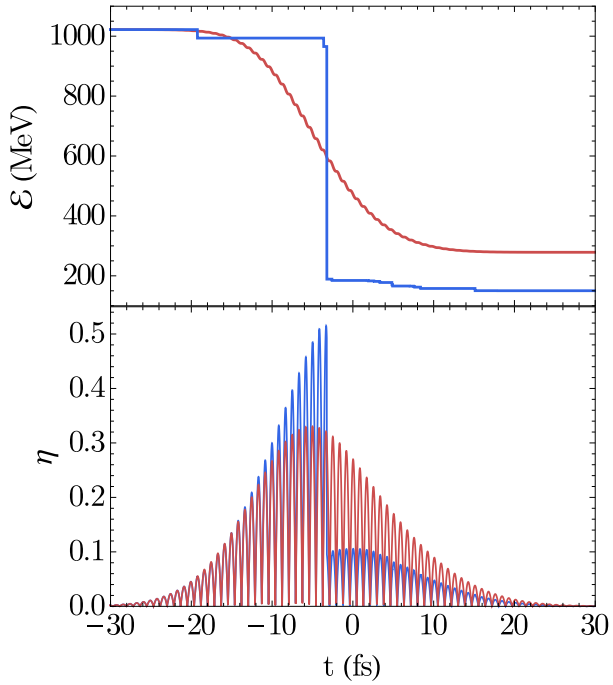

Figure 33: The energy and η of a GeV electron colliding with a laser pulse that has peak intensity 5×10^{21} Wcm^{-2} at $t = 0$. Red corresponds to continuous radiation reaction as given by (4.2.1); blue is one example of stochastic radiation reaction.

Straggling should therefore: enhance the yield of the highest energy gamma rays; enhance the yield of electron-positron pairs; and broaden the final energy distribution of an initially mono-energetic electron beam. Let us consider each of these in turn.

4.2.1 *To the gamma ray spectrum*

Our simulations show that, for both stochastic and continuous radiation reaction, the total number of photons (per electron) N_γ/N_e emitted by an initially mono-energetic 1 GeV electron beam colliding with a 30 fs plane-wave laser pulse is

$$\frac{N_\gamma}{N_e} = 13.7 I_{21}^{1/2}, \tag{4.2.3}$$

where $1 \leqslant I_{21} \leqslant 30$ is the peak laser intensity measured in units of 10^{21} Wcm^{-2}. This scaling arises because the total rate of photon emission $\sim \eta h(\eta)$, $\eta \sim I_{21}^{1/2}$ and $h(\eta)$ is slowly varying for $\eta < 1$.

However, the scalings differ if we consider the high energy tail of the spectrum. Fitting to the Monte-Carlo data, we find

$$\frac{N_\gamma(\hbar\omega \geqslant 500 \text{ MeV})}{N_e} \simeq \begin{cases} 8.81 \times 10^{-3} \log(1.39 I_{21}) & \text{stochastic r. r.} \\ 1.67 \times 10^{-3} \log(1.81 I_{21}) & \text{continuous r. r.} \end{cases} \tag{4.2.4}$$

which is accurate within 1% for $I_{21} \geqslant 5$. At 10^{22} Wcm^{-2}, for example, stochastic radiation reaction predicts a yield of 0.023 photons per electron with $\hbar\omega \geqslant 500$ MeV (4.8× more than would be expected classically). As wakefield-accelerated electron beams typically have charges of 100 pC, i.e. $N_e \sim 10^9$, a collision at this intensity could generate up to 4×10^{10} gamma rays, 2×10^7 of which would have energies exceeding 500 MeV. The latter photons are strongly beamed in the forward direction, into a cone with opening half angle $\sim a_0/\gamma_0$; if the strong-field region in which they are generated has size ~ 1 μm, the peak brilliance is then $\sim 5 \times 10^{22}$ s^{-1}mm^{-2}mrad^{-2}.

This enhancement can be seen in more detail in fig. 34, which shows the tail distribution of the photon spectrum for GeV electrons colliding with laser pulses of intensity 10^{21} and 10^{22} Wcm^{-2}, i.e.

$$N_\gamma(\hbar\omega > \mathcal{E}) = \int_{\mathcal{E}}^{\gamma mc^2} \frac{dN_\gamma}{d\omega} \, \mathrm{d}\omega. \tag{4.2.5}$$

We can see that the factor by which the stochastic spectrum is increased over the classical spectrum (the 'multiplier') grows non-linearly with the minimum energy $\mathcal{E}$, reaching two orders of magnitude if $\mathcal{E} \sim$ 700 MeV. The origin of this enhancement is the increase in the max-

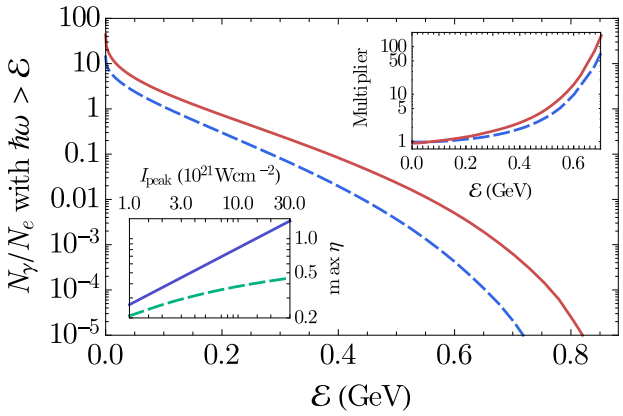

Figure 34: The number of photons with energy greater than $\mathcal{E}$ emitted by a 1 GeV electron incident on a linearly polarised, plane wave laser pulse that has Gaussian temporal profile (FWHM 30 fs) and peak intensity (blue, dashed) 10^{21} and (red) 10^{22} Wcm^{-2}. (upper inset) The factor by which the plotted gamma ray spectrum is multiplied in going from continuous to stochastic radiation reaction. (lower inset) The maximum η of the electron when radiating (green, dashed) continuously and (purple) stochastically. (Adapted from Blackburn et al. [20].)

imum η reached by the electron, which is shown in the lower inset of fig. 34. For stochastic radiation, $\eta_{\rm max} \sim I_{21}^{1/2}$ as there will always be some electrons that do not radiate until they reach the centre of the laser pulse; for classical radiation, the scaling is much weaker as the electron must always lose energy in the foot of the pulse. The detection of the highest energy gamma rays is then a signature of quantum radiation reaction, as these can only be generated stochastically.

However, we must allow for the fact that in reality, both the laser pulse and electron beam will have temporal and spatial structure and so not all the electrons will be incident on the region of highest intensity. Let us now consider a beam of 1 GeV electrons, uniformly distributed around the optical axis in a disk of radius 10 μm, colliding with a laser pulse that has Gaussian temporal and radial profiles (FWHM 30 fs and waist size 2.2 μm). If the pulse has a peak intensity of 10^{22} Wcm^{-2}, this collision will produce 7.40×10^{-4} (1.32×10^{-5}) photons per electron with $\hbar\omega \geqslant 500$ (700) MeV, 4.3× (160×) greater than that which would be radiated classically.

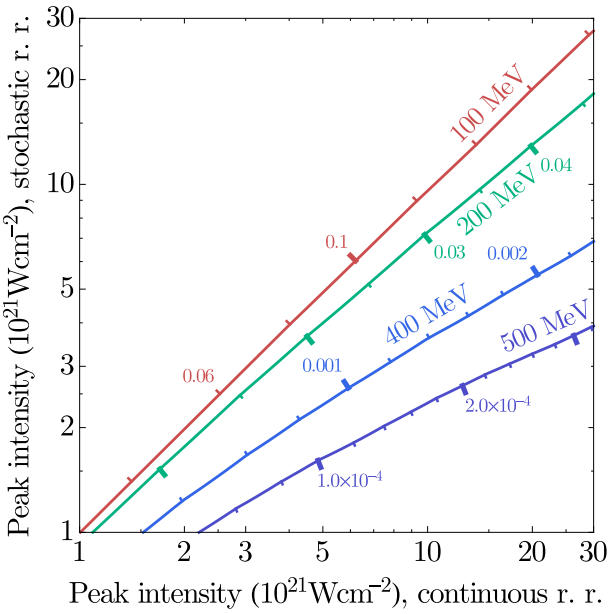

Figure 35: The number of photons per electron with energy greater than (red) 100, (green) 200, (blue) 400 and (purple) 500 MeV radiated by a 1 GeV electron beam (uniformly distributed in a disk of radius 10 μm around the optical axis) that has collided with a focused laser pulse with given peak intensity and Gaussian temporal and radial profiles (FWHM 30 fs and waist size 2.2 μm) if radiation is treated (horizontal axis) continuously or (vertical axis) stochastically. (From Blackburn et al. [20].)

While these yields are much smaller than in the plane wave case, it is still possible to distinguish stochastic radiation reaction by measuring the high-energy tail of the photon spectrum, as the production of these gamma rays is most enhanced by straggling. Figure 35 compares the intensity of laser pulse necessary to produce a given yield of photons if the electrons radiate continuously or stochastically. We find that the laser pulse must be more intense for a classical interaction to produce the same yield as a stochastic interaction.

The stochastic nature, or otherwise, of a laser–electron-beam collision can then be determined by fitting the gamma ray spectrum to the points shown in fig. 35. For example, the detection of 9.0×10^{-2} photons per electron with $\hbar\omega \geqslant 100$ MeV would be consistent with both a continuously and stochastically radiating electron beam and a laser pulse of peak intensity 5×10^{21} Wcm^{-2}. If however that collision were also measured to produce 1.9×10^{-3} photons per electron with $\hbar\omega \geqslant 400$ MeV, then this could only be consistent with stochastic radiation reaction, as a continuously radiating beam would have had to collide with a pulse of peak intensity 1.8×10^{22} Wcm^{-2} to produce that number of gamma rays. Were the number of photons with $\hbar\omega \geqslant 500$ MeV measured instead, then the equivalent intensity would rise to 5.2×10^{22} Wcm^{-2}, an order of magnitude greater than is needed by stochastic radiation.

It is the sensitivity of the tail of the gamma ray yield to the laser intensity that will make it possible to overcome the experimental uncertainty in that intensity and demonstrate the stochastic nature of photon emission.

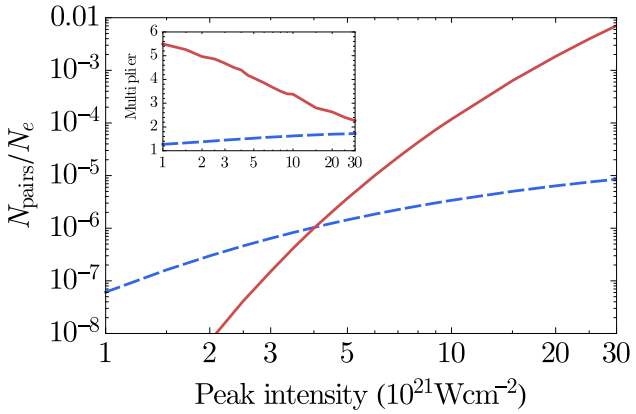

Figure 36: The number of (red) Breit-Wheeler and (blue, dashed) trident e^+e^- pairs produced by a 1 GeV electron incident on a linearly polarised, plane wave laser pulse that has Gaussian temporal profile (FWHM 30 fs) and given peak intensity (using the Weizsäcker-Williams approximation to the trident rate). (inset) The factor by which the pair yields are multiplied in going from continuous to discontinuous radiation. (Adapted from Blackburn et al. [20].)

4.2.2 *To the pair yields*

It is probable that some of these high-energy gamma rays will decay into electron-positron pairs in the strong field of the laser, undergoing the Breit-Wheeler process. Pairs can also be produced directly by the electron in the trident process, where the mediating photon is virtual. Plotted in fig. 36 are the number of pairs produced per electron by a monoenergetic 1 GeV beam incident on a plane wave laser pulse with given peak intensity. The trident rate used was calculated with the Weizsäcker-Williams approximation described in section 3.5.4 (i.e. with (3.5.7)).

The trident process is dominant for lower intensities, because the synchrotron photons produced have low energy and propagate in a small electric field [16]. Increasing the intensity therefore raises the Breit-Wheeler rate for two reasons: more, higher energy photons are radiated; and these photons each have a greater probability to pair-produce. The dominant effect is the latter. The scalings found in section 4.2.1 suggest that a factor of 2 increase in intensity (from $I_{21} = 5$ to 10) leads only to

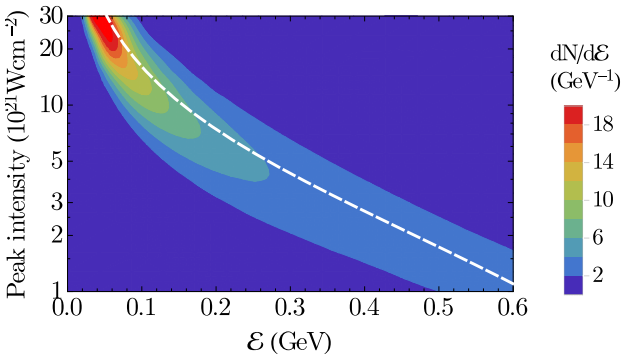

Figure 37: The energy distribution $\mathrm{d}N/\mathrm{d}\mathcal{E}$ of a 1 GeV electron that has collided with a plane-wave laser pulse with given peak intensity and Gaussian temporal profile (FWHM 30 fs). (white, dashed) The energy to which a classically radiating electron would fall.

a factor of 1.34 increase in the number of photons with energy greater than 500 MeV. However, 30× the number of Breit-Wheeler pairs are produced; a 1 GeV electron beam will produce 1.2×10^{-4} pairs per electron if the laser intensity exceeds 10^{22} Wcm^{-2}. This is because there is rapid increase in the Breit-Wheeler pair production rate for $\chi \gtrsim 0.2$ (see fig. 25), which parameter regime can be reached with current high-intensity lasers and photons with $\hbar\omega > 500$ MeV. Doing so is sensitive to the yield of near-GeV photons; as this is increased by straggling, we find the yield of pairs is also increased (see inset of fig. 36).

However, the pair yields are small enough that any depletion of the gamma ray spectrum, or production of secondary radiation, is negligible. The latter means that this experimental geometry is not capable of producing a pair cascade. Electrons counter-propagate into the laser and so decelerate; converting laser energy to pairs requires much more intense, counter-propagating laser beams that can accelerate the electron up to high energy between emission events, as discussed by Nerush et al. [18], Duclous et al. [17].

4.2.3 *To the electron beam*

It is also possible to use the final energy spectrum of the electron beam as evidence that straggling has taken place. Figure 37 shows the final energy spectrum for an initially mono-energetic beam with $\gamma_0 = 2000$ colliding with a plane-wave laser pulse of given peak intensity; at the current intensity frontier of 2×10^{22} Wcm^{-2}, it is clear that the electron can lose almost all its energy to gamma rays. Furthermore, the probabilistic nature of the emission process manifests itself in the broadening of the energy spectrum (see fig. 33), as some electrons lose more energy than would be predicted classically, and some lose less.

Neitz and Di Piazza [19] showed that the energy spread of an electron beam would narrow were that beam subject to classical radiation reaction, but would broaden if it were subject to quantum radiation reaction. This is because the Landau-Lifshitz force (4.2.1) $\sim \eta^2 \sim \gamma^2$; consequently, more energetic electrons lose energy faster than their lower energy counterparts. However, measuring that broadening, and so confirming that stochastic radiation reaction has taken place, requires that the electron beam be free of a low-energy tail, have well-defined, large initial energy and be reproducible from shot to shot. This could be accomplished using a conventional RF accelerator [75], or by magnetically filtering the beam produced by a laser-driven wakefield and gathering statistics over a large number of shots.

However, we must account for the fact that as both the electron beam and laser pulse will have radial structure, electrons will counter-propagate with a range of displacements from the optical axis and experience different peak laser intensities. This would lead to broadening of the energy spectrum of a mono-energetic beam even with continuous radiation reaction. Nevertheless, as the energy loss of a classical electron is deterministic, there will be a non-zero lower bound to the classical

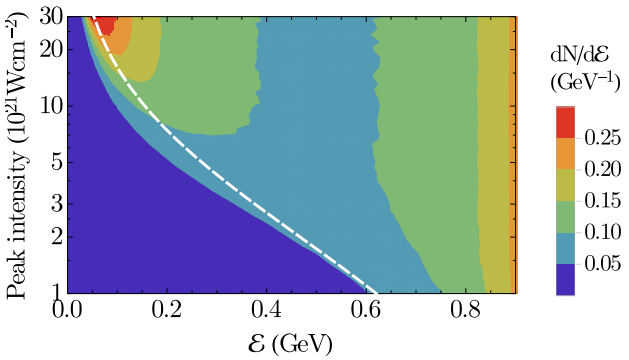

Figure 38: The energy distribution $\mathrm{d}N/\mathrm{d}\mathcal{E}$ of a 1 GeV electron beam (uniformly distributed in a disk of radius 10 μm around the optical axis) that has collided with a focused laser pulse with given peak intensity and Gaussian temporal and radial profiles (FWHM 30 fs and waist size 2.2 μm). (white, dashed) The lower bound on the energy distribution of an electron beam that radiates continuously. (Adapted from Blackburn et al. [20].)

final state energy distribution, corresponding to those electrons which have passed through the region of highest laser intensity. This is shown in fig. 38, which compares the spectra for mono-energetic GeV electron beams that are uniformly distributed around the optical axis in a disk of radius 10 μm. The fraction of the beam that straggles and loses more energy than possible classically $\simeq 7.3\times10^{-3}/(1+0.030I_{21}^{0.81})$; at 2×10^{22} Wcm^{-2}, 0.55% of the beam will experience an energy loss exceeding 940 MeV, the maximum possible classically.

4.3 MEASURING QUANTUM RADIATION REACTION

In section 4.2, we considered the collision of a GeV electron beam with a laser pulse of intensity 10^{21} to 3×10^{22} Wcm^{-2}; the beams collided at an angle of 180° and were timed to coincide perfectly at the laser focus. Quantum radiation reaction could be experimentally diagnosed by measuring the large yield of gamma rays or the reduced energy of the electron beam after the collision.

Both these signatures are sensitive to the overlap between the electron beam and laser pulse, which places constraints on the accuracy of

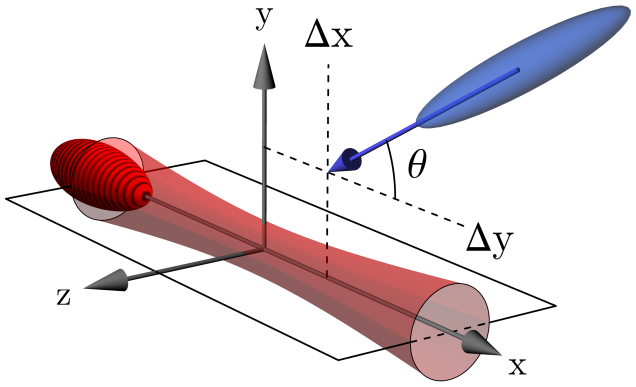

Figure 39: The experimental configuration under consideration: (blue) a GeV electron beam colliding with (red) an laser pulse of intensity 10^{22} Wcm^{-2}. The laser moves in the positive x-direction; the electron beam centre is located in, and the electrons' initial momenta are parallel to, the x-y plane. Observing radiation reaction will depend upon the degree to which the beams overlap, i.e. the collision timing and angle θ. The timing error is parametrised by $(\Delta x, \Delta y)$, the location of the electron beam centre at $t = 0$, when the laser pulse is focused at the origin. We do not consider the effects of a displacement between the beams in the z-direction.

collision timing required. In this section we will consider how the collision timing, and the angle between the beams, affects the total gamma ray energy, the electron beam's final energy spectrum and therefore the viability of diagnosing quantum radiation reaction in an experiment using today's high intensity laser facilities.

A schematic of the experimental configuration under consideration is given in fig. 39. We consider varying the angle of collision θ as well as the mistiming in the x-y plane. This is parametrised by the offsets $(\Delta x, \Delta y)$, which correspond to the displacement of the electron beam centre from the origin at $t = 0$, at which time the laser is focused there.

The laser is a Gaussian focused beam (in the paraxial approximation) with waist $w_0 = 2$ μm and wavelength $\lambda = 0.8$ μm, linearly polarised along the y axis and propagating towards $+x$. It has a Gaussian temporal intensity profile with maximum $I = 10^{22}$ Wcm^{-2} ($a_0 = 65$) and

full length at half maximum $f = c \cdot 30$ fs $= 9$ μm. The fields at position (x, y, z) are

$$E_y = E_0 \frac{w_0}{w(x)} \exp\left(-\frac{y^2+z^2}{w(x)^2} - \frac{2\ln 2\,\phi^2}{k^2 f^2}\right) \sin\phi \tag{4.3.1}$$

$$B_z = E_y/c \tag{4.3.2}$$

where the phase of the wave is

$$\phi = kx - \omega t + \frac{kx(y^2+z^2)}{x^2 + x_\mathrm{R}^2} - \tan^{-1}\left(\frac{x}{x_\mathrm{R}}\right) \tag{4.3.3}$$

and the beam radius is

$$w(x) = w_0 \left[1 + \left(\frac{x}{x_\mathrm{R}}\right)^2\right]^{1/2}. \tag{4.3.4}$$

The Rayleigh range $x_\mathrm{R} = \pi w_0^2/\lambda$, the wavevector $k = 2\pi/\lambda$ and the angular frequency $\omega = ck$. The peak field E_0 is related to the laser intensity by $I = \frac{1}{2} c\epsilon_0 E_0^2$.

η, which controls photon emission, does not depend on the polarisation of the EM field, but only on the angle between the optical axis and the electron momentum θ. As such, the choice of polarisation here is arbitrary except that it defines the plane in which the electrons oscillate and so affects the angular distribution of radiation. This will be a fan of opening angle $\sim a_0/\gamma$ oriented along the polarisation axis [20].

4.3.1 *With a single electron*

To begin, let us consider a single electron (by which we mean a beam where all electrons have the same position, momentum and $\Delta x, \Delta y, \theta$). As photon emission is a stochastic process, we will consider the *mean* energy loss to gamma rays; to see the dependence of the gamma yield

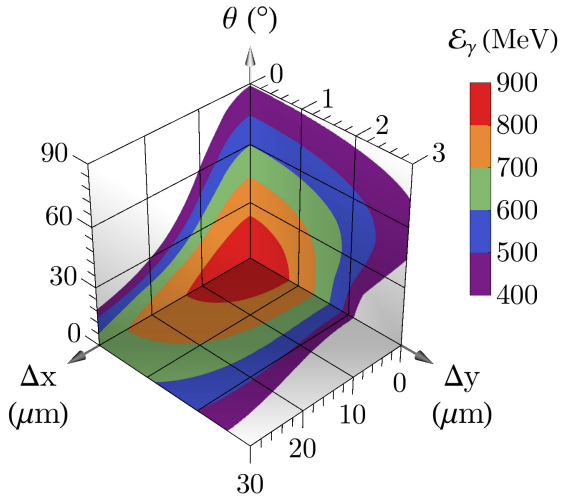

Figure 40: The mean energy $\mathcal{E}_\gamma$ radiated to photons of all energies by a single GeV electron colliding with a Gaussian laser pulse of intensity 10^{22} Wcm^{-2}. That loss is a function of $(\Delta x, \Delta y, \theta)$ and is calculated over the three planes where one of those parameters is zero.

on beam timing and angle of collision, we vary $(\Delta x, \Delta y, \theta)$, keeping the electron and laser pulse parameters the same.

Figure 40 shows the mean energy emitted in gamma rays by a GeV electron colliding with a laser pulse of intensity 10^{22} Wcm^{-2}. We see that the electron can lose a substantial fraction of its initial energy in the interaction, with a maximal loss of 845 MeV for the 'perfect' collision $\Delta x = \Delta y = \theta = 0$.

The gamma ray yield is much more sensitive to the perpendicular displacement between the beams Δy than the parallel displacement Δx. This is because the peak intensity the electron encounters falls as $\exp(-2(\Delta y/w_0)^2)$ for increasing Δy but as $[1 + (\Delta x/x_\mathrm{R})^2]^{-1}$ for increasing Δx; to reduce the peak intensity by a half requires $\Delta x = 16$ μm but only $\Delta y = 1.4$ μm. The shape of the contours in the $\Delta x - \Delta y$ plane in fig. 40 shows that this is somewhat ameliorated by the fact that the pulse becomes wider with divergence angle of 15°, so for larger parallel displacements the gamma yield is more tolerant of perpendicular displacements.

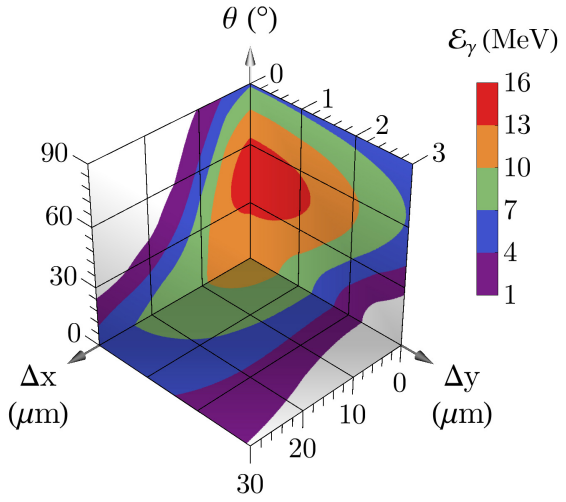

Figure 41: The mean energy $\mathcal{E}_\gamma$ radiated to photons with $\hbar\omega > 500$ MeV by a single GeV electron colliding with a Gaussian laser pulse of intensity 10^{22} Wcm^{-2}.

Given a displacement Δx, we can see that increasing the angle of collision θ always reduces the energy loss, as the parameter that controls the importance of radiation reaction $\eta \propto (1 + \cos\theta)$.

This is generally true as well if instead the electrons are displaced perpendicularly to the laser focus. However, for $\Delta y \gtrsim 1.5\ \mu$m, increasing θ can increase the gamma ray yield, as the electron beam then crosses the optical axis a shorter distance downstream of the laser pulse. As the intensity experienced is then higher, this goes some way to countering the effect of the geometric factor $(1 + \cos\theta)$ in η.

We saw in section 4.2.1 that measuring the yield of the highest energy photons can allow the distinguishing of quantum and classical radiation reaction. Accordingly, we measured the simulated yield of gamma rays with energies greater than 500 MeV; the mean total of this yield per electron, is plotted in fig. 41. Unlike the total gamma ray yield, peak generation does not occur when the beams are perfectly counter-propagating, but rather when $\theta \simeq 45°$.

As it contains a geometric factor $(1 + \cos\theta)$, the η of such an electron will be about 18% smaller than that for counter-propagation. This will

have two effects: the electron will emit photons at a lower rate; and overall those photons will have lower energies, as the tail of the synchrotron spectrum grows non-linearly with increasing η. These should act to reduce the yield of high energy photons. However, the laser pulse is much longer along the propagation axis than it is wide, so electrons traversing it at an angle interact with field over a shorter distance and are more likely to reach the high-intensity region.

To see the interplay of these three factors, we will determine the probability distribution of ϕ_1, the phase of the laser pulse at which the electron emits its first photon. This will be controlled by the emission rate and the effective length of the laser pulse, both of which depend upon the angle of collision. The η reached by the electron at this point will then determine the energy spectrum of the emitted photons. We will compare any analytical results with our simulations, taking $\Delta x = \Delta y = 0$.

Recalling that

$$\eta = \frac{\gamma \left|\mathbf{E}_\perp + \mathbf{v} \times \mathbf{B}\right|}{E_{\text{Sch}}} = \frac{\gamma(1+\cos\theta)\left|\mathbf{E}\right|}{E_{\text{Sch}}} \tag{4.3.5}$$

for an ultrarelativistic electron propagating at angle θ to a linearly polarised electromagnetic wave, the rate of change of optical depth against emission is

$$\frac{\mathrm{d}\tau}{\mathrm{d}t} = \frac{\sqrt{3}\alpha}{2\pi\tau_{\text{c}}}\frac{\eta}{\gamma}h(\eta) = \frac{\sqrt{3}\alpha}{2\pi\tau_{\text{c}}}(1+\cos\theta)\frac{|E(t)|}{E_{\text{Sch}}}h(\eta). \tag{4.3.6}$$

The first approximation we will make is that $h(\eta) \simeq h(0) = 5\pi/3$ at all times along the electron trajectory. We can justify this as in the foot of the pulse, the electric field is sufficiently small to keep $\eta \lesssim 0.1$. Even then, $h(0.1) = 0.93\,h(0)$ so any overestimate of the rate will be negligible.

In our simulations, $\mathcal{E}_0 = 1000$ MeV and therefore the electron can be treated as ultrarelativistic. Therefore its initial momentum is $\mathbf{p}_0 = -\mathcal{E}_0/c\,(\cos\theta, \sin\theta, 0)$. As $\gamma_0 = \mathcal{E}_0/m_e \gg a_0$, we can also assume that any deflection of the electron by the laser pulse is minimal. Its trajectory before emission is linear, with position at time t given by $(x, y, z) = -ct(\cos\theta, \sin\theta, 0)$. As (4.3.6) depends on the electron energy only through $h(\eta)$, which we approximate as constant, our result will depend on $\mathcal{E}_0$ only in the sense that it must be sufficiently large that the electron be ultrarelativistic.

In our simulations we use the full form of the Gaussian beam. However, for simplicity in our analytical calculations, we will neglect wavefront curvature, the Gouy shift and the spreading of the beam, so

$$E = E_0 \sin\phi \, \exp\left(-\frac{y^2+z^2}{w_0^2} - \frac{2\ln 2\,\phi^2}{k^2 f^2}\right) \tag{4.3.7}$$

$$\phi = kx - \omega t = -(1+\cos\theta)\omega t. \tag{4.3.8}$$

Using (4.3.8) to recast (4.3.6) and (4.3.7) in terms of ϕ, we find

$$\frac{\mathrm{d}\tau}{\mathrm{d}\phi} = -\frac{5\alpha}{2\sqrt{3}\omega\tau_\mathrm{c}} \frac{E_0}{E_\mathrm{Sch}} |\sin\phi| \, \exp\left(-\zeta^2\phi^2\right) \tag{4.3.9}$$

where

$$\zeta^2 = \frac{\sin^2\theta}{(1+\cos\theta)^2 k^2 w_0^2} + \frac{2\ln 2}{k^2 f^2}. \tag{4.3.10}$$

As the envelope in (4.3.9) varies slowly with ϕ, we can approximate $|\sin\phi| \simeq 2/\pi$ and thus integrate (4.3.9) from ∞ to ϕ_1. We find the following relation between the final optical depth and the phase at which the electron emits its first photon:

$$\tau_\mathrm{f} \simeq \frac{5\alpha}{2\sqrt{3\pi}\omega\tau_\mathrm{c}} \frac{E_0}{E_\mathrm{Sch}} \frac{1-\mathrm{erf}\,(\zeta\phi_1)}{\zeta}. \tag{4.3.11}$$

Photon emission is a stochastic process and governed by Poisson statistics, so these final optical depths are distributed as $\tau_\mathrm{f} \sim \exp(-\tau_\mathrm{f})$.

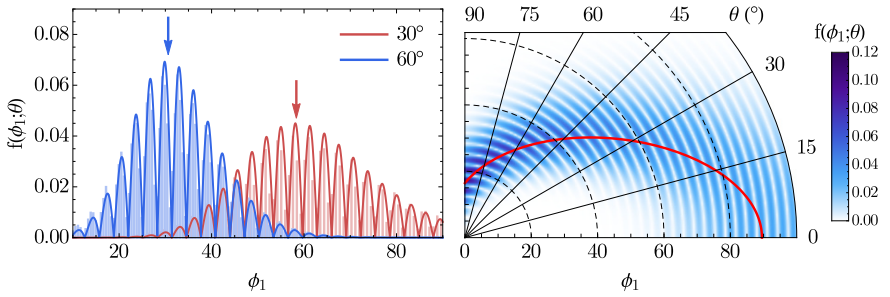

Figure 42: (left) The probability density that an electron colliding with Gaussian laser pulse of intensity 10^{22} Wcm^{-2} at θ = (red) 30° and (blue) 60° emits its first photon at wave phase ϕ_1. The curves are calculated using (4.3.12) and the vertical bars give the distribution found in simulations. The arrows indicate the value of $\phi_{1,\mathrm{peak}}$ given by (4.3.13). (right) Density plot of $f(\phi_1;\theta)$: the red line is $\phi_{1,\mathrm{peak}}$.

Then the probability density that an electron colliding with a Gaussian laser pulse at angle θ emits its first photon at phase ϕ_1 is given by

$$f(\phi_1;\theta) = \exp(-\tau_\mathrm{f}) \left| \frac{\mathrm{d}\tau_\mathrm{f}}{\mathrm{d}\phi} \right| \tag{4.3.12}$$

where we substitute (4.3.11) in the exponent and (4.3.9) in the modulus. Figure 42 compares our analytical $f(\phi_1;\theta)$ with that obtained from simulation and finds good agreement.

It is evident from fig. 42 that at larger angles of collision, the electron is more likely to penetrate further into the laser pulse before emitting its first photon; both the peak and the width of the distribution decrease as θ grows, reducing the length of interaction. The peak $\phi_{1,\mathrm{peak}}$ can be estimated by solving $\mathrm{d}f(\phi_1;\theta)/\mathrm{d}\phi_1 = 0$, using (4.3.11), to find

$$\phi_{1,\mathrm{peak}}^2 \simeq \frac{1}{2\zeta^2}\, W\left[\frac{1}{\zeta^2} \left(\frac{5\alpha}{\sqrt{6}\pi} \frac{1}{\omega\tau_\mathrm{c}} \frac{E_0}{E_\mathrm{Sch}} \right)^2 \right] \tag{4.3.13}$$

where $W(x)$ is the Lambert W function, defined by $x = W(x)e^{W(x)}$, and ζ^2 is as given in (4.3.10).

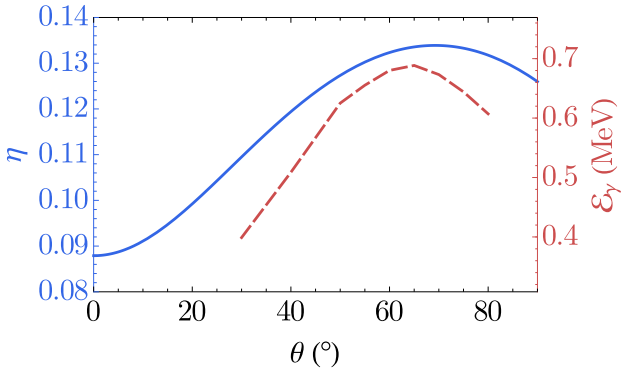

Figure 43: (blue) The typical η of an electron with $\mathcal{E}_0 = 1000$ MeV emitting its first photon; (red, dashed) the energy lost at first emission to photons with $\hbar\omega > 500$ MeV from simulations.

We can use $\phi_{1,\text{peak}}$ to find the typical η that an electron propagating at angle θ reaches when emitting its first photon

$$\eta \simeq \frac{\gamma_0(1+\cos\theta)E_0}{E_{\text{Sch}}} \exp(-\zeta^2\phi_{1,\text{peak}}^2) \tag{4.3.14}$$

which is plotted in fig. 43. First, we can justify approximating $h(\eta) = h(0)$ as $\eta \simeq 0.1$ at first emission over the whole range of θ. We also find that the largest η is reached for approximately 70°. Given that maximising the geometric factor $(1+\cos\theta)$ in η requires $\theta = 0°$, and minimising the length of interaction $\theta = 90°$, we can see that, at least for the first emission, the latter dominates. As the high energy tail of the emitted photon spectrum is sensitive to increasing η, we find as expected that this peak is also well correlated to the θ which maximises the energy lost to photons with $\hbar\omega > 500$ MeV at first emission.

However, fig. 41 shows that once the whole interaction with the pulse is taken into account, the yield of high energy photons is maximised for $\theta \simeq 45°$. This is because as the electron continues into the centre of the laser pulse, emission becomes much more frequent. This is most important for smaller angles of collision: while the rate of emission scales as η, the radiated power scales as η^2; when squared, the geometric factor $(1+\cos\theta)$ more strongly favours counter-propagation and reduces the

advantage of a shorter length of interaction. Our simulations show that energy lost to >500 MeV photons peaks for an initial angle of 65° after one emission, 55° after five and then 45° after the complete interaction. Nevertheless it is reasonable to conclude that for a single electron, reducing the length of interaction and so the energy loss in the foot of the pulse is the most important factor in maximising the yield of the highest energy gamma rays.

4.3.2 *With an electron beam*

We now consider the interaction of an intense laser pulse with a GeV electron beam, rather than a single electron, with these parameters: the Lorentz factors of the electrons in the beam are normally distributed, with mean $\gamma_0 = 1957$ and $\sigma = 60$, i.e. an initial energy of $\mathcal{E}_0 = 1000$ MeV and spread of 3%. In a real electron beam, there would be a small angular divergence of order mrad, but here their initial momenta are directed along $\hat{\mathbf{p}}_0 = -(\cos\theta, \sin\theta, 0)$. The charge density of the beam forms a Gaussian envelope with $\sigma_\parallel = 15$ μm and $\sigma_\perp = 2$ μm, where the widths are given in the directions parallel and perpendicular to $\hat{\mathbf{p}}_0$ respectively. We neglect the space charge field, following section 2.6.2, and also collective radiation effects, as the typical separation between electrons $(\sigma_\parallel \sigma_\perp^2 e/Q)^{1/3} \simeq 5$ nm, which is equivalent to 40 eV.

4.3.2.1 *Via the gamma ray spectrum*

Figure 44 shows the energy lost by such an electron beam to gamma rays when colliding with the specified laser pulse. As before, to see the dependence of the gamma ray yield on beam timing and angle of collision, we vary $(\Delta x, \Delta y, \theta)$, keeping the electron beam and laser pulse the same.

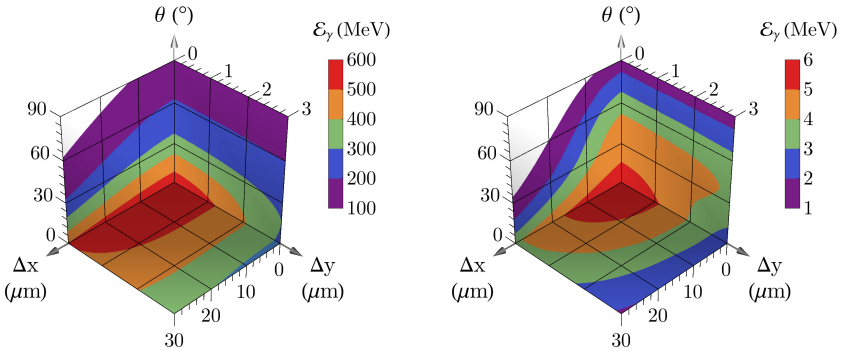

Figure 44: The energy radiated by a GeV electron beam, per electron, $\mathcal{E}_\gamma$ to (left) photons of all energies and to (right) photons with $\hbar\omega > 500$ MeV, when colliding with a Gaussian laser pulse of intensity 10^{22} Wcm^{-2}. That loss is a function of $(\Delta x, \Delta y, \theta)$ and is calculated over the three planes where one of those parameters is zero.

Unlike the single electron case, we find that both the total loss, and the loss to high energy photons, are maximised for $\Delta x = \Delta y = \theta = 0$. The maximal total loss is 560 MeV per electron (0.056 mJ for a beam with charge 100 pC); the maximal loss to > 500 MeV photons is 5.6 MeV (0.56 nJ for a beam).

Our previous analysis indicated that the yield of high energy photons is most sensitive to the distance the electrons must travel in the foot of the pulse; for $\Delta x = \Delta y = 0$, a collision at 65° maximises the gamma ray yield by balancing the shorter length of interaction against the geometric reduction in η. Here however, we must include the fact that when colliding at an angle, there is reduced overlap between the electron beam and laser pulse and so fewer electrons can straggle to reach the highest intensity fields.

We can estimate the overlap between the beams by evaluating

$$\Omega = \int \mathrm{d}t \int \mathrm{d}^3\mathbf{r}\, \rho(\mathbf{r}, t)|E(\mathbf{r}, t)| \tag{4.3.15}$$

where ρ is the beam charge density and $|E(\mathbf{r}, t)|$ is as given in (4.3.1), again taking $|\sin\phi| = 2/\pi$. We compare (4.3.15) with the total energy lost to photons in fig. 45, varying each of Δx, Δy and θ, and find it

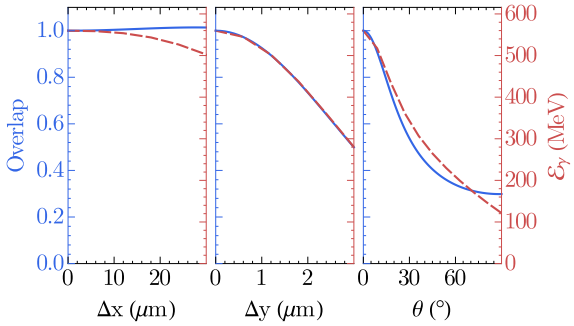

Figure 45: The (blue) overlap between the laser pulse and electron beam, normalised to the overlap at $\Delta x = \Delta y = \theta = 0$ and (red, dashed) the total loss of energy to photons per electron, varying from left to right: only Δx, only Δy and only θ.

models the dependence on Δy well. (4.3.15) overestimates the total gamma ray energy per electron for varying Δx: Ω increases with Δx for $\Delta x < 35$ μm, falling thereafter, because the laser pulse defocuses and becomes wider; however, even though more electrons collide with the pulse, each has a lower emission rate because the peak electric field encountered decreases as $[1 + (\Delta x/x_\mathrm{R})^2]^{-1}$. This is unimportant for varying Δy because for $\Delta y < 3$ μm, some of the electron beam always encounters the laser focus at $t = 0$. For varying θ, we see that overlap is much more significant a factor than both the shorter length of interaction and the geometric reduction in η.

Maximising the yield of photons in an experiment would therefore demand counter-propagation of the electron beam and laser pulse. However, in this setup the continuing pulses and electron beam could cause downstream damage to laser chains, particularly the focusing optics. In fig. 46, we consider a collision angle of 30° and plot the phase-space regions in which the total energy emitted in gamma rays is at least half of that obtained for $\Delta x = \Delta y = \theta = 0$. Comparing these to the contours in the Δx-Δy planes of fig. 44, it can be seen that these regions 'rotate' away from the Δx axis as the angle of collision increases, favouring a larger perpendicular offset.

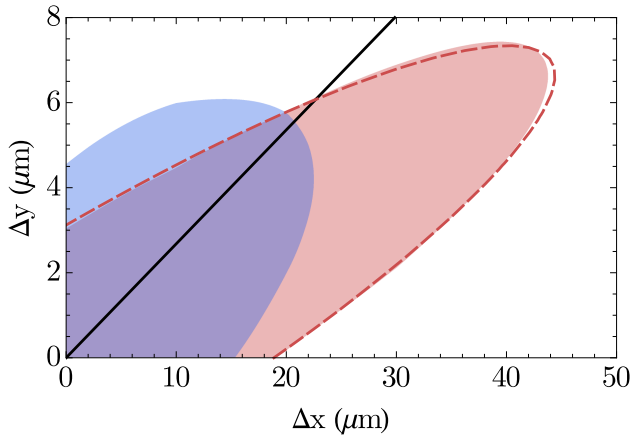

Figure 46: For a GeV electron beam colliding with a 10^{22} Wcm^{-2}, 30 fs laser pulse at an angle of 30°, the phase-space regions in which (red) the total energy radiated to photons is at least 280 MeV per electron and (blue) the total energy radiated to >500 MeV photons is at least 2.8 MeV per electron. In both cases this represents at least half the energy produced by a perfectly-timed, head-on collision. The lines are: (black) an analytical fit to the boundary of the red region as given in (4.3.17); (black, dashed) the combination of Δx and Δy required for the laser pulse peak and electron beam centre to coincide.

This can be explained in terms of the overlap between the beams. A non-zero Δx and θ mean that the electron beam crosses the optical axis ahead of the laser pulse at $t = 0$; the advancing laser pulse then interacts only with the tail of the passing electron beam. The distance of closest approach between the laser pulse and the beam centre is given by

$$\Delta_{\min} = \Delta y \cos\frac{\theta}{2} - \Delta x \sin\frac{\theta}{2}. \tag{4.3.16}$$

$\Delta_{\min} = 0$ implies $\Delta y = \Delta x \tan(\theta/2)$ and so with increasing θ the optimal perpendicular displacement does indeed 'rotate' away from $\Delta y = 0$. Figure 46 shows that this condition closely predicts the displacements required to maximise the yield of >500 MeV gamma rays, as that yield is sensitive to the number of electrons that encounter the region of highest laser intensity.

Fitting an ellipse to the boundary of the red region in fig. 46, the total energy emitted in gamma rays will be at least half that of a perfectly-

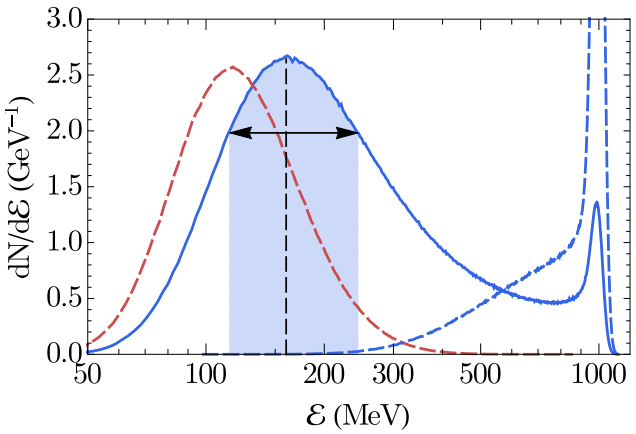

Figure 47: The energy spectrum of a GeV electron beam after colliding with a 10^{22} Wcm^{-2}, 30 fs laser pulse at an angle of (blue, solid) 0° and (blue, dashed) 90°; and (red, dashed) the energy spectrum of a single GeV electron after colliding with the same pulse at 0°, scaled by a factor of 0.3. Illustrated are the three signatures of a well-defined lower peak: (black, dashed) its energy, (black, arrowed) its width at 75% of maximum and (blue, shaded) the number of electrons within it.

timed, head-on collision if the parallel and perpendicular displacements satisfy:

$$\left(\frac{\Delta x}{18.9\ \mu\text{m}}\right)^2 + \left(\frac{\Delta y}{3.12\ \mu\text{m}}\right)^2 - \frac{\Delta x \Delta y}{(5.71\ \mu\text{m})^2} \leqslant 1 \tag{4.3.17}$$

4.3.2.2 *Via the electron spectrum*

Detecting radiation reaction in an experiment could also be accomplished by comparing the energy spectrum of a wakefield-accelerated electron beam with and without the target short pulse, showing the reduced energy of the beam in the former case.

Neitz and Di Piazza [19] showed that with stochastic radiation reaction, the energy distribution of an electron beam interacting with a laser pulse would broaden, in contrast to the narrower distribution expected with classical radiation reaction. Figure 47 compares the final state energy distribution of the GeV electron beam to that of a single electron located at the beam centre, i.e. after both beam and electron

have undergone a collision with $\Delta x = \Delta y = \theta = 0$; we see that in both cases there is substantial broadening of the energy spectrum.

However, the overall energy loss is lower for an electron beam and, unlike the single electron case, the distribution is strongly bimodal. The peak at 160 MeV is formed by those electrons that have collided with the intense part of the laser pulse and consequently lost a substantial fraction of their energy to gamma rays; the peak at 1000 MeV is formed by those electrons that have missed the laser pulse entirely. The broad spread between these peaks is caused not only by the stochastic nature of emission (two electrons travelling along the same trajectory will not necessarily lose the same energy) but by the lower peak intensities encountered for larger distances of closest approach to the laser focus.

However, if we consider the final state energy distribution for a collision at 90°, we see that there is no lower peak. As both η and the overlap between the beams are smaller, most of the electrons lose little to no energy; radiation reaction manifests itself by 'smearing out' the initial energy distribution, creating a tail down to 300 MeV. It is unlikely that this tail could be distinguished from the low energy tail that is seen in even high quality laser wakefield-accelerated electron beams. A large, well-defined low energy peak would allow an experiment to claim a robust signature of radiation reaction.

We now consider electron energy spectra for various parallel and perpendicular offsets (Δx and Δy) and angles of collision θ. If there is a low energy peak, we measure its prominence with three markers, as illustrated in fig. 47: its modal energy, its width (at 75% of maximum) and the number of electrons in the peak (i.e. the integral of the distribution over the range given by the width). The dependence of these markers on Δx, Δy and θ is given in fig. 48.

The modal energy has its lowest value (160 MeV) for a head-on collision $\Delta x = \Delta y = \theta = 0$. The energy loss of an electron depends upon its

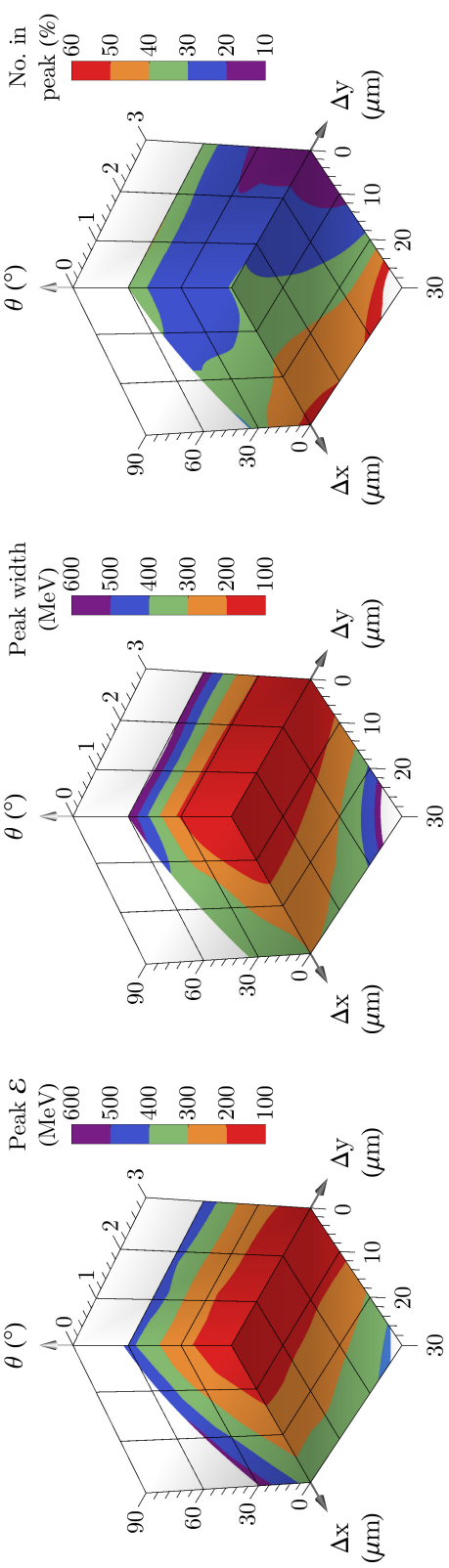

Figure 48: (left) The energy of the lower peak in the final state energy distribution $\mathrm{d}N/\mathrm{d}\mathcal{E}_{\mathrm{final}}$ of an electron beam (initial energy 1 GeV, spread 3%) that has collided with a 10^{22} Wcm^{-2}, 30 fs laser pulse, (centre) the full width of the peak at 75% of maximum and (right) the percentage of beam electrons in the peak, i.e. the integral of $\mathrm{d}N/\mathrm{d}\mathcal{E}_{\mathrm{final}}$ over the range defined by the peak width. Regions where a peak cannot be distinguished have been left blank.

radiated power and the length of time it spends in the laser pulse: the mean radiated power $\mathcal{P}(\eta) \propto \eta^2 g(\eta)$ (the factor $g(\eta) \in (0, 1]$ is a quantum correction [17]); the time it spends in the pulse depends upon the overlap between the beams. Both the power and the length of interaction fall with increasing Δx (the laser pulse diverges and loses intensity, lowering η) and θ (the geometric factor in η falls, as does the apparent length of the pulse).

The width is smallest (130 MeV) for a head-on collision as well. The stochastic nature of emission means that the energy spectrum of the beam broadens as it enters the laser pulse; however, as it loses energy, η falls and emission becomes less stochastic. As the mean radiated power $\propto \eta^2$, those electrons with higher energy radiate more than their lower energy counterparts and the spread begins to narrow. The longer, and more intense, the laser pulse, the smaller the peak width can become. Increasing Δx lowers the peak intensity the electrons encounter and increasing θ reduces the beams' length of interaction, preserving the initial broadening of the energy spectrum.

The peak position and width are essentially insensitive to Δy; however, increasing Δy from 0 to 3 μm does reduces the fraction of electrons within the peak from 31% to 15%. This is because the energy of the lower peak depends on the highest intensity the electron beam encounters: as Δy increases, this intensity maximum remains the same, but fewer electrons encounter it. The fraction in the peak increases with Δx because of the correlation between the lower peak's modal energy and its width; as the electrons encounter lower laser intensities, their final energy is higher, the peak width is larger and so the integral over that range captures more electrons.

Unsurprisingly, evidence of radiation reaction is strongest for counter-propagating beams. As discussed in section 4.3.2.1, the continuing laser pulses could cause downstream damage to the optical chains in such an

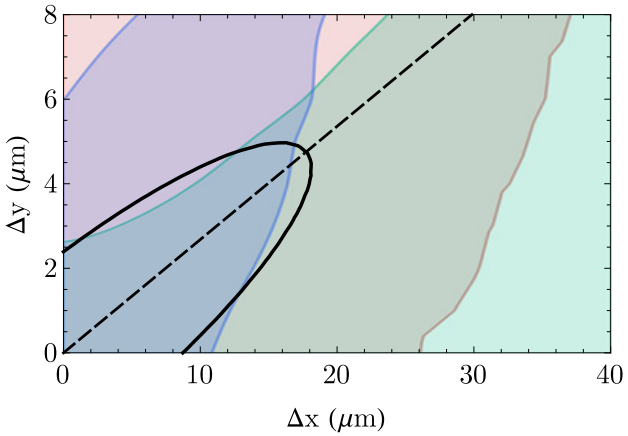

Figure 49: For a GeV electron beam colliding with a 10^{22} Wcm^{-2}, 30 fs laser pulse at an angle of 30°, the phase-space regions in which: (red) the energy of the lower peak < 500 MeV; (blue) the peak width < 250 MeV; and (green) the percentage of electrons in the peak $> 25\%$. The lines are: (black) an analytical fit to the region where all the above three overlap, as given in (4.3.18); (black, dashed) the combination of Δx and Δy required for the laser pulse peak and electron beam centre to coincide, as given in (4.3.16).

experiment. If instead we consider a collision that takes place at 30°, we can constrain Δx and Δy such that the lower peak is still distinguishable. For this to be case, it must be well separated in energy from the peak at 1000 MeV, narrow, and contain a substantial fraction of the beam electrons. Plotted in fig. 49 are the phase space regions in which the peak's modal energy < 500 MeV, its width < 250 MeV and the number of electrons $> 25\%$ of the beam total.

We can make the following analytical approximation to the boundary of the region where all three conditions are satisfied:

$$\left(\frac{\Delta x}{8.73\ \mu\text{m}}\right)^2 + \left(\frac{\Delta y}{2.40\ \mu\text{m}}\right)^2 - \frac{\Delta x \Delta y}{(3.46\ \mu\text{m})^2} \leqslant 1 \tag{4.3.18}$$

Note that beam overlap continues to be the dominant factor in determining the strength of radiation reaction, as the major axis of the ellipse (4.3.18) is collinear with the condition (4.3.16) that means the beam centres are at some point coincident.

4.4 CONCLUSION

In this chapter we have considered the colliding beams experimental geometry, using a fully stochastic model of radiation reaction and pair production. Under the chosen conditions, the quantum parameter for the energetic electron beam $\eta \simeq 0.1$ and QED effects such as the reduction in radiated power and straggling become important. The stochastic nature of emission enhances the yield of photons with $\hbar\omega > 700$ MeV by a factor of 160 over that predicted classically; the observation of these photons will be an unambiguous signal of that stochasticity.

The gamma ray yield and the energy loss of the electron beam are sensitive to both the maximal η reached by the electrons as well as the length over which this is sustained. However, for a realistic electron beam, the overlap between the beams will be a more significant factor in determining the strength of radiation reaction.

Maximising these should require the counter-propagation of the electron beam and laser pulse; this exploits the slow angular divergence of the laser pulse, minimising the accuracy of longitudinal timing required, and the geometric factor $(1 + \cos\theta)$ in η to enhance the high energy tail of the photon spectrum.

For a GeV electron beam colliding head-on with a 30 fs laser pulse of intensity 10^{22} Wcm^{-2}, the mean energy lost to gamma rays will be 560 MeV per electron. The electron beam's final energy spectrum will be bimodal, with a lower energy peak at 160 MeV (width 130 MeV) containing 31% of the beam. These maximal values are achieved for $\Delta x = \Delta y = \theta = 0$.

A head-on collision could be achieved using a focusing optic with an aperture, so that the decelerated electrons, gamma rays and any pairs do not cause downstream damage to the laser chain. However, this will lower the peak intensity as not all the energy is focused onto

the electron beam. If instead the angle of collision is 30°, the total energy emitted to gamma rays will be at least half its head-on value if the parallel and perpendicular offsets satisfy (4.3.17); the lower energy peak in the electron spectrum will be well-defined if (4.3.18) is satisfied, which is the stricter condition.

Obtaining a Δx and Δy that satisfy these accuracy requirements will rely on gathering statistics over a large series of laser shots. While the region in $\Delta x, \Delta y$ phase space is small, the energy converted to gamma rays is sufficiently large, and the resulting low energy peak in the electron spectrum sufficiently prominent, to be robust signatures of radiation reaction, with experimental parameters that can be achieved in current high intensity laser facilities.

5

CONCLUSION

5.1 SUMMARY

The purpose of this thesis is threefold: to justify the necessity of including radiation reaction and strong-field QED processes when considering laser-plasmas with $a_0 > 100$; to explain how such plasmas may be modelled; and to show that it is possible to probe the QED-plasma regime in an experiment that could be accomplished in today's high intensity laser plasmas.

In chapter 1, we saw that electrons subject to intense electromagnetic waves are rapidly accelerated to relativistic energies. That acceleration causes them to radiate and lose energy; for laser intensities $I > 10^{23}$ Wcm^{-2}, that loss amounts to more than half the electron's energy per laser period. The necessity of including the back-reaction of the radiation on the electron led us to a modified equation of motion called the Lorentz-Abraham-Dirac [4] equation (1.3.5). However, it possesses runaway solutions and other pathologies that arise from the difficulty of interpreting the self-force on a pointlike particle [6, 31].

A way forward was indicated by the fact that the magnitude of radiation losses is controlled by the quantum non-linearity parameter η, which measures the electric field strength in the rest frame of a particle against the critical field of QED E_{Sch} [16]. We asked whether treating the emission process quantum-mechanically would avoid the difficulties inherent in a classical treatment of radiation reaction. After all, that reaction must arise naturally in QED as the electromagnetic field is

quantised; when an electron scatters from a photon, the two-particle conservation of momentum sets the magnitude of the recoil [63].

Present lasers can easily reach $a_0 \sim 1$. In that intensity regime, the dominant QED process is non-linear Compton scattering: the inelastic scattering of an electron from many background photons [67]. As the photon density in an intense laser is high, the rate must be calculated using strong-field QED, which divides the electromagnetic field into a classical background and quantised radiation field [68]. If the background is a plane wave, it is possible to do so analytically [9, 71]. We saw in chapter 2 that as $a_0 > 1$, the number of non-linear orders that is accessible becomes very large, leading to the emission of photons with much more energy than would be expected with linear Compton scattering [83].

In a general laser-plasma interaction the EM fields have complex structure and it is not possible to derive QED rates analytically. However, the region over which the emission process takes place, the formation length, becomes very small as a_0 increases [9]. For $a_0 \gg 1$ the quasistatic approximation allows us to calculate those rates in an equivalent system of static fields that has the same η, which dramatically simplifies the analysis [84].

In chapter 3 we used this to set out how QED processes could be included in plasma physics. We reviewed in detail the two leading-order processes of synchrotron photon emission and Breit-Wheeler pair creation, as well as briefly discussing higher-order processes and spin effects. The average rate of energy loss to synchrotron photon emission matches that predicted classical radiation reaction for $\eta \ll 1$. For $\eta > 0.1$, however, quantum corrections to the spectrum reduce the electron emissivity and so classical radiation reaction greatly overestimates the energy loss.

Coupling QED rates to plasma physics can be achieved using particle-in-cell (PIC) codes, which simulate *ab initio* the self-consistent evolution of EM fields and particles. We outlined the Monte-Carlo algorithm of Duclous et al. [17] by which emission events can be included in the standard PIC loop, treating the gamma rays as particles rather than waves on the discretised grid. These QED-PIC codes have been used to model a variety of laser-plasma interactions for $I > 10^{23}$ Wcm^{-2} [11, 21, 18].

It is vital that this semi-classical approach to QED and the simulation codes are benchmarked against experimental results. However, the current intensity frontier, 10^{22} Wcm^{-2} [1], is not yet within the radiation-reaction or QED-dominated regimes. We saw that in chapter 4 that this could be overcome by accelerating the electrons to high energies before they encounter an intense laser pulse [75, 143]. The collision of a GeV electron beam and laser with $I > 10^{21}$ Wcm^{-2} leads to an $\eta \sim 1$ and so the electron motion will be dominated by quantum radiation reaction [20, 19]. The stochastic nature of photon emission leads to a phenomenon we call *straggling*, which enhances the emission of the highest energy photons. My simulations of these interactions show that it will be possible to distinguish quantum from classical radiation reaction by measuring the high-energy tail of the gamma ray spectrum. Experimental verification of this is entirely feasible using present-day high-power laser facilities.

While classical radiation reaction and strong-field QED are by no means new subject areas in physics, it is only recently that their effect on laser-plasma interactions has become of wide interest. That interest has been driven by the expectation that the next generation of high-power laser facilities will produce focused intensities exceeding 10^{23} Wcm^{-2} [2, 3]. These laser-plasmas will provide a means of studying extreme astrophysical environments [55] as well as the fundamental

structure of QED [10]. We have shown that the models used to simulate these plasmas may be verified in today's high-power laser facilities; doing so will justify the simulation and design of future high-intensity laser-plasma experiments.

5.2 OUTLOOK

The field of QED-plasma physics is still young and there remains work of a fundamental nature to be performed in the coming years. Much of this will occur at the interface between theoretical, computational and experimental physics. For example, the use of the quasistatic approximation in laser-plasma simulations has encouraged strong-field QED theorists to study processes in constant crossed fields to develop analytical benchmarks of our numerical methods [88, 85, 116].

It is important that as this field develops, it should be guided by experiment. There are now concrete proposals to perform laser-electron-beam collisions at $a_0 \gg 1$; an experiment that successfully observed stochastic radiation reaction or pair production in the highly non-linear regime would attract much interest from all sides of QED theory as well as computational and experimental plasma physics. That contact can guide the development of the next generation of high-intensity laser experiments.

Those experiments will almost certainly begin with laser irradiation of solid targets. Accordingly, the next step must be to develop a model of laser absorption in overdense plasmas when gamma ray production and pair creation are dynamically significant. This will naturally involve PIC simulation, but there is scope for analytical work; the ultimate goal would be to predict the absorption fraction for a given laser intensity. As QED processes change how the energy budget is distributed among

ions and electrons, this understanding is necessary for assessing high-intensity lasers as sources of energetic particle beams.

We should also continue by refining our computational models. This could involve studying higher-order QED processes, but at tree-level the first change would be to include spin and polarisation as a property of the computational particles in PIC simulations. Electrons would then precess as they propagate through the plasma fields, as well as experiencing a force due to the interaction between their magnetic moment and the external fields. We would look for geometries where the subsequent modifications to the gamma ray spectrum become important. For example, in lasers intense enough that a single particle can seed a pair cascade, we must model the initial state of that particle as precisely as possible, including any spin degrees of freedom.

[1] S.-W. Bahk, P. Rousseau, T. A. Planchon, V. Chvykov, G. Kalintchenko, A. Maksimchuk, G. A. Mourou, and V. Yanovsky. Generation and characterization of the highest laser intensities (10^{22} W/cm^2). *Opt. Lett.*, 29(24):2837–2839, Dec 2004. doi: 10.1364/OL.29.002837. URL http://ol.osa.org/abstract.cfm?URI=ol-29-24-2837. (Cited on pages 1, 21, 55, 92, and 130.)

[2] The Vulcan 10 PW Project. URL http://www.stfc.ac.uk/CLF/Facilities/Vulcan/14684.aspx. (Cited on pages 1, 23, and 130.)

[3] The Extreme Light Infrastructure (ELI) Project. URL http://www.eli-laser.eu/theeliproject.html. (Cited on pages 1, 23, 93, and 130.)

[4] P. A. M. Dirac. Classical theory of radiating electrons. *Proc. R. Soc. London Ser. A*, 167(929):148–169, 1938. ISSN 0080-4630. doi: 10.1098/rspa.1938.0124. URL http://rspa.royalsocietypublishing.org/content/167/929/148. (Cited on pages 1, 16, and 128.)

[5] T. Erber. The classical theories of radiation reaction. *Fortschr. Phys.*, 9(7):343–392, 1961. ISSN 1521-3979. doi: 10.1002/prop.19610090702. URL http://dx.doi.org/10.1002/prop.19610090702. (Cited on pages 1, 15, and 16.)

[6] D. A. Burton and A. Noble. Aspects of electromagnetic radiation reaction in strong fields. *Contemp. Phys.*, 55(2):110–121, 2014. doi: 10.1080/00107514.2014.886840. URL http://dx.doi.org/10.1080/00107514.2014.886840. (Cited on pages 1, 17, 18, 20, and 128.)

[7] W. H. Furry. On bound states and scattering in positron theory. *Physical Review*, 81:115–124, January 1951. doi: 10.1103/PhysRev.81.115. (Cited on pages 1 and 25.)

[8] L. S. Brown and T. W. Kibble. Interaction of intense laser beams with electrons. *Physical Review*, 133:705–719, February 1964. doi: 10.1103/PhysRev.133.A705. (Cited on page 1.)

[9] V. I. Ritus. Quantum effects of the interaction of elementary particles with an intense electromagnetic field. *J. Sov. Laser Res.*, 6(5):497–617, September 1985. ISSN 0270-2010. doi: 10.1007/BF01120220. URL http://dx.doi.org/10.1007/BF01120220. (Cited on pages 1, 28, 29, 30, 33, 49, 50, 54, 55, 70, 76, and 129.)

[10] A. Di Piazza, C. Müller, K. Z. Hatsagortsyan, and C. H. Keitel. Extremely high-intensity laser interactions with fundamental

quantum systems. *Rev. Mod. Phys.*, 84:1177–1228, Aug 2012. doi: 10.1103/RevModPhys.84.1177. URL http://link.aps.org/doi/10.1103/RevModPhys.84.1177. (Cited on pages 1, 25, 51, and 131.)

[11] C. P. Ridgers, C. S. Brady, R. Duclous, J. G. Kirk, K. Bennett, T. D. Arber, A. P. L. Robinson, and A. R. Bell. Dense electron-positron plasmas and ultraintense γ rays from laser-irradiated solids. *Phys. Rev. Lett.*, 108:165006, Apr 2012. doi: 10.1103/PhysRevLett.108.165006. URL http://link.aps.org/doi/10.1103/PhysRevLett.108.165006. (Cited on pages 1, 3, 56, 87, and 130.)

[12] D. Strickland and G. Mourou. Compression of amplified chirped optical pulses. *Opt. Comm.*, 56(3):219–221, 1985. doi: 10.1016/0030-4018(85)90120-8. URL http://www.sciencedirect.com/science/article/pii/0030401885901208. (Cited on page 2.)

[13] M. Tamburini, F. Pegoraro, A. Di Piazza, C. H. Keitel, and A. Macchi. Radiation reaction effects on radiation pressure acceleration. *New J. Phys.*, 12(12):123005, 2010. URL http://stacks.iop.org/1367-2630/12/i=12/a=123005. (Cited on pages 2, 14, and 19.)

[14] A. G. R. Thomas, C. P. Ridgers, S. S. Bulanov, B. J. Griffin, and S. P. D. Mangles. Strong radiation-damping effects in a gamma-ray source generated by the interaction of a high-intensity laser with a wakefield-accelerated electron beam. *Phys. Rev. X*, 2:041004, Oct 2012. doi: 10.1103/PhysRevX.2.041004. URL http://link.aps.org/doi/10.1103/PhysRevX.2.041004. (Cited on pages 2, 64, and 88.)

[15] R. Capdessus, E. d'Humières, and V. T. Tikhonchuk. Influence of ion mass on laser-energy absorption and synchrotron radiation at ultrahigh laser intensities. *Phys. Rev. Lett.*, 110:215003, May 2013. doi: 10.1103/PhysRevLett.110.215003. URL http://link.aps.org/doi/10.1103/PhysRevLett.110.215003. (Cited on page 2.)

[16] A. R. Bell and John G. Kirk. Possibility of prolific pair production with high-power lasers. *Phys. Rev. Lett.*, 101:200403, Nov 2008. doi: 10.1103/PhysRevLett.101.200403. URL http://link.aps.org/doi/10.1103/PhysRevLett.101.200403. (Cited on pages 2, 14, 22, 56, 59, 105, and 128.)

[17] R. Duclous, J. G. Kirk, and A. R. Bell. Monte Carlo calculations of pair production in high-intensity laser–plasma interactions. *Plasma Phys. Control. Fusion*, 53:015009, Jan 2011. doi: 10.1088/0741-3335/53/1/015009. URL http://iopscience.iop.org/0741-3335/53/1/015009. (Cited on pages 2, 5, 44, 55, 65, 84, 85, 97, 106, 124, and 130.)

[18] E. N. Nerush, I. Yu. Kostyukov, A. M. Fedotov, N. B. Narozhny, N. V. Elkina, and H. Ruhl. Laser field absorption in self-generated

electron-positron pair plasma. *Phys. Rev. Lett.*, 106:035001, Jan 2011. doi: 10.1103/PhysRevLett.106.035001. URL http://link.aps.org/doi/10.1103/PhysRevLett.106.035001. (Cited on pages 2, 87, 106, and 130.)

[19] N. Neitz and A. Di Piazza. Stochasticity effects in quantum radiation reaction. *Phys. Rev. Lett.*, 111:054802, Aug 2013. doi: 10.1103/PhysRevLett.111.054802. URL http://link.aps.org/doi/10.1103/PhysRevLett.111.054802. (Cited on pages 2, 90, 91, 107, 121, and 130.)

[20] T. G. Blackburn, C. P. Ridgers, J. G. Kirk, and A. R. Bell. Quantum radiation reaction in laser–electron-beam collisions. *Phys. Rev. Lett.*, 112:015001, Jan 2014. doi: 10.1103/PhysRevLett.112.015001. URL http://link.aps.org/doi/10.1103/PhysRevLett.112.015001. (Cited on pages 2, 5, 52, 76, 91, 95, 96, 102, 103, 105, 108, 110, and 130.)

[21] C. S. Brady, C. P. Ridgers, T. D. Arber, A. R. Bell, and J. G. Kirk. Laser absorption in relativistically underdense plasmas by synchrotron radiation. *Phys. Rev. Lett.*, 109:245006, Dec 2012. doi: 10.1103/PhysRevLett.109.245006. URL http://link.aps.org/doi/10.1103/PhysRevLett.109.245006. (Cited on pages 3, 14, 87, and 130.)

[22] C. P. Ridgers, J. G. Kirk, R. Duclous, T. G. Blackburn, C. S. Brady, K. Bennett, T. D. Arber, and A. R. Bell. Modelling gamma-ray photon emission and pair production in high-intensity laser-matter interactions. *J. Comp. Phys.*, 260:273–285, Mar 2014. doi: 10.1016/j.jcp.2013.12.007. URL http://www.sciencedirect.com/science/article/pii/S0021999113008061. (Cited on pages 3, 83, 84, 85, 86, and 87.)

[23] C. D. Murphy. Private communication, Dec 2014. (Cited on pages 5 and 42.)

[24] O. Heaviside. The waste of energy from a moving electron. *Nature*, 67:6–8, Nov 1902. doi: 10.1038/067006d0. URL http://www.nature.com/nature/journal/v67/n1723/index.html. (Cited on pages 5 and 7.)

[25] J. D. Jackson. *Classical Electrodynamics*. John Wiley & Sons, Inc., 3rd edition, 1991. (Cited on pages 5, 7, 74, and 75.)

[26] M. S. Longair. *High Energy Astrophysics*. Cambridge University Press, 3rd edition, 2011. (Cited on pages 5 and 6.)

[27] J. J Thomson. *Conduction of Electricity through Gases*. Cambridge University Press, 2nd edition, 1906. (Cited on page 5.)

[28] J. Larmor. On the theory of the magnetic influence on spectra; and on the radiation from moving ions. *Philos. Mag.*, 44(271):503–512, 1897. doi: 10.1080/14786449708621095. URL http://dx.doi.org/10.1080/14786449708621095. (Cited on page 7.)

[29] Claudio Teitelboim. Radiation reaction as a retarded self-interaction. *Phys. Rev. D*, 4:345–347, Jul 1971. doi: 10.1103/PhysRevD.4.345. URL http://link.aps.org/doi/10.1103/PhysRevD.4.345. (Cited on page 15.)

[30] M. Abraham. *Theorie der Elektrizität*, volume 2. Teubner, 1905. (Cited on page 15.)

[31] F. Rohrlich. The dynamics of a charged sphere and the electron. *Am. J. Phys.*, 65(11):1051–1056, 1997. doi: 10.1119/1.18719. URL http://scitation.aip.org/content/aapt/journal/ajp/65/11/10.1119/1.18719. (Cited on pages 15 and 128.)

[32] G. W. Ford and R. F. O'Connell. Radiation reaction in electrodynamics and the elimination of runaway solutions. *Phys. Lett. A*, 157(4–5):217–220, 1991. ISSN 0375-9601. doi: 10.1016/0375-9601(91)90054-C. URL http://www.sciencedirect.com/science/article/pii/037596019190054C. (Cited on page 18.)

[33] Tse Chin Mo and C. H. Papas. New equation of motion for classical charged particles. *Phys. Rev. D*, 4:3566–3571, Dec 1971. doi: 10.1103/PhysRevD.4.3566. URL http://link.aps.org/doi/10.1103/PhysRevD.4.3566. (Cited on page 18.)

[34] W. B. Bonnor. A new equation of motion for a radiating charged particle. *Proc. R. Soc. London Ser. A*, 337(1611):591–598, 1974. ISSN 0080-4630. doi: 10.1098/rspa.1974.0069. URL http://rspa.royalsocietypublishing.org/content/337/1611/591. (Cited on page 18.)

[35] I. V. Sokolov. Renormalization of the Lorentz-Abraham-Dirac equation for radiation reaction force in classical electrodynamics. *J. Exp. Theor. Phys.*, 109(2):207–212, 2009. ISSN 1063-7761. doi: 10.1134/S1063776109080044. URL http://dx.doi.org/10.1134/S1063776109080044. (Cited on page 18.)

[36] L. D. Landau and E. M. Lifshitz. *The Course of Theoretical Physics*, volume 2. Butterworth-Heinemann, 1987. (Cited on page 18.)

[37] A. Di Piazza. Exact solution of the Landau-Lifshitz equation in a plane wave. *Lett. Math. Phys.*, 83(3):305–313, 2008. ISSN 0377-9017. doi: 10.1007/s11005-008-0228-9. URL http://dx.doi.org/10.1007/s11005-008-0228-9. (Cited on page 19.)

[38] A. Ilderton and G. Torgrimsson. Radiation reaction from QED: Lightfront perturbation theory in a plane wave background. *Phys. Rev. D*, 88:025021, Jul 2013. doi: 10.1103/PhysRevD.88.025021. URL http://link.aps.org/doi/10.1103/PhysRevD.88.025021. (Cited on page 19.)

[39] T. Fulton and F. Rohrlich. Classical radiation from a uniformly accelerated charge. *Ann. Phys.*, 9(4):499–517, 1960. ISSN 0003-4916. doi: 10.1016/0003-4916(60)90105-6. URL http://www.sciencedirect.com/science/article/pii/0003491660901056. (Cited on page 19.)

[40] E. Eriksen and G. Øyvind. On the energy and momentum of an accelerated charged particle and the sources of radiation. *Eur. J. Phys.*, 28(3):401, 2007. doi: 10.1088/0143-0807/28/3/002. URL http://stacks.iop.org/0143-0807/28/i=3/a=002. (Cited on page 19.)

[41] G. A. Schott. On the motion of the Lorentz electron. *Philos. Mag.*, 29(169):49–62, 1915. doi: 10.1080/14786440108635280. URL http://dx.doi.org/10.1080/14786440108635280. (Cited on page 19.)

[42] Ø. Grøn. The significance of the Schott energy for energy-momentum conservation of a radiating charge obeying the Lorentz-Abraham-Dirac equation. *Am. J. Phys.*, 79(1):115–122, 2011. doi: 10.1119/1.3488985. URL http://scitation.aip.org/content/aapt/journal/ajp/79/1/10.1119/1.3488985. (Cited on page 19.)

[43] A. K. Singal. The equivalence principle and an electric charge in a gravitational field II. A uniformly accelerated charge does not radiate. *Gen. Relat. Gravit.*, 29(11):1371–1390, 1997. ISSN 0001-7701. doi: 10.1023/A:1018830012340. URL http://dx.doi.org/10.1023/A%3A1018830012340. (Cited on page 19.)

[44] J. A. Heras and R. F. O'Connell. Generalization of the Schott energy in electrodynamic radiation theory. *Am. J. Phys.*, 74(2):150–153, 2006. doi: 10.1119/1.2142753. URL http://scitation.aip.org/content/aapt/journal/ajp/74/2/10.1119/1.2142753. (Cited on page 19.)

[45] C. de Almeida and A. Saa. The radiation of a uniformly accelerated charge is beyond the horizon: A simple derivation. *Am. J. Phys.*, 74(2):154–158, 2006. doi: 10.1119/1.2162548. URL http://scitation.aip.org/content/aapt/journal/ajp/74/2/10.1119/1.2162548. (Cited on page 19.)

[46] A. Higuchi and G. D. R. Martin. Lorentz-Dirac force from QED for linear acceleration. *Phys. Rev. D*, 70:081701, Oct 2004. doi: 10.1103/PhysRevD.70.081701. URL http://link.aps.org/doi/10.1103/PhysRevD.70.081701. (Cited on page 19.)

[47] W. G. Unruh. Notes on black-hole evaporation. *Phys. Rev. D*, 14:870–892, Aug 1976. doi: 10.1103/PhysRevD.14.870. URL http://link.aps.org/doi/10.1103/PhysRevD.14.870. (Cited on page 20.)

[48] N. B. Narozhny, A. M. Fedotov, B. M. Karnakov, V. D. Mur, and V. A. Belinskii. Boundary conditions in the Unruh problem. *Phys. Rev. D*, 65:025004, Dec 2001. doi: 10.1103/PhysRevD.65.025004. URL http://link.aps.org/doi/10.1103/PhysRevD.65.025004. (Cited on page 20.)

[49] S. A. Fulling and W. G. Unruh. Comment on 'Boundary conditions in the Unruh problem'. *Phys. Rev. D*, 70:048701, Aug 2004. doi: 10.1103/PhysRevD.70.048701. URL http://link.aps.org/doi/10.1103/PhysRevD.70.048701. (Cited on page 20.)

[50] N. B. Narozhny, A. M. Fedotov, B. M. Karnakov, V. D. Mur, and V. A. Belinskii. Reply to 'Comment on 'Boundary conditions in the Unruh problem''. *Phys. Rev. D*, 70:048702, Aug 2004. doi: 10.1103/PhysRevD.70.048702. URL http://link.aps.org/doi/10.1103/PhysRevD.70.048702. (Cited on page 20.)

[51] G. W. Ford and R. F. O'Connell. Is there Unruh radiation? *Phys. Lett. A*, 350(1–2):17–26, 2006. doi: 10.1016/j.physleta.2005.09.068. URL http://www.sciencedirect.com/science/article/pii/S0375960105015355. (Cited on page 20.)

[52] J. Schwinger. On gauge invariance and vacuum polarization. *Phys. Rev.*, 82:664–679, Jun 1951. doi: 10.1103/PhysRev.82.664. URL http://link.aps.org/doi/10.1103/PhysRev.82.664. (Cited on pages 21, 22, 55, and 71.)

[53] F. Sauter. Über das Verhalten eines Elektrons im homogenen elektrischen Feld nach der relativistischen Theorie Diracs. *Z. Phys.*, 69:742, 1931. (Cited on pages 21 and 22.)

[54] V. Yanovsky, V. Chvykov, G. Kalinchenko, P. Rousseau, T. Planchon, T. Matsuoka, A. Maksimchuk, J. Nees, G. Cheriaux, G. Mourou, and K. Krushelnick. Ultra-high intensity- 300-TW laser at 0.1 Hz repetition rate. *Opt. Express*, 16(3):2109–2114, Feb 2008. doi: 10.1364/OE.16.002109. URL http://www.opticsexpress.org/abstract.cfm?URI=oe-16-3-2109. (Cited on pages 21, 55, and 93.)

[55] P. Goldreich and W. H. Julian. Pulsar electrodynamics. *Astrophys. J.*, 157:869, Aug 1969. doi: 10.1086/150119. URL http://adsabs.harvard.edu/doi/10.1086/150119. (Cited on pages 21 and 130.)

[56] A. N. Timokhin. Time-dependent pair cascades in magnetospheres of neutron stars - I. Dynamics of the polar cap cascade with no particle supply from the neutron star surface. *Mon. Not. R. Astron. Soc.*, 408(4):2092–2114, 2010. doi: 10.1111/j.1365-2966.2010.17286.x. URL http://mnras.oxfordjournals.org/content/408/4/2092.abstract. (Cited on page 21.)

[57] D. C. Backer, S. R. Kulkarni, C. Heiles, M. M. Davis, and W. M. Goss. A millisecond pulsar. *Nature*, 300:615–618, Dec 1982. doi: 10.

1038/300615a0. URL http://www.nature.com/nature/journal/v300/n5893/abs/300615a0.html. (Cited on page 21.)

[58] R. C. Duncan and C. Thompson. Formation of very strongly magnetized neutron stars: implications for gamma-ray bursts. *Ap. J.*, 392:L9–L13, Jun 1992. doi: 10.1086/186413. URL http://adsabs.harvard.edu/abs/1992ApJ...392L...9D. (Cited on page 21.)

[59] K. Makishima, T. Enoto, J. S. Hiraga, T. Nakano, K. Nakazawa, S. Sakurai, M. Sasano, and H. Murakami. Possible evidence for free precession of a strongly magnetized neutron star in the magnetar 4U 0142 + 61. *Phys. Rev. Lett.*, 112:171102, Apr 2014. doi: 10.1103/PhysRevLett.112.171102. URL http://link.aps.org/doi/10.1103/PhysRevLett.112.171102. (Cited on page 21.)

[60] T. Erber. High-energy electromagnetic conversion processes in intense magnetic fields. *Rev. Mod. Phys.*, 38:626–659, Oct 1966. doi: 10.1103/RevModPhys.38.626. URL http://link.aps.org/doi/10.1103/RevModPhys.38.626. (Cited on pages 21, 55, 57, 62, 64, 65, 67, and 75.)

[61] J. K. Daugherty and I. Lerche. Theory of pair production in strong electric and magnetic fields and its applicability to pulsars. *Phys. Rev. D*, 14:340–355, Jul 1976. doi: 10.1103/PhysRevD.14.340. URL http://link.aps.org/doi/10.1103/PhysRevD.14.340. (Cited on page 21.)

[62] J. K. Daugherty and A. K. Harding. Pair production in superstrong magnetic fields. *Astrophys. J.*, 273:761–773, October 1983. doi: 10.1086/161411. URL http://adsabs.harvard.edu/abs/1983ApJ...273..761D. (Cited on page 21.)

[63] M. E. Peskin and D. V. Schroeder. *An Introduction to Quantum Field Theory*. Westview Press, 1995. (Cited on pages 22, 26, 27, 74, 75, and 129.)

[64] W. Heisenberg and H. Euler. Folgerungen aus der Diracschen Theorie des Positrons. *Z. Phys.*, 98:714, 1936. (Cited on page 22.)

[65] O. Klein and T. Nishina. Über die Streuung von Strahlung durch freie Elektronen nach der neuen relativistischen Quantendynamik von Dirac. *Zeitschrift fur Physik*, 52:853–868, November 1929. doi: 10.1007/BF01366453. (Cited on pages 25 and 35.)

[66] A. H. Compton. A quantum theory of the scattering of X-rays by light elements. *Phys. Rev.*, 21:483–502, May 1923. doi: 10.1103/PhysRev.21.483. URL http://link.aps.org/doi/10.1103/PhysRev.21.483. (Cited on page 25.)

[67] F. Mackenroth and A. Di Piazza. Nonlinear Compton scattering in ultrashort laser pulses. *Phys. Rev. A*, 83:032106, Mar 2011. doi: 10.1103/PhysRevA.83.032106. URL http://link.aps.org/doi/10.1103/PhysRevA.83.032106. (Cited on pages 26, 46, and 129.)

[68] T. Heinzl. Strong-field QED and high-power lasers. *Int. J. Mod. Phys. A*, 27(15):1260010, 2012. doi: 10.1142/S0217751X1260010X. URL http://www.worldscientific.com/doi/abs/10.1142/S0217751X1260010X. (Cited on pages 26 and 129.)

[69] D. M. Volkov. *Z. Phys.*, 94:250, 1935. (Cited on pages 26 and 28.)

[70] C. N. Harvey, T. Heinzl, A. Ilderton, and M. Marklund. Intensity-dependent electron mass shift in a laser field: Existence, universality, and detection. *Phys. Rev. Lett.*, 109:100402, Sep 2012. doi: 10.1103/PhysRevLett.109.100402. URL http://link.aps.org/doi/10.1103/PhysRevLett.109.100402. (Cited on page 29.)

[71] C. N. Harvey, T. Heinzl, and A. Ilderton. Signatures of high-intensity Compton scattering. *Phys. Rev. A*, 79:063407, Jun 2009. doi: 10.1103/PhysRevA.79.063407. URL http://link.aps.org/doi/10.1103/PhysRevA.79.063407. (Cited on pages 29, 33, and 129.)

[72] DLMF. NIST Digital Library of Mathematical Functions. http://dlmf.nist.gov/, Release 1.0.9 of 2014-08-29. URL http://dlmf.nist.gov/10.19.E1/. (Cited on page 35.)

[73] D. Seipt. *Strong-Field QED Processes in Short Laser Pulses: One- and Two-Photon Compton Scattering*. PhD thesis, Institut für Theoretische Physik, Fachrichtung Physik, Fakultät Mathematik und Naturwissenschaften der Technischen Universität Dresden, 2012. (Cited on page 39.)

[74] C. Bula, K. T. McDonald, E. J. Prebys, C. Bamber, S. Boege, T. Kotseroglou, A. C. Melissinos, D. D. Meyerhofer, W. Ragg, D. L. Burke, R. C. Field, G. Horton-Smith, A. C. Odian, J. E. Spencer, D. Walz, S. C. Berridge, W. M. Bugg, K. Shmakov, and A. W. Weidemann. Observation of nonlinear effects in Compton scattering. *Phys. Rev. Lett.*, 76:3116–3119, Apr 1996. doi: 10.1103/PhysRevLett.76.3116. URL http://link.aps.org/doi/10.1103/PhysRevLett.76.3116. (Cited on page 40.)

[75] D. L. Burke, R. C. Field, G. Horton-Smith, J. E. Spencer, D. Walz, S. C. Berridge, W. M. Bugg, K. Shmakov, A. W. Weidemann, C. Bula, K. T. McDonald, E. J. Prebys, C. Bamber, S. J. Boege, T. Koffas, T. Kotseroglou, A. C. Melissinos, D. D. Meyerhofer, D. A. Reis, and W. Ragg. Positron production in multiphoton light-by-light scattering. *Phys. Rev. Lett.*, 79:1626–1629, Sep 1997. doi: 10.1103/PhysRevLett.79.1626. URL http://link.aps.org/doi/10.1103/PhysRevLett.79.1626. (Cited on pages 40, 76, 95, 98, 107, and 130.)

[76] C. Bamber, S. J. Boege, T. Koffas, T. Kotseroglou, A. C. Melissinos, D. D. Meyerhofer, D. A. Reis, W. Ragg, C. Bula, K. T. McDonald, E. J. Prebys, D. L. Burke, R. C. Field, G. Horton-Smith,

J. E. Spencer, D. Walz, S. C. Berridge, W. M. Bugg, K. Shmakov, and A. W. Weidemann. Studies of nonlinear QED in collisions of 46.6 GeV electrons with intense laser pulses. *Phys. Rev. D*, 60: 092004, Oct 1999. doi: 10.1103/PhysRevD.60.092004. URL http://link.aps.org/doi/10.1103/PhysRevD.60.092004. (Cited on page 40.)

[77] K. Ta Phuoc, S. Corde, Thaury C., Malka V., Tafzi A., J. P. Goddet, R. C. Shah, S. Sebban, and A. Rousse. All-optical Compton gamma ray source. *Nature Photonics*, 6:308–311, Apr 2012. doi: 10.1038/nphoton.2012.82. URL http://dx.doi.org/10.1038/nphoton.2012.82. (Cited on pages 40 and 41.)

[78] S. Kneip, S. R. Nagel, S. F. Martins, S. P. D. Mangles, C. Bellei, O. Chekhlov, R. J. Clarke, N. Delerue, E. J. Divall, G. Doucas, K. Ertel, F. Fiuza, R. Fonseca, P. Foster, S. J. Hawkes, C. J. Hooker, K. Krushelnick, W. B. Mori, C. A. J. Palmer, K. Ta Phuoc, P. P. Rajeev, J. Schreiber, M. J. V. Streeter, D. Urner, J. Vieira, L. O. Silva, and Z. Najmudin. Near-GeV acceleration of electrons by a nonlinear plasma wave driven by a self-guided laser pulse. *Phys. Rev. Lett.*, 103:035002, Jul 2009. doi: 10.1103/PhysRevLett.103.035002. URL http://link.aps.org/doi/10.1103/PhysRevLett.103.035002. (Cited on pages 42, 44, and 95.)

[79] S. Agontinelli et al. Geant4–a simulation toolkit. *Nucl. Instr. Meth. Phys. Res. A*, 506(3):250–303, 2003. ISSN 0168-9002. doi: 10.1016/S0168-9002(03)01368-8. URL http://www.sciencedirect.com/science/article/pii/S0168900203013688. (Cited on page 43.)

[80] J. Allison et al. Geant4 developments and applications. *IEEE Trans. Nucl. Sci.*, 53(1):270–278, Feb 2006. ISSN 0018-9499. doi: 10.1109/TNS.2006.869826. URL http://ieeexplore.ieee.org/xpls/abs_all.jsp?isnumber=33833&arnumber=1610988&count=33&index=7. (Cited on page 43.)

[81] T. Heinzl, D. Seipt, and B. Kämpfer. Beam-shape effects in nonlinear Compton and Thomson scattering. *Phys. Rev. A*, 81: 022125, Feb 2010. doi: 10.1103/PhysRevA.81.022125. URL http://link.aps.org/doi/10.1103/PhysRevA.81.022125. (Cited on page 45.)

[82] D. Seipt and B. Kämpfer. Nonlinear Compton scattering of ultrashort intense laser pulses. *Phys. Rev. A*, 83:022101, Feb 2011. doi: 10.1103/PhysRevA.83.022101. URL http://link.aps.org/doi/10.1103/PhysRevA.83.022101. (Cited on page 46.)

[83] G. Sarri, D. J. Corvan, W. Schumaker, J. M. Cole, A. Di Piazza, H. Ahmed, C. Harvey, C. H. Keitel, K. Krushelnick, S. P. D. Mangles, Z. Najmudin, D. Symes, A. G. R. Thomas, M. Yeung, Z. Zhao, and M. Zepf. Ultrahigh brilliance multi-MeV γ-ray beams from nonlinear relativistic thomson scattering. *Phys. Rev. Lett.*, 113:224801,

Nov 2014. doi: 10.1103/PhysRevLett.113.224801. URL http://link.aps.org/doi/10.1103/PhysRevLett.113.224801. (Cited on pages 48 and 129.)

[84] J. G. Kirk, A. R. Bell, and I. Arka. Pair production in counter-propagating laser beams. *Plasma Phys. Control. Fusion*, 51: 085008, Aug 2009. doi: 10.1088/0741-3335/51/8/085008. URL http://iopscience.iop.org/0741-3335/51/8/085008/. (Cited on pages 50, 54, 55, 59, 62, 65, 76, and 129.)

[85] C. N. Harvey, A. Ilderton, and B. King. Testing numerical implementations of strong-field electrodynamics. *Phys. Rev. A*, 91: 013822, Jan 2015. doi: 10.1103/PhysRevA.91.013822. URL http://link.aps.org/doi/10.1103/PhysRevA.91.013822. (Cited on pages 50, 61, and 131.)

[86] A. Di Piazza, K. Z. Hatsagortsyan, and C. H. Keitel. Quantum radiation reaction effects in multiphoton Compton scattering. *Phys. Rev. Lett.*, 105:220403, Nov 2010. doi: 10.1103/PhysRevLett.105.220403. URL http://link.aps.org/doi/10.1103/PhysRevLett.105.220403. (Cited on page 51.)

[87] A. I. Nishikov and V. I. Ritus. Quantum processes in the field of a plane electromagnetic wave and in a constant field. *Sov. Phys. JETP*, 19:1191–1199, Nov 1964. URL http://www.jetp.ac.ru/cgi-bin/e/index/e/19/5/p1191?a=list. (Cited on page 55.)

[88] B. King and H. Ruhl. Trident pair production in a constant crossed field. *Phys. Rev. D*, 88:013005, Jul 2013. doi: 10.1103/PhysRevD.88.013005. URL http://link.aps.org/doi/10.1103/PhysRevD.88.013005. (Cited on pages 55, 71, 73, 74, 75, 76, and 131.)

[89] N. P. Klepikov. *Zh. Eksp. Teor. Fiz.*, 26, 1954. (Cited on page 55.)

[90] J. Schwinger. The quantum correction in the radiation by energetic electrons. *Proc. Natl. Acad. Sci.*, 40(2):132–136, 1954. URL http://www.pnas.org/content/40/2/132.short. (Cited on pages 55, 59, and 62.)

[91] V. N. Baier, V. M. Katkov, and V. M. Strakhovenko. *Electromagnetic Processes at High Energies in Oriented Single Crystals*. World Scientific, 1998. (Cited on pages 55, 56, 57, 62, 65, 66, 67, and 78.)

[92] A. H. Sørensen. Channeling, bremsstrahlung and pair creation in single crystals. *Nucl. Instrum. Methods Phys. Res. B*, 119:2–29, Oct 1996. doi: 10.1016/0168-583X(96)00349-7. URL http://www.sciencedirect.com/science/article/pii/0168583X96003497. (Cited on page 59.)

[93] Ulrik I. Uggerhøj. The interaction of relativistic particles with strong crystalline fields. *Rev. Mod. Phys.*, 77:1131–1171, Oct 2005. doi: 10.1103/RevModPhys.77.1131. URL http://link.aps.org/

doi/10.1103/RevModPhys.77.1131. (Cited on pages 59, 65, 67, 72, and 77.)

[94] J. Lindhard. Quantum-radiation spectra of relativistic particles derived by the correspondence principle. *Phys. Rev. A*, 43:6032–6037, Jun 1991. doi: 10.1103/PhysRevA.43.6032. URL http://link.aps.org/doi/10.1103/PhysRevA.43.6032. (Cited on page 59.)

[95] K. Kirsebom, U. Mikkelsen, E. Uggerhøj, K. Elsener, S. Ballestrero, P. Sona, and Z. Z. Vilakazi. First measurements of the unique influence of spin on the energy loss of ultrarelativistic electrons in strong electromagnetic fields. *Phys. Rev. Lett.*, 87:054801, Jul 2001. doi: 10.1103/PhysRevLett.87.054801. URL http://link.aps.org/doi/10.1103/PhysRevLett.87.054801. (Cited on pages 59 and 77.)

[96] A. A. Sokolov, N. P. Klepikov, and I. M. Ternov. *Doklady Akad. Nauk SSSR*, 89, 1953. (Cited on page 62.)

[97] A. A. Sokolov and I. M. Ternov. *Synchrotron Radiation*. Pergamon, 1968. (Cited on page 62.)

[98] S. R. Yoffe, Y. Kravets, A. Noble, and D. A. Jaroszynski. Semiclassical beam cooling in an intense laser pulse. *ArXiv e-prints*, October 2014. URL http://arxiv.org/abs/1410.1759. (Cited on page 64.)

[99] C. S. Shen and D. White. Energy straggling and radiation reaction for magnetic bremsstrahlung. *Phys. Rev. Lett.*, 28:455–459, Feb 1972. doi: 10.1103/PhysRevLett.28.455. URL http://link.aps.org/doi/10.1103/PhysRevLett.28.455. (Cited on pages 64 and 97.)

[100] G. Breit and J. A. Wheeler. Collision of two light quanta. *Phys. Rev.*, 46:1087–1091, Dec 1934. doi: 10.1103/PhysRev.46.1087. URL http://link.aps.org/doi/10.1103/PhysRev.46.1087. (Cited on page 65.)

[101] O. J. Pike, F. Mackenroth, E. G. Hill, and S. J. Rose. A photon-photon collider in a vacuum hohlraum. *Nature Photonics*, 8:434–436, Jun 2014. doi: 10.1038/nphoton.2014.95. URL http://dx.doi.org/10.1038/nphoton.2014.95. (Cited on page 65.)

[102] N. V. Elkina, A. M. Fedotov, I. Yu. Kostyukov, M. V. Legkov, N. B. Narozhny, E. N. Nerush, and H. Ruhl. QED cascades induced by circularly polarized laser fields. *Phys. Rev. ST Accel. Beams*, 14:054401, May 2011. doi: 10.1103/PhysRevSTAB.14.054401. URL http://link.aps.org/doi/10.1103/PhysRevSTAB.14.054401. (Cited on pages 65, 67, 87, and 89.)

[103] G. Bassompierre, G. Bologna, D. Boget, M. Chevallier, S. Costa, J. Dufournaud, M. Farizon, B. Farizon Mazuy, A. Feliciello,

M.J. Gaillard, R. Garfagnini, R. Genre, M. Gouanère, B. Ille, R. Kirsch, P. Lautesse, M. Richard, E. Rossetto, D. Sillou, and M. Spighel. Search for light neutral objects photoproduced in a crystal strong field and decaying into e^+e^- pairs. *Phys. Lett. B*, 355(3–4):584–594, Aug 1995. doi: http://dx.doi.org/10.1016/0370-2693(95)00628-X. URL http://www.sciencedirect.com/science/article/pii/037026939500628X. (Cited on page 68.)

[104] A. I. Voroshilo, E. A. Padusenko, and S. P. Roshchupkin. One-photon annihilation of an electron-positron pair in the field of pulsed circularly polarized light wave. *Laser Phys.*, 20(7):1679–1685, 2010. ISSN 1054-660X. doi: 10.1134/S1054660X10130177. URL http://dx.doi.org/10.1134/S1054660X10130177. (Cited on page 69.)

[105] V. Bargmann, Louis Michel, and V. L. Telegdi. Precession of the polarization of particles moving in a homogeneous electromagnetic field. *Phys. Rev. Lett.*, 2:435–436, May 1959. doi: 10.1103/PhysRevLett.2.435. URL http://link.aps.org/doi/10.1103/PhysRevLett.2.435. (Cited on page 70.)

[106] B. King, N. Elkina, and H. Ruhl. Photon polarization in electron-seeded pair-creation cascades. *Phys. Rev. A*, 87:042117, Apr 2013. doi: 10.1103/PhysRevA.87.042117. URL http://link.aps.org/doi/10.1103/PhysRevA.87.042117. (Cited on page 70.)

[107] C. Bula and K. T. McDonald. The Weizsäcker-Williams approximation to trident production in electron photon collisions. *ArXiv e-prints*, Apr 1997. URL http://arxiv.org/abs/hep-ph/0004117. (Cited on pages 71 and 76.)

[108] Anton Ilderton. Trident pair production in strong laser pulses. *Phys. Rev. Lett.*, 106:020404, Jan 2011. doi: 10.1103/PhysRevLett.106.020404. URL http://link.aps.org/doi/10.1103/PhysRevLett.106.020404. (Cited on pages 71 and 73.)

[109] D. Seipt and B. Kämpfer. Two-photon Compton process in pulsed intense laser fields. *Phys. Rev. D*, 85:101701, May 2012. doi: 10.1103/PhysRevD.85.101701. URL http://link.aps.org/doi/10.1103/PhysRevD.85.101701. (Cited on page 71.)

[110] F. Mackenroth and A. Di Piazza. Nonlinear double Compton scattering in the ultrarelativistic quantum regime. *Phys. Rev. Lett.*, 110:070402, Feb 2013. doi: 10.1103/PhysRevLett.110.070402. URL http://link.aps.org/doi/10.1103/PhysRevLett.110.070402. (Cited on pages 71 and 79.)

[111] M. Schumacher. Delbrück scattering. *Radiat. Phys. Chem.*, 56(1–2):101–111, Aug 1999. ISSN 0969-806X. doi: http://dx.doi.org/10.1016/S0969-806X(99)00289-3. URL http://www.sciencedirect.com/science/article/pii/S0969806X99002893. (Cited on page 71.)

[112] A. Di Piazza and A. I. Milstein. Delbrück scattering in combined Coulomb and laser fields. *Phys. Rev. A*, 77:042102, Apr 2008. doi: 10.1103/PhysRevA.77.042102. URL http://link.aps.org/doi/10.1103/PhysRevA.77.042102. (Cited on pages 71 and 72.)

[113] S. L. Adler, J. N. Bahcall, C. G. Callan, and M. N. Rosenbluth. Photon splitting in a strong magnetic field. *Phys. Rev. Lett.*, 25:1061–1065, Oct 1970. doi: 10.1103/PhysRevLett.25.1061. URL http://link.aps.org/doi/10.1103/PhysRevLett.25.1061. (Cited on page 71.)

[114] Sh. Zh. Akhmadaliev, G. Ya. Kezerashvili, S. G. Klimenko, R. N. Lee, V. M. Malyshev, A. L. Maslennikov, A. M. Milov, A. I. Milstein, N. Yu. Muchnoi, A. I. Naumenkov, V. S. Panin, S. V. Peleganchuk, G. E. Pospelov, I. Ya. Protopopov, L. V. Romanov, A. G. Shamov, D. N. Shatilov, E. A. Simonov, V. M. Strakhovenko, and Yu. A. Tikhonov. Experimental investigation of high-energy photon splitting in atomic fields. *Phys. Rev. Lett.*, 89:061802, Jul 2002. doi: 10.1103/PhysRevLett.89.061802. URL http://link.aps.org/doi/10.1103/PhysRevLett.89.061802. (Cited on page 71.)

[115] A. Di Piazza, A. I. Milstein, and C. H. Keitel. Photon splitting in a laser field. *Phys. Rev. A*, 76:032103, Sep 2007. doi: 10.1103/PhysRevA.76.032103. URL http://link.aps.org/doi/10.1103/PhysRevA.76.032103. (Cited on page 71.)

[116] B. King. Double Compton scattering in a constant crossed field. *Phys. Rev. A*, 91:033415, Mar 2015. doi: 10.1103/PhysRevA.91.033415. URL http://link.aps.org/doi/10.1103/PhysRevA.91.033415. (Cited on pages 72 and 131.)

[117] E. Brezin and C. Itzykson. Pair production in vacuum by an alternating field. *Phys. Rev. D*, 2:1191–1199, Oct 1970. doi: 10.1103/PhysRevD.2.1191. URL http://link.aps.org/doi/10.1103/PhysRevD.2.1191. (Cited on page 72.)

[118] C. F. Weizsäcker. Ausstrahlung bei Stössen sehr schneller Elektronen. *Zeitschrift für Physik*, 88(9–10):612–625, Feb 1934. ISSN 0044-3328. doi: 10.1007/BF01333110. URL http://dx.doi.org/10.1007/BF01333110. (Cited on page 74.)

[119] E. J. Williams. Nature of the high energy particles of penetrating radiation and status of ionization and radiation formulae. *Phys. Rev.*, 45:729–730, May 1934. doi: 10.1103/PhysRev.45.729. URL http://link.aps.org/doi/10.1103/PhysRev.45.729. (Cited on page 74.)

[120] N. B. Narozhny. Expansion parameter of perturbation theory in intense-field quantum electrodynamics. *Phys. Rev. D*, 21:1176–1183, Feb 1980. doi: 10.1103/PhysRevD.21.1176. URL http://link.aps.org/doi/10.1103/PhysRevD.21.1176. (Cited on page 76.)

[121] J. Lindhard. Influence of crystal lattice on motion of energetic charged particles. *K. Dan. Vidensk. Selsk. Mat. Fys. Medd.*, 34:1–64, 1965. URL http://www.sdu.dk/media/bibpdf/Bind%2030-39/Bind/mfm-34-14.pdf. (Cited on page 77.)

[122] K. K. Andersen, J. Esberg, H. Knudsen, H. D. Thomsen, U. I. Uggerhøj, P. Sona, A. Mangiarotti, T. J. Ketel, A. Dizdar, and S. Ballestrero. Experimental investigations of synchrotron radiation at the onset of the quantum regime. *Phys. Rev. D*, 86: 072001, Oct 2012. doi: 10.1103/PhysRevD.86.072001. URL http://link.aps.org/doi/10.1103/PhysRevD.86.072001. (Cited on pages 77 and 95.)

[123] A. Belkacem, G. Bologna, M. Chevallier, N. Cue, M. J. Gaillard, R. Genre, J. C. Kimball, R. Kirsch, B. Marsh, J. P. Peigneux, J. C. Poizat, J. Remillieux, D. Sillou, M. Spighel, and C. R. Sun. Study of e^+-e^- pair creation by 20–150-GeV photons incident on a germanium crystal in alignment conditions. *Phys. Rev. Lett.*, 58:1196–1199, Mar 1987. doi: 10.1103/PhysRevLett.58.1196. URL http://link.aps.org/doi/10.1103/PhysRevLett.58.1196. (Cited on page 77.)

[124] A. Belkacem, G. Bologna, M. Chevallier, A. Clouvas, N. Cue, M. J. Gaillard, R. Genre, C. C. Kimball, R. Kirsch, B. Marsh, J. P. Peigneux, J. C. Poizat, J. Remillieux, D. Sillou, M. Spighel, and C. R. Sun. Observation of enhanced pair creation for 50–110-GeV photons in an aligned Ge crystal. *Phys. Rev. Lett.*, 53:2371–2373, Dec 1984. doi: 10.1103/PhysRevLett.53.2371. URL http://link.aps.org/doi/10.1103/PhysRevLett.53.2371. (Cited on page 77.)

[125] V. N. Baier and V. M. Katkov. Quantum effects in magnetic bremsstrahlung. *Phys. Lett. A*, 25(7):492–493, Oct 1967. doi: 10.1016/0375-9601(67)90003-5. URL http://www.sciencedirect.com/science/article/pii/0375960167900035. (Cited on page 78.)

[126] C. K. Birdsall and A. B. Langdon. *Plasma Physics via Computer Simulation*. Taylor & Francis Group, 2005. (Cited on pages 81 and 85.)

[127] J. M. Dawson. Particle simulation of plasmas. *Rev. Mod. Phys.*, 55:403–447, Apr 1983. doi: 10.1103/RevModPhys.55.403. URL http://link.aps.org/doi/10.1103/RevModPhys.55.403. (Cited on page 81.)

[128] J. P. Boris. Relativistic plasma simulation - optimization of a hybrid code. In *Proc. Fourth Conf. Num. Sim. Plasmas*, pages 3–67. Naval Res. Lab., 1970. (Cited on page 82.)

[129] J.-L. Vay. Simulation of beams or plasmas crossing at relativistic velocity. *Phys. Plasmas*, 15(5):056701, 2008. doi: http://dx.doi.org/

10.1063/1.2837054. URL http://scitation.aip.org/content/aip/journal/pop/15/5/10.1063/1.2837054. (Cited on page 82.)

[130] J. Villasenor and O. Buneman. Rigorous charge conservation for local electromagnetic field solvers. *Comput. Phys. Commun.*, 69(2–3):306–316, 1992. doi: http://dx.doi.org/10.1016/0010-4655(92)90169-Y. URL http://www.sciencedirect.com/science/article/pii/001046559290169Y. (Cited on page 82.)

[131] K. S. Yee. Numerical solution of initial boundary value problems involving Maxwell's equations in isotropic media. *IEEE Trans. Antennas Propag.*, 14(3):302–307, May 1966. doi: 10.1109/TAP.1966.1138693. URL http://ieeexplore.ieee.org/xpl/articleDetails.jsp?arnumber=1138693. (Cited on page 82.)

[132] J.-P. Berenger. A perfectly matched layer for the absorption of electromagnetic waves. *J. Comp. Phys.*, 114(2):185–200, Oct 1994. doi: http://dx.doi.org/10.1006/jcph.1994.1159. URL http://www.sciencedirect.com/science/article/pii/S0021999184711594. (Cited on page 83.)

[133] K. Nanbu. Theory of cumulative small-angle collisions in plasmas. *Phys. Rev. E*, 55:4642–4652, Apr 1997. doi: 10.1103/PhysRevE.55.4642. URL http://link.aps.org/doi/10.1103/PhysRevE.55.4642. (Cited on page 83.)

[134] R. Courant, K. Friedrichs, and H. Lewy. On the partial difference equations of mathematical physics. *IBM J. Res. Dev.*, 11:215–234, 1967. ISSN 0018-8646/e. doi: 10.1147/rd.112.0215. (Cited on page 83.)

[135] Extendable PIC Open Collaboration. URL http://ccpforge.cse.rl.ac.uk/gf/project/epoch/. (Cited on page 84.)

[136] Osiris. URL https://plasmasim.physics.ucla.edu/codes/osiris. (Cited on page 84.)

[137] M. Vranic, T. Grismayer, J. L. Martins, R. A. Fonseca, and L. O. Silva. Particle merging algorithm for PIC codes. *ArXiv e-prints*, November 2014. URL http://arxiv.org/abs/1411.2248. (Cited on page 87.)

[138] E. N. Nerush and I. Y. Kostyukov. Laser-driven hole boring and gamma-ray emission in high-density plasmas. *Plasma Phys. Control. Fusion*, 57(3):035007, Feb 2015. doi: 10.1088/0741-3335/57/3/035007. URL http://iopscience.iop.org/0741-3335/57/3/035007/. (Cited on page 87.)

[139] V. F. Bashmakov, E. N. Nerush, I. Yu. Kostyukov, A. M. Fedotov, and N. B. Narozhny. Effect of laser polarization on quantum electrodynamical cascading. *Phys. Plasmas*, 21(1):013105, Jan 2014. doi: http://dx.doi.org/10.1063/

1.4861863. URL http://scitation.aip.org/content/aip/journal/pop/21/1/10.1063/1.4861863. (Cited on page 87.)

[140] Suo Tang, Muhammad Ali Bake, Hong-Yu Wang, and Bai-Song Xie. QED cascade induced by a high-energy γ photon in a strong laser field. *Phys. Rev. A*, 89:022105, Feb 2014. doi: 10.1103/PhysRevA.89.022105. URL http://link.aps.org/doi/10.1103/PhysRevA.89.022105. (Cited on page 87.)

[141] M. Tamburini, T. V. Liseykina, F. Pegoraro, and A. Macchi. Radiation-pressure-dominant acceleration: Polarization and radiation reaction effects and energy increase in three-dimensional simulations. *Phys. Rev. E*, 85:016407, Jan 2012. doi: 10.1103/PhysRevE.85.016407. URL http://link.aps.org/doi/10.1103/PhysRevE.85.016407. (Cited on page 88.)

[142] M. Vranic, J. L. Martins, J. Vieira, R. A. Fonseca, and L. O. Silva. All-optical radiation reaction at 10^{21} W/cm^2. *Phys. Rev. Lett.*, 113:134801, Sep 2014. doi: 10.1103/PhysRevLett.113.134801. URL http://link.aps.org/doi/10.1103/PhysRevLett.113.134801. (Cited on page 88.)

[143] Igor V. Sokolov, Natalia M. Naumova, John A. Nees, and Gérard A. Mourou. Pair creation in QED-strong pulsed laser fields interacting with electron beams. *Phys. Rev. Lett.*, 105:195005, Nov 2010. doi: 10.1103/PhysRevLett.105.195005. URL http://link.aps.org/doi/10.1103/PhysRevLett.105.195005. (Cited on pages 89, 90, and 130.)

[144] S. S. Bulanov, C. B. Schroeder, E. Esarey, and W. P. Leemans. Electromagnetic cascade in high-energy electron, positron, and photon interactions with intense laser pulses. *Phys. Rev. A*, 87:062110, Jun 2013. doi: 10.1103/PhysRevA.87.062110. URL http://link.aps.org/doi/10.1103/PhysRevA.87.062110. (Cited on page 90.)

[145] N. Neitz. Private communication, Nov 2012. (Cited on page 91.)

[146] W. L. Kruer. *The Physics of Laser-Plasma Interactions*. Westview Press, 2003. (Cited on page 91.)

[147] J. G. Kirk, A. R. Bell, and C. P. Ridgers. Pair plasma cushions in the hole-boring scenario. *Plasma Phys. Control. Fusion*, 55 (9):096016, Aug 2013. doi: 10.1088/0741-3335/55/9/095016. URL http://iopscience.iop.org/0741-3335/55/9/095016. (Cited on page 92.)

[148] Hyung Taek Kim, Ki Hong Pae, Hyuk Jin Cha, I Jong Kim, Tae Jun Yu, Jae Hee Sung, Seong Ku Lee, Tae Moon Jeong, and Jongmin Lee. Enhancement of electron energy to the multi-GeV regime by a dual-stage laser-wakefield accelerator pumped by petawatt laser pulses. *Phys. Rev. Lett.*, 111:165002, Oct 2013. doi:

10.1103/PhysRevLett.111.165002. URL http://link.aps.org/doi/10.1103/PhysRevLett.111.165002. (Cited on page 95.)

COLOPHON

This document was typeset using the typographical look-and-feel `classicthesis` developed by André Miede. The style was inspired by Robert Bringhurst's seminal book on typography "*The Elements of Typographic Style*". `classicthesis` is available for both LaTeX and LyX:

http://code.google.com/p/classicthesis/

Happy users of `classicthesis` usually send a real postcard to the author, a collection of postcards received so far is featured here:

http://postcards.miede.de/

Final Version as of July 29, 2015 (`classicthesis`).